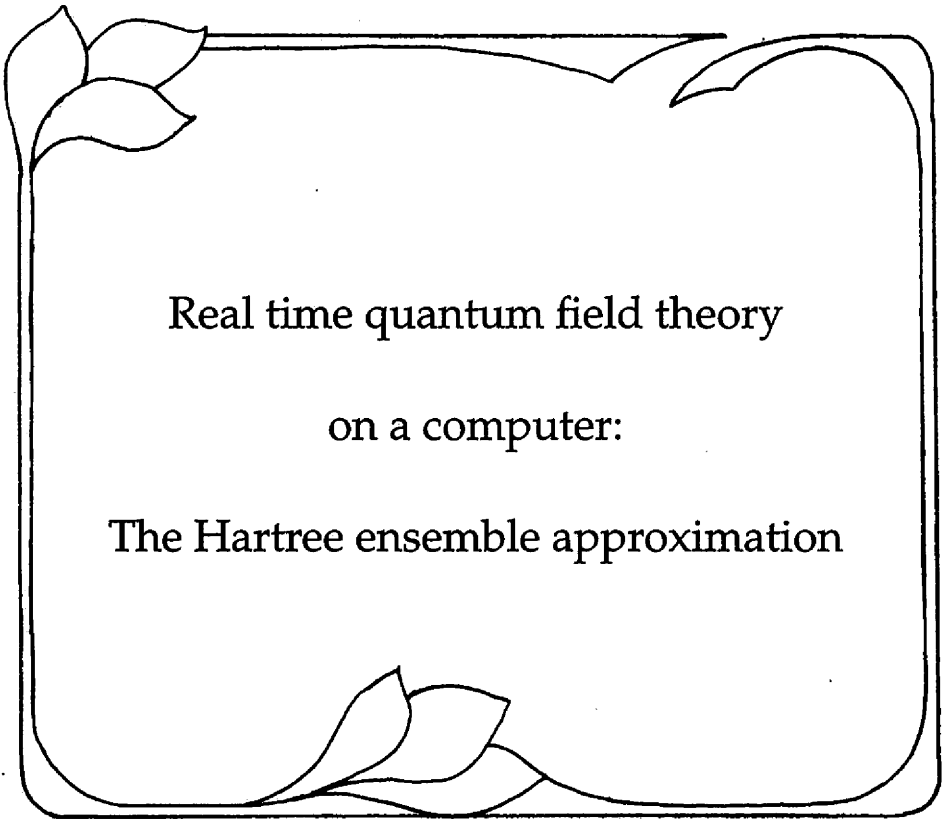

Real time quantum field theory on a computer: The Hartree ensemble approximation

Mischa Sallé

Real time quantum field theory on a computer: The Hartree ensemble approximation

Real time quantum field theory on a computer: The Hartree ensemble approximation

Academisch Proefschrift

ter verkrijging van de graad van doctor
aan de Universiteit van Amsterdam
op gezag van de Rector Magnificus
prof.mr. P.F. van der Heijden
ten overstaan van een door het college voor promoties ingestelde
commissie, in het openbaar te verdedigen in de Aula der Universiteit
op dinsdag 3 december 2002, te 10.00 uur

door

Mischa Sallé

geboren te Amsterdam

Promotiecommissie:

Promotor:	Prof. dr. J. Smit
Overige leden:	Prof. dr. P.J. van Baal Prof. dr. ir F.A. Bais Prof. dr. J.H. Koch Prof. dr. H.T.C. Stoof Dr. J.C. Vink Prof. dr. Ch. van Weert

Faculteit der Natuurwetenschappen, Wiskunde en Informatica

Cover design by Marijke Sallé

This work is part of the research program of the "Stichting voor Fundamenteel Onderzoek de Materie" (FOM), which is financially supported by the "Nederlandse Organisatie voor Wetenschappelijk Onderzoek" (NWO).

ISBN 90-9016388-3

CONTENTS

List of Figures

CHAPTER 1

INTRODUCTION

1.1 MOTIVATION

Many different areas of physics can be described using the same equations and the same methods from theoretical physics. In condensed matter systems, such as superconductors, superfluids and Bose-Einstein condensates, at temperatures down to 100nK and high energy systems, such as the formation of the quark gluon plasma and the electroweak phase transition at a temperature of 10^{15}K, very similar phenomena play a role, which are described in terms of universal concepts, such as the Higgs mechanism.

We are particularly interested in the description of non-equilibrium and non-perturbative effects that play a role, such as phase transitions. This severely restricts the applicability of many of the standard physical tools such as perturbation theory, or imaginary time Monte Carlo simulations. In order to describe the aforementioned phenomena, one has to resort to approximations, which are still able to describe the non-perturbative and non-equilibrium aspects. The study of one of those, the Hartree approximation will be the topic of this thesis.

Besides the aforementioned systems, there are many more in which the methods described and studied here, can be applied. Since our main motivation comes from the early universe, we will give a very brief overview of some of the main events in its history. A standard reference is still [1], although the latest results are not described.

1.1.1 HUBBLE EXPANSION

The discovery by Edwin Hubble that the further away stars and galaxies are, the faster they move away from us, and its logical implication, that the universe is expanding, has resulted in the Hot Big Bang model, in which the early universe is extremely hot, dense and rapidly expanding. The further one goes back in time, the hotter and denser it becomes. In this process several phase transitions have been

crossed of which the electroweak, already mentioned above, is just one. We will discuss a few of them in a little more detail in the next sections, going backwards in time.

1.1.2 THE COSMIC BACKGROUND RADIATION

One of the last important phase transitions occurred when the universe was about 300 000 thousand years old and had a temperature of 3500K, i.e. $0.3eV$. At that point in history the electrons and nuclei (mostly just protons) combined to neutral atoms. This temperature is considerably lower than the naive estimate of $13.6eV$, the ionisation energy of hydrogen, due to the small number of protons compared to photons, which will be discussed later. Till this point in the thermal history, the nuclei and electrons formed a hot plasma, in which the mean free path for photons is extremely short. Since the universe suddenly became neutral, the photons could travel almost freely and have done so ever since. Because of the expansion, their wavelength has also expanded, about a factor of thousand. Today they are still "visible" as the Cosmic Microwave Background Radiation (CMBR), which has a thermal spectrum with a temperature of 2.73K (due to the interaction with the matter the photons acquired a black body spectrum which, except for the characterizing temperature, is invariant under the expansion). Apart from being direct evidence for the hot and thermal nature of the early universe, it also provides very important information about the universe in the 300 000 years previous to its decoupling: it has such a strong interaction with the matter in the universe, the spacial inhomogeneities of the universe at the time of recombination left their imprint on the CMBR. By measuring in the sky the angular correlations in the CMBR and comparing them with predictions from different cosmological models, such as inflation, one can differentiate between them. See also (the introduction of) Ref. [2] and references therein.

1.1.3 BIG BANG NUCLEOSYNTHESIS

Although the universe was not transparent before the decoupling of photons, there is direct experimental evidence of the Hot Big Bang model dating from as early as the first three minutes, from a period in which the temperature lowered from 1 to $0.1MeV$ (from 10^{10} till 10^9 K). In that (very short) period the protons and neutrons in the universe bound together in nuclei. Up to that point the reaction rates for

$$n \rightleftharpoons p^+ + e^- + \overline{\nu}_e \tag{1.1}$$

were in chemical equilibrium and the ratio of the proton and neutron densities satisfied

$$\frac{N_p}{N_n} \propto e^{-\Delta m/T}, \tag{1.2}$$

where Δm is the mass difference between the proton and neutron. At temperatures higher than this mass difference, the densities are almost equal. Simultaneously, the processes of binding nucleons into nuclei and the opposite, in which the nuclei fall apart again, are also in equilibrium, as in (1.1). However, because of the higher mass difference, free nucleons are highly favoured. At some point the rate of the weak interactions driving (1.1) lacks the Hubble expansion rate and the proton/neutron ratio almost "freezes-out". This happened at a temperature $T \approx 0.8MeV$. Shortly after, around $T \approx 0.3 - 0.1MeV$, the reaction rates for the binding of protons and neutrons into nuclei, favours nuclei instead of free nucleons and almost all of them bind into nuclei of the light elements: nucleosynthesis. The abundances of these light elements, mainly helium, can be calculated and are very accurately reproduced by the experimental data. Only one free parameter is needed, the ratio of the net number of baryons (i.e. baryons minus antibaryons) over photons. This is a remarkable success of the Hot Big Bang model and puts it on a very firm experimental basis all the way back to times of around 1 minute.

The actual value of the free parameter

$$\eta = \frac{n_b - n_{\overline{b}}}{n_\gamma} \tag{1.3}$$

lies somewhere in the range $1.55 \cdot 10^{-10} \ldots 4.45 \cdot 10^{-10}$. The fact that it is so small is the main motivation for baryogenesis, which is discussed in the next section. For a recent review on Big Bang nucleosynthesis (BBN) and its consequences see Ref. [3, 4].

1.1.4 BARYOGENESIS

The fact that η is so small has led to the idea that in the beginning of the universe it may have actually been zero, i.e. all energy resided in photons. However, that would mean that in a later stage an asymmetry between the number of baryons and antibaryons must have been created, baryogenesis. As it turns out, there are three necessary and sufficient conditions, formulated by Sakharov [5], for baryogenesis and all three already are present in the Standard Model (the model describing the elementary particles and their electromagnetic, weak and strong interactions). One of the three conditions states that the baryon number should be non conserving. At low temperatures, the baryon-number is (almost) conserved, the lifetime of a proton is many times longer than the age of the universe. However, at high

temperatures, this is no longer the case. This has to do with the Higgs mechanism, giving all particles their mass. At a temperature of $100GeV$, there is a phase transition at which (coming from low temperatures) the vacuum expectation value (v.e.v.) of the Higgs field goes from a finite value to zero. In the Higgs mechanism all masses are proportional to this v.e.v. and therefore all particles become massless above this electroweak phase transition. Furthermore, due to the vanishing of the Higgs v.e.v., the number of baryons is no longer conserved, any asymmetry existing above this phase transition, will be washed out. It is therefore most logical that the baryogenesis process took place around the electroweak phase transition. In order for a sufficient number of baryons to be created the phase transition has to be strong enough, the v.e.v. has to jump sufficiently fast from zero to a finite value. Unfortunately, it seems this is not the case in the Standard Model. Extensions of Standard Model, in which it is sufficiently strong are under very active investigation. A recent review of the status of electroweak baryogenesis can be found in Ref. [6, 7].

1.1.5 QUARK GLUON PLASMA: HEAVY ION COLLISIONS

As a final example in which phase transitions play an important role, we will briefly discuss the formation of the Quark Gluon Plasma, at the deconfining phase transition (or the confining phase transition, when coming from high temperatures, such as in the early universe). From lattice Monte Carlo simulations, it was predicted that at a temperature of around $150MeV$ ($\approx 10^{15}$K) a phase transition should take place. At low temperatures, the strong force is confining: quarks and gluons attract each other with a force which becomes stronger and stronger at larger distances, i.e. at lower typical energies. At very high temperatures on the other hand, their attraction weakens and the quarks and gluons are asymptotically free. From lattice studies it was found that there should be a phase transition between the two phases around $T \approx 150MeV$. Above the phase transition, the quarks and gluons form a plasma while below they are bound in hadrons, such as protons and neutrons.

Since the early universe also once had this temperature, one might hope that experimental signatures can be found in e.g. the CMBR. However, it seems this is not the case, all signatures are probably washed out. Fortunately, in contrast to baryogenesis, the formation can actually be studied in the laboratory, by colliding heavy ions of gold, lead, or uranium, at very high speeds. Because of the very high speeds the ions are Lorentz contracted to very flat "pancakes". These go through each other leaving behind a small, highly energised region filled with quarks and gluons. Because of their interaction the energy is redistributed leading to thermalization. If this thermalization process is sufficiently fast and to a high enough temperature, a quark gluon plasma is formed. This in turn expands very rapidly, similar to the early universe, thereby cooling and passing the confining

phase transition, after which the quarks and gluons form hadrons, such as baryons and mesons. One of the difficult but central questions is to find experimental signatures which differentiate between a very hot gas of hadrons and a plasma of quarks and gluons. After careful re-examination of many data sets, the CERN SPS has found evidence for the formation of this plasma. Currently the RHIC accelerator at Brookhaven is acquiring data, giving much more information and in the near future, the LHC at CERN, will also start operating. For a review of evidence from SPS and some of the results from RHIC see [8].

1.2 NON-PERTURBATIVE PHYSICS IN REAL TIME

In all the examples discussed in the previous section, non-equilibrium phenomena such as phase transitions, played a crucial role. However, in many computer simulations and analytical calculations people make use of the equilibrium aspects by using the imaginary time formulation of quantum field theory. We will need a real-time formulation to study the non-equilibrium aspects. Furthermore in non-equilibrium processes it is not always possible to find a small parameter suitable to make perturbative expansions.Thermal processes, for example, in which the field can fluctuate from one classical minimum of the potential to the other, make non-perturbative methods necessary. Finally, the inclusion of a chemical potential in an imaginary time formulation forms a difficult obstacle for Monte Carlo simulations. Using real-time simulations may thus also give an alternative for equilibrium calculations.

1.2.1 APPROXIMATION SCHEMES

In order to do such calculations it is necessary to make approximations. One can make use of the high temperature and make an expansion in $1/T$. In the Bose-Einstein distribution, for example, given by

$$n(\omega_k) = \frac{1}{e^{\hbar\omega_k/T} - 1}, \tag{1.4}$$

the inverse temperature occurs in the same way as Planck's constant and the leading behaviour in a large T expansion will be the classical behaviour. One can use the classical equations of motion to describe the non-perturbative dynamics. It is not necessary to have a thermal state in order for this approximation to be reasonable, it suffices that the occupation numbers of the field quanta are large.

The classical approximation has given very useful results for the sphaleron rate (see [9] and [10] for the status in one and three spatial dimensions), thermalization after preheating [11, 12, 13], non-equilibrium electroweak baryogenesis [14, 15],

as well as for studies of equilibration and thermalization [16, 17, 18]. With the inclusion of fermions it has given encouraging results for finite density simulations [19, 20].

As mentioned earlier, this approximation is reasonable when the occupation numbers of the field quanta are large, but in field theory there are always modes with which this is not the case. For instance, at high temperatures the low momentum modes of the fields are highly occupied and follow the classical Boltzmann distribution, but at large momenta occupation numbers are low and the classical distribution differs significantly from the quantum Bose-Einstein distribution, thereby giving rise to Rayleigh-Jeans divergences. To some extent these can be ameliorated in scalar field theories [21, 22], but for gauge theories the problems are more severe [23, 24, 25].

Another class of approximations are the large-n approximations, which have been used for initial value problems, with $O(n)$-type models. In this approximation, which is good if n, the number of field components is large, the action is expanded in the small parameter $1/n$. The leading order has given useful results for the description of preheating dynamics in the early universe (see e.g. [26] and references therein) and for the possibly disoriented chiral condensate in heavy ion collisions [27, 28]. However, it is generally considered to contain insufficient scattering for describing thermalization at larger times. This will be improved in next order in $1/n$, where scattering comes into play, but full implementation in field theory is hard. Furthermore, within quantum mechanics one finds instabilities [29, 30], and it has been argued that systematically correcting in $1/n$ does not prevent the approximation to break down at times of order $\sqrt{n}$ [31]. On the other hand, Schwinger-Dyson-like approaches including scattering diagrams and 2PI Φ-derivable approaches (see for instance Ref. [32, 33, 34] and references therein) appear to give more favourable results and have been found to lead to thermalization in field theory [35, 36].

The leading order large n equations for the $O(n)$ model are almost identical to the Hartree approximation for the single component scalar field, and so the latter approximation is also not considered to be able to describe thermalization. Yet, one can improve on this by allowing the system to be arbitrarily inhomogeneous. This has the effect that particle-like excitations can scatter through the intermediary of a mean field fluctuating in time *and space*. This will be one of the main topics of this thesis.

1.2.2 THE HARTREE VERSUS CLASSICAL APPROXIMATION

Let us first review the Hartree approximation. It describes the dynamics in terms of a mean field and a two-point correlation function. It corresponds to a Gaussian density matrix in field space, centred around the mean field with a width given by

the two-point function (see e.g. [30]). The two-point function can be conveniently described in terms of a complete set of mode functions. For a homogeneous initial state the mean field is translationally invariant and the mode functions can be taken in the form of plane waves labelled by a wave vector $\mathbf{k}$. Typically, only mode functions in a narrow $|\mathbf{k}|$-band get excited by a time-dependent homogeneous mean field, through parametric resonance or spinodal instability, see for example [37] and references therein. The system equilibrates but does not thermalize in this approximation and particle distribution functions show resonance peaks instead of approaching the Bose-Einstein distribution (see for example [38]). In order for the system to thermalize, the particles should be able to scatter, while in the Hartree, just as in the leading $1/n$ approximation no direct scattering is present.

We can improve on this however, by writing the initial density operator as an ensemble of coherent states with generally *in*homogeneous mean fields and two-point functions, in this way we include indirect scattering via the modes of the inhomogeneous mean field. Before explaining this approach in detail, let us first clarify the motivation by comparing it with the classical approximation. Simulations in this case indicate no problem of principle with thermalization (see [16, 17, 18] for quantitative studies). Starting from an initial ensemble of classical field configurations $\rho_c[\varphi, \pi, t_{in}]$ (with canonical field variables φ and π), suitable observables are found to become distributed according to the classical canonical distribution $\exp(-\beta H[\varphi, \pi])$. This distribution will not be reached starting with strictly homogeneous realisations, because then the dynamics is that of a simple system with only two degrees of freedom, i.e. the spatially constant φ and π. As initial conditions aiming at thermalization these are unsuitable realisations, even if $\rho_c[\varphi, \pi, t_{in}]$ is homogeneous. The phase space distribution $\rho_c[\varphi, \pi, t]$ may be homogeneous, but realisations $\varphi(\mathbf{x}, t)$, $\pi(\mathbf{x}, t)$ are typically inhomogeneous. Viewing the Hartree approximation as a semi-classical improvement, we may expect that thermalization will improve if some analogies of classical realisations are used as initial states.

1.2.3 HARTREE ENSEMBLE APPROXIMATION

To implement the idea, we note that an arbitrary density operator can be formally written as a superposition of Gaussian pure states:[1]

$$\hat{\rho} = \int [d\varphi\, d\pi]\, \rho_q[\varphi, \pi]\, |\varphi, \pi\rangle\langle\varphi, \pi|. \tag{1.5}$$

Here the $|\varphi, \pi\rangle$ are coherent states centred around $\varphi(\mathbf{x}) = \langle\varphi, \pi|\hat{\varphi}(\mathbf{x})|\varphi, \pi\rangle$ and $\pi(\mathbf{x}) = \langle\varphi, \pi|\hat{\pi}(\mathbf{x})|\varphi, \pi\rangle$, and $\rho_q[\varphi, \pi]$ is a functional representing the density operator $\hat{\rho}$. We interpret the $|\varphi, \pi\rangle\langle\varphi, \pi|$ as "realisations" of $\hat{\rho}$. The distribution $\rho_q[\varphi, \pi]$

[1] Operators are indicated with a caret.

can be quite singular for non-classical states, but for suitable semi-classical states or thermal states it is positive and intuitively attractive [39, 40].

A thermal state like $\exp[-\beta\hat{H}]$ cannot be approximated very well by a Gaussian if there are nontrivial interactions. For example, with a double well potential there are in general multiple peaks in the field distribution, while a Gaussian has a single peak. But if in the decomposition (1.5) a Gaussian state $|\varphi,\pi\rangle\langle\varphi,\pi|$ has a reasonable weight, we can take it as an initial state and use the Hartree approximation to compute the time evolution. We can then compute time averages (as long as the approximation is good), and finally sum over initial states according to (1.5). Such a description is semi-classical in so far as the mean field describes a near-classical path and $\rho_q[\varphi,\pi]$ is positive. But note that in the Hartree approximation the Gaussian fluctuations (i.e. the modes comprising the two-point function, these are the "particle-like excitations" alluded to above) influence the "classical" field, i.e. the mean field of the "realisation".

So the full expectation values now consist of a quantum average using the Gaussian quantum density matrix $|\varphi,\pi\rangle\langle\varphi,\pi|$ and a classical average using the density functional $\rho_q[\varphi,\pi]$. Even if the full expectation values describe a homogeneous system, the realisations are in general inhomogeneous.

We have thus achieved four things. Firstly, we have made contact with the classical approximation. If the mean field in a coherent state is large compared to the width of the state, the Gaussian wave packet approximately follows a classical trajectory and the mean field can be thought of as a *classical* field. This then suggests that the individual coherent states in the ensemble may be referred to as "realisations". However, by using an ensemble of coherent states rather than classical fields, we might have a much better description for those modes that have low occupation numbers for which the classical dynamics is a poor approximation. Secondly, we have expressed a (typically non-Gaussian) initial density operator in terms of Gaussian states. These are optimal for the Hartree method, which we want to use to approximate the dynamics of these states. Thirdly, the mean fields in the individual coherent states are *inhomogeneous*, therefore the particles can interact with the inhomogeneous mean field, such that the energy may get distributed over the full momentum range. As we will see this leads to approximate thermalization in coarse grained distributions. Finally, there is another aspect which is relevant in this context. When non-perturbative field configurations (domain walls, skyrmions, sphalerons, kinks, etc.) play a role, these can be taken into account with inhomogeneous background fields (i.e. mean field realisations).

As an example for the expansion (1.5), we derive $\rho_q[\varphi,\pi]$ for a free scalar field at temperature $1/\beta$ in Appendix 2.A. The canonical distribution

$$\hat{\rho} = \exp(-\beta\hat{H}[\varphi,\pi]),$$

is represented as

$$\rho_q[\varphi,\pi] \propto \prod_{\mathbf{k}} \exp\left[-(e^{\beta\omega_{\mathbf{k}}}-1)(\pi_{\mathbf{k}}^2+\omega_{\mathbf{k}}^2\varphi_{\mathbf{k}}^2)/2\omega_{\mathbf{k}}\right], \tag{1.6}$$

where $\mathbf{k}$ labels the modes of the field with frequency $\omega_{\mathbf{k}}$.

There is another possible application for this method. For thermal equilibrium the functional $\rho_q[\varphi,\pi]$ is time-independent but it is not known for interacting systems. If the time evolution could be followed exactly, we would be able to reconstruct its microcanonical version, assuming the system is sufficiently strongly ergodic. With exact dynamics we can imagine starting from some initial $\rho_q[\varphi,\pi]$ which is reasonably close to the target distribution, wait for equilibration and subsequently compute time averages over an arbitrarily long time span. With only an approximation to the dynamics (Hartree), the distribution may deteriorate after some time and we may have to stop and start again.

Crucial questions are now: does the system equilibrate sufficiently in the Hartree approximation, such that results are insensitive to reasonable choices of the initial $\rho_q[\varphi,\pi]$? Does it thermalize approximately, e.g. do one-particle distribution functions get the appropriate thermal forms? How long does it take for the approximation to break down? And if the answers to these questions are sufficiently favourable, can we obtain a reasonable approximation to the target equilibrium distribution at intermediate times starting with a convenient initial one?

1.3 OUTLINE OF THE THESIS

We will review the Hartree approximation in Chapter 2, deriving the equations of motion for the 1+1 dimensional φ^4 model, in terms of a mean field and mode functions. These equations can also be derived from an effective Hamiltonian, which will be presented. Furthermore this Hamiltonian possesses certain symmetries, following from the Hartree approximation, which lead to conserved charges. We will derive the equilibrium states for the system, which motivate the introduction of coarse grained particle numbers and frequencies, which will be the main observables used in this chapter. Since all our results are obtained using lattice field theory, we will discuss some of the peculiarities. The numerical results shown in this chapter will include a Monte Carlo, to verify the prediction of an approximate Bose-Einstein thermal distribution in our interacting model and most importantly, we will show that our Hartree Ensemble Approximation is capable of approximately reaching this state. This chapter is based on [41], except for Section 2.6, which appeared in [42] and Section 2.7.1, which appeared in [43].

In Chapter 3 we will further investigate the model, focusing on the different time scales present. We will differentiate between weak and strong coupling. Fur-

thermore we will show, that in 1+1 dimensions, the plasmon damping rate shows a very different behaviour from that in 3+1 dimensions. We will perform a calculation, and compare the results with our numerical simulations. Another topic discussed in this chapter will be numerical optimisations of the method. The computational cost of updating all the inhomogeneous mode functions is high, and makes it practically impossible to go to higher dimensions. We will investigate the possibility of reducing the number of modes and make a comparison with the limit of no mode functions at all: the classical approximation. This chapter is based on [43], except for Section 3.4, which appeared as two separate publications in [44, 45].

In Chapters 2 and 3 we mainly discussed the "broken phase" of the theory. However, we also found that in many aspects the "symmetric phase" behaves quite differently. This will be investigated in detail in Chapter 4, both numerically and analytically. This chapter is based on [42].

The ϕ^4 theory contains nontrivial topologically stable solutions, kinks. They are the topic for the final Chapter 5. We will compare their dynamics in the Hartree and classical approximations, starting from stationary or colliding kink antikink configurations.

CHAPTER 2

TOWARDS EQUILIBRIUM

In this chapter we will introduce the Hartree approximation, applied to the $\lambda\varphi^4$ model. We will discuss the equilibrium states using the effective potential and calculate the full quantum equilibrium state using a Monte Carlo simulation.

In order to describe the equilibration behaviour, we need to resort to approximations, of which on the one hand the classical and on the other hand the large n and Hartree are the most commonly used. In order to study quantum equilibration, one is forced to use one of the latter two. To prevent subtleties with would-be Goldstone bosons, we only consider the Hartree approximation.

When using homogeneous initial conditions, Hartree (Gaussian) dynamical approximations are known to have problems with thermalization, because of insufficient scattering. We attempt to improve on this by writing an arbitrary density matrix as a superposition of Gaussian pure states and applying the Hartree approximation to each member of such an ensemble. Particles can then scatter via their back-reaction on the typically inhomogeneous mean fields.

We will numerically study this Hartree ensemble approximation, starting from initial states which are far from equilibrium and numerically compute the time evolution of particle distribution functions. We will see that they do indeed display approximate thermalization on intermediate time scales by approaching a Bose-Einstein (BE) form. However, for very large times the distributions drift towards classical-like equipartition. We will study a very small system at strong coupling for a long period of time in order to obtain the final equilibrium distribution.

2.1 GAUSSIAN APPROXIMATION

We will study the $\lambda\varphi^4$ theory, which has the following action[1]

$$\mathcal{L} = -\partial_\mu \varphi \partial^\mu \varphi - \frac{1}{2}\mu^2\varphi^2 - \frac{1}{4}\lambda\varphi^4, \tag{2.1}$$

resulting in the following Heisenberg field equation for the quantum field at times $x^0 > 0$,

$$(-\partial^2 + \mu^2)\hat{\varphi}(x) + \lambda\hat{\varphi}(x)^3 = 0. \tag{2.2}$$

For exact evaluation we would have to specify the infinite set of matrix elements of $\hat{\varphi}(\mathbf{x}, 0)$ and $\partial_0\hat{\varphi}(\mathbf{x}, 0)$ as initial conditions. In practise, of course, less detail is needed. Taking the expectation value in an initial state at time $x^0 = 0$ leads to

$$\langle\hat{\varphi}(x)\rangle = \varphi(x), \tag{2.3a}$$

$$\langle T\hat{\varphi}(x_1)\hat{\varphi}(x_2)\rangle = \varphi(x_1)\varphi(x_2) - iG(x_1, x_2), \tag{2.3b}$$

$$\begin{aligned}\langle T\hat{\varphi}(x_1)\hat{\varphi}(x_2)\hat{\varphi}(x_3)\rangle &= \varphi(x_1)\varphi(x_2)\varphi(x_3) - i\varphi(x_1)G(x_2, x_3) + 2 \text{ perm.} \\ &\quad + (-i)^2 G(x_1, x_2, x_3),\end{aligned} \tag{2.3c}$$

$$\begin{aligned}\langle T\hat{\varphi}(x_1)\cdots\hat{\varphi}(x_4)\rangle &= \varphi(x_1)\cdots\varphi(x_4) - i\varphi(x_1)\varphi(x_2)G(x_3, x_4) + 6 \text{ perm.} \\ &\quad + \varphi(x_1)(-i)^2 G(x_2, x_3, x_4) + 3 \text{ perm.} \\ &\quad + (-i)^2 G(x_1, x_2)G(x_3, x_4) + 2 \text{ perm.} \\ &\quad + (-i)^3 G(x_1, \ldots, x_4),\end{aligned} \tag{2.3d}$$

etc. Here T denotes time ordering and

$$\langle\hat{\varphi}(x_1)\cdots\hat{\varphi}(x_n)\rangle \equiv \operatorname{Tr}\hat{\rho}\,\hat{\varphi}(x_1)\cdots\hat{\varphi}(x_n), \tag{2.4}$$

where $\hat{\rho}$ is the initial density operator; φ is the mean field (or classical field) and the $G's$ are correlation functions (connected Green functions). Taking the expectation value of (2.2) and neglecting the three point correlation function $G(x, x, x)$ gives the approximate equation

$$[-\partial^2 + \mu^2 + \lambda\varphi(x)^2 - 3i\lambda G(x, x)]\varphi(x) = 0. \tag{2.5}$$

To use it we need an equation for the two-point function. Such an equation can be found by multiplying (2.2) by $\hat{\varphi}(y)$ and taking again the expectation value in the initial state. This leads to the approximate equation

$$[-\partial^2 + \mu^2 + 3\lambda\varphi(x)^2 - 3i\lambda G(x, x)]\, G(x, y) = \delta^4(x - y), \tag{2.6}$$

[1] Throughout this thesis I will use the metric $g_{\mu\nu} = \operatorname{diag}(-1, 1, 1, 1)$, in this section we assume 3+1 dimensions.

where we used the canonical commutation relations and dropped the three and four-point correlation functions. We shall comment on their neglect at the end of this section. Since only the two-point function appears, equations (2.5), (2.6) are exact if the Hamiltonian and density matrix are approximated by Gaussian forms. Given the neglect of the higher correlation functions the initial density matrix does not have to be Gaussian *per se*, but its non-Gaussianity does not enter in eqs. (2.5), (2.6). For clarity we shall now assume the bra-kets $\langle\cdots\rangle$ to refer to a *Gaussian density operator* $\hat{\rho}$. Later we will consider non-Gaussian operators by further averaging over initial conditions, as in (1.5), which will be indicated by $\overline{\langle\cdots\rangle}$.

An intuitive as well as practical way of computing the two-point function, is in terms of mode functions $f_\alpha(x)$. We write

$$-iG(x,y) = \theta(x^0-y^0)C(x,y) + \theta(y^0-x^0)C(y,x), \tag{2.7}$$

such that

$$C(x,y) = \langle[\hat{\varphi}(x)-\varphi(x)][\hat{\varphi}(y)-\varphi(y)]\rangle. \tag{2.8}$$

It follows from (2.6) that $C(x,y)$ satisfies the homogeneous equation (i.e. $\delta^4(x-y)\to 0$), in the variable x as well as in y, as if $\hat{\varphi}(x)-\varphi(x)$ satisfies this equation. We can now introduce mode functions $f_\alpha(x)$, satisfying the homogeneous equation

$$[-\partial^2+\mu^2+3\lambda\varphi(x)^2+3\lambda C(x,x)]\,f_\alpha(x) = 0, \tag{2.9}$$

($-iG(x,x) = C(x,x)$) and write:

$$\hat{\varphi}(x) \overset{\text{g.a.}}{=} \varphi(x) + \sum_\alpha \left[\hat{b}_\alpha f_\alpha(x) + \hat{b}^\dagger_\alpha f^*_\alpha(x)\right]. \tag{2.10}$$

where the $\hat{b}_\alpha$ and $\hat{b}^\dagger_\alpha$ are spacetime independent and "g.a." means "Gaussian approximation". The wave equation (2.9) for the f_α is of the Klein-Gordon type and we require the mode functions to be orthogonal and complete in the Klein-Gordon sense (using finite volume notation),

$$\int d^3x\ [f^*_\alpha(x)i\partial_0 f_\beta(x) - i\partial_0 f^*_\alpha(x) f_\beta(x)] = \delta_{\alpha\beta}, \tag{2.11a}$$

$$\int d^3x\ [f_\alpha(x)i\partial_0 f_\beta(x) - i\partial_0 f_\alpha(x) f_\beta(x)] = 0, \tag{2.11b}$$

$$\sum_\alpha [-if_\alpha(x)\partial_0 f^*_\alpha(y) + if^*_\alpha(x)\partial_0 f_\alpha(y)]_{x^0=y^0} = \delta^3(\mathbf{x}-\mathbf{y}), \tag{2.11c}$$

$$\sum_\alpha [f_\alpha(x)f^*_\alpha(y) - f^*_\alpha(x)f_\alpha(y)]_{x^0=y^0} = 0, \tag{2.11d}$$

$$\sum_\alpha [\partial_0 f_\alpha(x)\partial_0 f^*_\alpha(y) - \partial_0 f^*_\alpha(x)\partial_0 f_\alpha(y)]_{x^0=y^0} = 0. \tag{2.11e}$$

The above orthogonality and completeness relations are preserved by the equation of motion (2.9) for the f_α. The canonical commutation relations for $\hat{\varphi}$ and $\partial_0\hat{\varphi}$ translate into

$$[\hat{b}_\alpha, \hat{b}^\dagger_\beta] = \delta_{\alpha\beta}, \qquad [\hat{b}_\alpha, \hat{b}_\beta] = [\hat{b}^\dagger_\alpha, \hat{b}^\dagger_\beta] = 0. \tag{2.12}$$

The initial condition implies $\langle \hat{b}_\alpha \rangle = 0$ and we have to specify $E_{\alpha\beta} \equiv \langle \hat{b}_\alpha \hat{b}_\beta \rangle$ and $N_{\alpha\beta} \equiv \langle \hat{b}^\dagger_\alpha \hat{b}_\beta \rangle$. The matrices N and E are subject to constraints which follow from their definition as expectation values of operators in Hilbert space. We shall assume that a Bogoliubov transformation $\hat{b}_\alpha \to \sum_\beta [A_{\alpha\beta}\hat{b}_\beta + B_{\alpha\beta}\hat{b}^\dagger_\beta]$ can be made such that $E_{\alpha\beta} \to 0$ and $N_{\alpha\beta} \propto \delta_{\alpha\beta}$. This transformation produces new mode functions which are linear combinations of the f and f^*. In the new basis we only have to specify as initial conditions

$$\langle \hat{b}^\dagger_\alpha \hat{b}_\beta \rangle \equiv n^0_\alpha \, \delta_{\alpha\beta}, \qquad n^0_\alpha \geq 0, \tag{2.13}$$

in terms of which

$$C(x,y) = \sum_\alpha \left[(1 + n^0_\alpha) f_\alpha(x) f^*_\alpha(y) + n^0_\alpha f^*_\alpha(x) f_\alpha(y) \right]. \tag{2.14}$$

Equation (2.10) expresses the fact that in the Gaussian approximation the field $\hat{\varphi}'(x) \equiv \hat{\varphi}(x) - \varphi(x)$ is a generalised free field, i.e. its correlation functions are completely determined by the two-point function. Its linear field equation (i.e. (2.9) with $f_\alpha \to \hat{\varphi}'$) is equivalent to the Heisenberg equations of motion of the effective Gaussian Hamiltonian operator

$$\hat{H}_{\text{g.a.}} = \int d^3x \left[\frac{1}{2}\hat{\pi}'^2 + \frac{1}{2}(\nabla\hat{\varphi}')^2 + \frac{1}{2}m^2_{\text{eff}}\hat{\varphi}'^2 + \epsilon_{\text{eff}} \right], \tag{2.15}$$

where the spacetime dependent effective mass m^2_{eff} is given by

$$m^2_{\text{eff}}(x) = 3\lambda\varphi(x)^2 + 3\lambda C(x,x). \tag{2.16}$$

We also introduced an effective c-number energy density ϵ_{eff}, which is determined by requiring $\langle \hat{H}_{\text{g.a.}} \rangle = \langle \hat{H} \rangle$:

$$\epsilon_{\text{eff}}(x) = \frac{1}{2}\pi(x)^2 + \frac{1}{2}[\nabla\varphi(x)]^2 + \frac{1}{2}\mu^2\varphi(x)^2 + \frac{1}{4}\lambda\varphi(x)^4 - \frac{3}{4}\lambda C(x,x)^2. \tag{2.17}$$

Summarising, the Gaussian approximation consists of the equations (2.5), (2.9), (2.13) and (2.14), together with the orthogonality and completeness conditions (2.11) for the mode functions and some initial condition for the mean field and mode

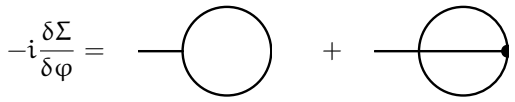

Figure 2.1: Diagrammatic illustration of $\delta\Sigma/\delta\varphi$, with Σ the self-energy functional defined by $\Gamma = S - \Sigma$. The lines and full dots represent the exact propagators (correlation functions) and vertex functions, the other vertices represent the bare vertex functions as given by the classical action S.

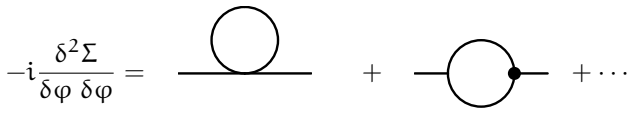

Figure 2.2: Diagrams for the self-energy part of the inverse correlation function $G^{-1} = -\delta^2 S/\delta\varphi\,\delta\varphi + \delta^2\Sigma/\delta\varphi\,\delta\varphi$. The $\cdots$ represent the two-loop diagrams obtained by differentiating the diagrams in Fig. 2.1.

functions. For the sake of clarity we write down the equations of motion again, explicitly specifying space and time derivatives:

$$\ddot{\varphi} = \Delta\varphi - [\mu^2 + \lambda\varphi^2 + 3\lambda C]\varphi, \tag{2.18a}$$

$$\ddot{f}_\alpha = \Delta f_\alpha - [\mu^2 + 3\lambda\varphi^2 + 3\lambda C] f_\alpha, \tag{2.18b}$$

with

$$C = \sum_\alpha (2n^0_\alpha + 1)|f_\alpha|^2, \qquad n^0_\alpha = \langle \hat{b}^\dagger_\alpha \hat{b}_\alpha \rangle. \tag{2.18c}$$

The Gaussian approximation can be justified in the limit of large n for the $O(n)$ model. The resulting field equations are very similar: we only need to make the replacement $3 \to 1$ in eqs. (2.5) and (2.9).

The above derivation in terms of the Heisenberg equations of motion can be put into the systematic framework of the Dyson-Schwinger hierarchy. These equations follow from functionally differentiating an exact equation of motion $\delta\Gamma/\delta\varphi = -J$ with respect to J and setting $J = 0$ afterwards. Here Γ is the effective action (with time integration along the usual Keldysh-Schwinger contour) and J an external source. We shall not go into details here, instead we just comment on the systematics, using diagrams (for a derivation, see for instance Ref. [46]). Fig. 2.1 illustrates

the exact equation for the mean field. The Gaussian approximation (2.5) is obtained by dropping the two-loop diagram. By differentiating the diagrams in Fig. 2.1 we get the exact equation for the two-point correlation function illustrated in Fig. 2.2. The Gaussian approximation (2.6) can be obtained from this by: a) dropping the two-loop contributions and b) dropping the second one-loop diagram. The neglect of the two-loop terms may be reasonable at weak coupling, and even the second approximation may be justifiable if the product of the three point couplings (one bare, the other dressed) is substantially smaller than the (bare) four point coupling in the first one-loop diagram. However, since the bare three point vertex $\delta^3 S/\delta\varphi^3 \propto \lambda\varphi$, we see that this is not likely if $\varphi = O(\lambda^{-1/2})$ or larger. Especially this second approximation b) is worrisome, because on iteration of the integral equations we would not get all one-loop diagrams correctly . It also has been established that the approximation does not give exact Goldstone bosons where one expects them, because the phase transition is incorrectly predicted to be first order, instead of second order (in 3+1 D) or a cross over (1+1 D). There is a problem with renormalization in 3+1 dimensions [47] (but not in 1+1 D).

It will depend on the circumstances if these troublesome features of the Hartree approximation are numerically important.

2.2 EFFECTIVE HAMILTONIAN AND CONSERVED CHARGES

The equations of the Gaussian approximation derived in Section 2.1 are local in time and they may be derived from a conserved effective Hamiltonian. We shall present it here and exhibit its symmetries and accompanying conserved charges. We write

$$f_\alpha(x) = \frac{1}{\sqrt{2}}\Big[f_{\alpha 1}(x) - i\, f_{\alpha 2}(x)\Big], \tag{2.19}$$

$$\xi_{\alpha a}(x) = \Big(\frac{1}{2} + n^0_\alpha\Big)^{1/2} f_{\alpha a}(x), \qquad a = 1, 2. \tag{2.20}$$

$$\eta_{\alpha a}(x) = \partial_0 \xi_{\alpha a}(x), \qquad \pi(x) = \partial_0 \varphi(x). \tag{2.21}$$

In terms of the real canonical variables φ, π, $\xi_{\alpha a}$ and $\eta_{\alpha a}$ the effective Hamiltonian takes the form

$$\begin{aligned} H_{\text{eff}} = \int d^3x \Big[&\frac{1}{2}\left(\pi^2 + \eta^2 + (\nabla\varphi)^2 + (\nabla\xi)^2\right) + \\ &\frac{1}{2}\mu^2\left(\varphi^2 + \xi^2\right) + \frac{1}{4}\lambda\left(\varphi^4 + 6\varphi^2\xi^2 + 3(\xi^2)^2\right)\Big], \end{aligned} \tag{2.22}$$

where

$$\xi^2 = \sum_\alpha \left(\xi_{\alpha 1}^2 + \xi_{\alpha 2}^2\right), \tag{2.23a}$$

$$(\nabla\xi)^2 = \sum_\alpha \left[(\nabla\xi_{\alpha 1})^2 + (\nabla\xi_{\alpha 2})^2\right], \tag{2.23b}$$

$$\eta^2 = \sum_\alpha \left(\eta_{\alpha 1}^2 + \eta_{\alpha 2}^2\right). \tag{2.23c}$$

It is easy to check that the mean field equation (2.5) and the mode equations (2.9) are equivalent to the Hamilton equations

$$\partial_0\varphi = \pi, \qquad \partial_0\pi = -\frac{\delta H_{\text{eff}}}{\delta\varphi}, \qquad \partial_0\xi_{\alpha a} = \eta_{\alpha a}, \qquad \partial_0\eta_{\alpha a} = -\frac{\delta H_{\text{eff}}}{\delta\xi_{\alpha a}}. \tag{2.24}$$

It is also straightforward to show that H_{eff} is just the expectation value of the quantum Hamiltonian

$$\hat{H}(t) = \int d^3x \left[\frac{1}{2}\hat{\pi}^2 + \frac{1}{2}(\nabla\hat{\varphi})^2 + \frac{1}{2}\mu^2\hat{\varphi}^2 + \frac{1}{4}\lambda\hat{\varphi}^4\right], \tag{2.25}$$

upon inserting the Gaussian approximation (2.10),

$$H_{\text{eff}} = \langle\hat{H}\rangle. \tag{2.26}$$

The effective Hamiltonian has evidently a large symmetry, corresponding to rotations of the infinite dimensional vectors $\xi_{\alpha a}$ and $\eta_{\alpha a}$. For definiteness, let us assume a regularisation of the field theory such that there are M modes, $\alpha = 1, \ldots, M$ (e.g. on an N^3 periodic lattice $M = N^3$). Then the effective Hamiltonian has $O(2M)$ symmetry, implying $M(2M-1)$ conserved generalised angular momenta of the general form

$$L_{\alpha a,\beta b} = \int d^3x \, (\xi_{\alpha a}\eta_{\beta b} - \xi_{\beta b}\eta_{\alpha a}), \qquad (\alpha, a) \neq (\beta, b). \tag{2.27}$$

Recalling the orthonormality relations for the mode functions, (2.11a) and (2.11b), we see that the conserved quantities are given in terms of the initial conditions as

$$L_{\alpha 1,\alpha 2} = \frac{1}{2} + n_\alpha^0, \tag{2.28}$$

with all others vanishing.

It is interesting to compare with the effective Hamiltonian corresponding to the large n limit of the $O(n)$ model [48], which may be obtained from H_{eff} above by the

replacement $3 \to 1$ (and $6 \to 2$). This has the effect of producing the combination $\lambda(\varphi^2+\xi^2)^2$, so the symmetry enlarges to $O(2M+1)$. The additional $2M$ conserved generalised angular momenta depend on the initial conditions for φ and π.[2]

2.3 EQUILIBRIUM STATES

In a first exploration of the system and of the Gaussian approximation we study equilibrium states, i.e. stationary states with maximum entropy. This will give information on the phase structure and quasi-particle excitations as a function of temperature. From now on we will restrict to 1+1 dimensions, $x^\mu \to (t,x)$, and assume the system to be confined to a "volume" L with periodic boundary conditions. The coupling λ needs no renormalization while the bare mass parameter μ^2 is only logarithmically divergent in the implicit cutoff.

We assume the equilibrium states to be homogeneous and time-independent, i.e. $\varphi(t,x)=v$ and $C(t,x;t,y)=C(0,x-y;0,0)$. Also the various time derivatives of C evaluated at equal times are assumed to be time-independent. We shall seek solutions of the form (2.14) in which the mode functions are plane waves,

$$\varphi(t,x) = v, \tag{2.29a}$$

$$f_k(t,x) = \frac{e^{ikx-i\omega_k t}}{\sqrt{2\omega_k L}}. \tag{2.29b}$$

Here the label α has become the wave number k and we write n_k for the corresponding (time independent) occupation numbers. With this ansatz the equations for the mean field and mode functions reduce to

$$(\mu^2 + 3\lambda C + \lambda v^2)v = 0, \tag{2.30}$$

$$-\omega_k^2 + k^2 + \mu^2 + 3\lambda C + 3\lambda v^2 = 0, \tag{2.31}$$

where $C = C(t,x;t,x)$ is time-independent. In the infinite volume limit it is given by

$$C = \int \frac{dk}{2\pi}\left(n_k + \frac{1}{2}\right)\frac{1}{\omega_k}. \tag{2.32}$$

It follows that

$$\omega_k^2 = m^2 + k^2, \qquad m^2 = \mu^2 + 3\lambda C + 3\lambda v^2. \tag{2.33}$$

[2] In [48] the effective Hamiltonian for the homogeneous system was expressed in terms of the radial variable $\xi_\alpha = (\xi_{\alpha 1}^2 + \xi_{\alpha 2}^2)^{1/2}$ (modulo a factor of two), and the rotational symmetries mixing $\xi_{\alpha 1}$ and $\xi_{\alpha 2}$ are then absent. However, the corresponding equations of motion then suffer from numerical complications due to the angular momentum barriers.

To determine the n_k we maximise the entropy S subject to the constraint of fixed energy $U \equiv H_{\text{eff}} = E$, i.e. maximise $S + \beta(E - U)$, with Lagrange multiplier β. We shall write these equations in terms of the densities $s = S/L$, $u = U/L$, $\epsilon = E/L$ with $L \to \infty$. The (unrenormalized) energy density u is given by

$$u = \frac{H_{\text{eff}}}{L} = \frac{1}{2}\mu^2\nu^2 + \frac{1}{4}\lambda\nu^4 + \int \frac{dk}{2\pi}\left(n_k + \frac{1}{2}\right)\frac{\omega_k^2 + k^2 + \mu^2 + 3\lambda\nu^2}{2\omega_k} + \frac{3}{4}\lambda C^2, \quad (2.34)$$

and for our Gaussian density operator, s can be written as

$$s = -\frac{1}{L}\operatorname{Tr}\rho\log\rho = \int \frac{dk}{2\pi}\left[(n_k+1)\log(n_k+1) - n_k\log n_k\right]. \quad (2.35)$$

The maximisation equations read

$$0 = \frac{\delta[s + \beta(\epsilon - u)]}{\delta n_k} = \log\left(\frac{n_k+1}{n_k}\right) - \beta\omega_k, \qquad u = \epsilon, \quad (2.36)$$

with the solution

$$n_k = \frac{1}{e^{\beta\omega_k} - 1} \quad (2.37)$$

and β such that $u = \epsilon$. So we found equilibrium states of the Hartree evolution corresponding to the Bose-Einstein distribution with temperature $T = \beta^{-1}$. All effects of the interaction are buried in the temperature dependent mass m introduced in (2.33).

For simplicity of discussion, let us next use a simple momentum cutoff $|k| < \Lambda$ and define a renormalized mass parameter μ_r^2 by combining the logarithmically divergent vacuum value of the mode sum (2.32) at the point $m^2 = \lambda$ with the bare mass parameter μ^2:

$$\mu_r^2 = \mu^2 + 3\lambda C(m^2 = \lambda, n_k = 0). \quad (2.38)$$

To leading order, μ_r^2 is given by

$$\mu_r^2 = \mu^2 + \frac{3\lambda}{4\pi}\log\frac{4\Lambda^2}{\lambda}. \quad (2.39)$$

and (2.33) takes the renormalized form

$$m^2 = \mu_r^2 + \frac{3\lambda}{4\pi}\log\frac{\lambda}{m^2} + 3\lambda\int_0^\infty \frac{dk}{\pi}\,\frac{1}{\sqrt{m^2+k^2}}\,\frac{1}{e^{\sqrt{m^2+k^2}/T} - 1} + 3\lambda\nu^2. \quad (2.40)$$

At zero temperature the equilibrium state is the vacuum. For $\nu = 0$ there is one solution m^2 for every $\mu_r^2 \in (-\infty, \infty)$

$$\mu_r^2 = m^2 + \frac{3\lambda}{4\pi}\log\frac{m^2}{\lambda}. \quad (2.41)$$

For nonzero v we get, from (2.30), the relations

$$m^2 = 2\lambda v^2, \qquad \mu_r^2 = -\frac{1}{2}m^2 + \frac{3\lambda}{4\pi}\log\frac{m^2}{\lambda}. \tag{2.42}$$

The right hand side of this equation has a maximum for $m^2/\lambda = 3/(2\pi)$, meaning there are *two* solutions, provided

$$\frac{\mu_r^2}{\lambda} < \frac{3}{4\pi}\Big[-1 + \log\Big(\frac{3}{2\pi}\Big)\Big] \approx -0.415, \tag{2.43}$$

otherwise there are none. To determine the true ground state we plot in Fig. 2.3a the effective potential u as a function of φ (i.e. with m^2 the solution of (2.40), with $v \to \varphi$ and at $T = 0$), for various μ_r. The plot shows that there is a first order phase transition as a function of μ_r^2, instead of the expected second order transition for a model in the universality class of the Ising model. This mis-representation of the phase transition is a well-known artifact of the Gaussian approximation (see, e.g. Ref. [47]).

Note that the second order transition would occur at strong coupling $\lambda/m^2 \to \infty$, where the Gaussian approximation is suspect. In fact, the two masses at the transition also imply strong coupling: they are given by $\lambda/m^2 \approx 10$, for $\varphi = 0$ and $\lambda/m^2 \approx 1.2$ for $\varphi = v_c \approx 0.65$. To avoid fake first order effects we should evidently choose parameters away from the transition region. For this paper we mostly used $\lambda/m^2 = 1/12$ for which there is only one ground state at $v^2 = 6$, well away from $v_c \approx 0.65$.

Having determined the groundstate we define the renormalized energy $H_{\text{eff,r}}$ by subtracting from H_{eff} its value in the ground state, such that the vacuum energy is zero. It can be instructive to split the total energy into a classical (Gaussian mean field) part and a mode energy, $H_{\text{eff,r}} = H_{\text{mf}} + H_{\text{modes}}$. We define the mean field part as

$$H_{\text{mf}} = \int dx \, \left[\frac{1}{2}\pi^2 + \frac{1}{2}(\nabla\varphi)^2 + V_{\text{mf}}(\varphi)\right], \tag{2.44a}$$

$$V_{\text{mf}}(\varphi) = \begin{cases} \frac{1}{2}m^2\varphi^2 + \frac{1}{4}\lambda\varphi^4, & v = 0, \\ \frac{1}{4}\lambda\left(\varphi^2 - v^2\right)^2, & v \neq 0, \end{cases} \tag{2.44b}$$

where m^2 and v^2 are the vacuum values (i.e. at $T = 0$).

Consider now starting in the broken symmetry phase $v \neq 0$ at zero temperature and raising the temperature. In 1+1 dimensions there should be only a cross over and not a true phase transition. Fig. 2.3b shows the finite temperature effective potential (free energy density)

$$f(\varphi) = u(\varphi) - Ts(\varphi), \tag{2.45}$$

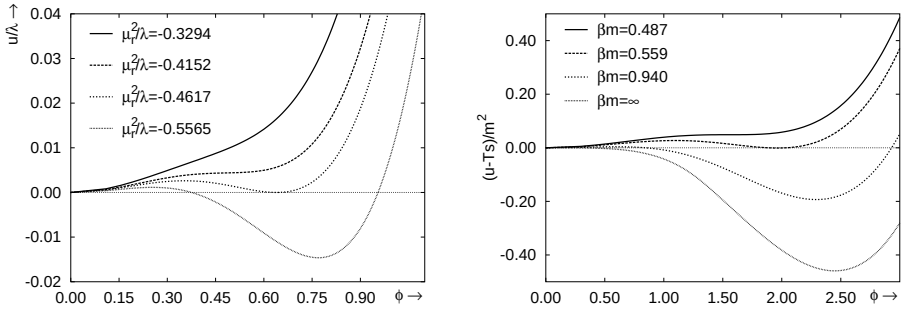

a: Zero temperature effective potential $u/\lambda = H_{\rm eff}/L\lambda$ for various values of μ_r^2/λ.

b: Finite temperature effective potential $f/m_0^2 = (u - Ts)/m_0^2$ for various values of βm_0 at a coupling $\lambda/m_0^2 = 1/12$ ($m_0 = m(v, T = 0)$).

Figure 2.3: Effective potential versus φ, normalised to zero at $\varphi = 0$.

using the temperature T as independent variable instead of μ_r^2. Now $m^2 = m^2(\varphi, T)$ is the solution of (2.40), $v \to \varphi$, at finite T. The parameters were chosen such that $v^2 = m^2(v, 0)/2\lambda = 6$ at $T = 0$. We see again a fake first order transition, at $T_c \approx 1.79\, m(v, 0)$, with $v_c = 1.96$. Its latent heat ℓ and surface tension σ are given by

$$\ell = \delta u = 0.39\, m(v, 0)^2, \qquad \sigma = \int_0^{v_c} d\varphi\, \sqrt{2f(\varphi)} = 0.295\, m(v, 0). \tag{2.46}$$

These are not particularly small values and we may not argue that the effects of the first order transition will be negligible under generic circumstances. However, in 1+1 dimensions, the critical size of a nucleating bubble is zero, so the bubble nucleation rate is not suppressed ($\propto \exp(-2\sigma/T_c) \approx \exp(-0.17)$) and supercooling will not be strong.

We end this section with some cautionary remarks. First, the fact that the equilibrium correlation function $C(x, y)$ has the free form (i.e. eq. (2.47), below, with n_k given by the Bose-Einstein form (2.37)) is a result of the Gaussian approximation. The exact correlation function will have a more complicated form, although the corrections are expected to be small at weak coupling. We will check this explicitly by a Monte Carlo computation discussed in Section 2.7.1.

Second, it is not clear that the finite temperature equilibrium state found above will actually be approached at very large times. Any set of numbers n_k in conjunction with eqs. (2.29)–(2.34) gives a stationary solution to the Hartree equations.

Our derivation of the Bose-Einstein form for n_k, used the standard form (2.35) for the entropy, but we have not shown that this entropy is a large time result of the dynamics. Of course, this would be trivially the case if we choose the initial occupation numbers $n^0_\alpha = n_k$. But for a generic Gaussian initial state the correlation function may still approach a fixed point of the form just discussed ($t \approx t'$),

$$C(t,x;t',x') = \sum_\alpha \Big[(1+n^0_\alpha) f_\alpha(t,x) f^*_\alpha(t',x') + n^0_\alpha f^*_\alpha(t,x) f_\alpha(t',x')\Big]$$
$$\to \int \frac{dk}{2\pi}\Big[\frac{1+n_k}{2\omega_k}\, e^{ik(x-x')-i\omega_k(t-t')} + \frac{n_k}{2\omega_k}\, e^{-ik(x-x')+i\omega_k(t-t')}\Big], \quad (2.47)$$

where the n_k are expected to correspond to maximum entropy in relation to the dynamics. Since the Hartree dynamics in terms of H_{eff} is classical we may expect this entropy to take a classical form, which would lead to

$$n_k = \frac{T}{\omega_k}. \quad (2.48)$$

However, matters are complicated by the presence of the infinitely many conserved charges (2.28), which are determined by the initial conditions. Note that without these constraints one would expect $n_k + 1/2 = T/\omega_k$, instead of (2.48), which makes a big difference because equipartition suggests low $T = O(\epsilon/\lambda)$ and therefore *small* n_k. We elaborate on this in Appendix 2.B.

To study such matters numerically we now first introduce a coarse graining of the correlation function and define a corresponding time dependent distribution function $n_k(t)$.

2.4 COARSE GRAINED PARTICLE NUMBERS

The mode functions may be interpreted as representing particles which interact through the mean field. This is similar to electrons scattering off each other in classical electrodynamics, albeit that here the "particles" are treated quantum mechanically and their interaction is short ranged. Intuitively, such an interpretation supposes that the particles are localised, with a correspondingly fluctuating (and hence inhomogeneous) mean field taking the role of a classical field.

Within such a picture one expects the system to thermalize approximately. We would like such thermalization to be quantal, e.g. with particle distribution functions which are of the Bose-Einstein type. However, the fact that our equations of motion have the form of classical Hamilton equations in terms of H_{eff} suggests otherwise, namely a distribution approaching a classical Boltzmann form $\exp(-\beta H_{\text{eff}})$, subject to the constraints set by the large number of conserved charges (2.27). But

this may take a very long time. In any case, one way to test the Gaussian approximation is to study its thermalization properties.

This we do by looking at equal time correlation functions, which are coarse grained by averaging over a spacetime region. Assuming the system is weakly coupled we can compare such averages with a free field form in terms of quasi-particles with effective masses. If the system equilibrates locally in a quantum way, then the quasi-particle distribution n_k should approach the Bose-Einstein form. We define the correlation functions

$$S(t,x,y) = \overline{\langle\hat\varphi(t,x)\hat\varphi(t,y)\rangle} - \overline{\langle\hat\varphi(t,x)\rangle}\;\overline{\langle\hat\varphi(t,y)\rangle}, \tag{2.49a}$$

$$T(t,x,y) = \frac{1}{2}\overline{\langle[\hat\varphi(t,x)\hat\pi(t,y)+\hat\pi(t,y)\hat\varphi(t,x)]\rangle} - \overline{\langle\hat\varphi(t,x)\rangle}\;\overline{\langle\hat\pi(y,t)\rangle}, \tag{2.49b}$$

$$U(t,x,y) = \overline{\langle\hat\pi(t,x)\hat\pi(t,y)\rangle} - \overline{\langle\hat\pi(t,x)\rangle}\;\overline{\langle\hat\pi(t,y)\rangle}, \tag{2.49c}$$

where the overbar denotes the spacetime averaging as well as a possible average over initial conditions as in (1.5). Using (2.3a) and (2.8) we can express these quantities in terms of a "classical" (mean field) and a "quantum" contribution,

$$S(t,x,y) = S^c(t,x,y) + S^q(t,x,y), \tag{2.50a}$$

$$S^c(t,x,y) = \overline{\varphi(t,x)\varphi(t,y)} - \overline{\varphi(t,x)}\;\overline{\varphi(t,y)}, \tag{2.50b}$$

$$S^q(t,x,y) = \overline{C(t,x;t,y)}, \tag{2.50c}$$

etc. Note that $S^c \to 0$ in case of averaging over initial conditions and/or spacetime.

For simplicity the spatial average is performed over all of space. For example,

$$\overline{\langle\hat\varphi(t,x)\hat\varphi(t,y)\rangle} = \frac{1}{L\delta}\int_{t-\delta/2}^{t+\delta/2} dt' \int_0^L dz\,\langle\hat\varphi(t',x+z)\hat\varphi(t',y+z)\rangle. \tag{2.51}$$

Because of the periodic boundary conditions S, T and U depend only on the difference between x and y. Taking the Fourier transform

$$S_k(t) = \frac{1}{L}\int_0^L dx\,dy\,e^{-ik(x-y)}\,S(x,y,t), \qquad k = (0,\pm1,\pm2,\cdots)\frac{2\pi}{L}, \tag{2.52}$$

and similarly for T and U, it is easy to see that S and U are symmetric and positive, i.e.

$$S_k(t) = S_{-k}(t) \geq 0, \qquad\qquad U_k(t) = U_{-k}(t) \geq 0, \tag{2.53}$$

while T_k enjoys no such properties. For a free field with average occupation numbers $\langle\hat a_k^\dagger\hat a_k\rangle = n_k$ and frequencies ω_k the correlators are given by

$$S_k = \frac{n_k + n_{-k} + 1}{2\omega_k}, \qquad T_k = \frac{n_k - n_{-k}}{2}, \qquad U_k = S_k\omega_k^2. \tag{2.54}$$

Note that in this case T is antisymmetric. We now *define* $\omega_k(t)$ and $n_k(t)$ for the interacting case by

$$n_k(t) = n_k^s(t) + n_k^a(t), \qquad n_k^s(t) = n_{-k}^s(t), \qquad n_k^a(t) = -n_{-k}^a(t), \tag{2.55}$$

$$S_k(t) = \left[n_k^s(t) + \frac{1}{2}\right] \frac{1}{\omega_k(t)}, \tag{2.56a}$$

$$T_k^a(t) = \frac{1}{2}\left[T_k(t) - T_{-k}(t)\right] = n_k^a(t), \tag{2.56b}$$

$$U_k(t) = \left[n_k^s(t) + \frac{1}{2}\right] \omega_k(t). \tag{2.56c}$$

These equations can be easily solved in terms of ω_k and n_k:

$$\omega_k = \omega_{-k} = \sqrt{U_k/S_k} \qquad n_k^s = \omega_k S_k - \frac{1}{2} = \sqrt{U_k S_k} - \frac{1}{2} \tag{2.57}$$

and n_k follows by adding T_k^a. In practise n_k is positive (it can be shown to be positive provided the symmetric correlation between φ and π vanishes).

There is a more direct interpretation of these formulae in terms of the expectation value of a number operator $\hat{a}_k^\dagger \hat{a}_k$. Suppose we define time dependent creation and annihilation operators as

$$\hat{a}_k(t) = \frac{1}{\sqrt{2\omega_k(t)L}} \int_0^L dx\, e^{-ikx} \left[\omega_k(t)\hat{\varphi}(t,x) + i\hat{\pi}(t,x)\right], \tag{2.58a}$$

$$\hat{a}_k^\dagger(t) = \left(\hat{a}_k(t)\right)^\dagger. \tag{2.58b}$$

Then

$$\overline{\langle \hat{a}_k^\dagger(t)\hat{a}_k(t)\rangle} = n_k(t). \tag{2.59}$$

The problem with starting with (2.58) is that one does not know a priori how to choose the $\omega_k(t)$. This is especially so if some of the effective squared frequencies $\mu^2 + 3\lambda\varphi^2 + 3\lambda C$ in the equations for the mode functions turn negative. The line of reasoning leading to (2.55)–(2.56c) solves this problem, but we should keep in mind that this is by brute force, which can be misleading in extreme situations, e.g. when the spectral function is not dominated by a sufficiently narrow quasi-particle bump.

The quasi-particles can also be used to define an energy:

$$E_{qp} = \sum_k n_k \omega_k \tag{2.60}$$

where n_k can be obtained from the two-point functions of the mean field, of the mode functions, or of the sum of both. This definition can then be compared with the effective Hamiltonian.

2.5 HARTREE ENSEMBLE APPROXIMATION

Above we described the Hartree approximation. In the Hartree ensemble method this approximation is applied to each individual realisation $|\varphi,\pi\rangle\langle\varphi,\pi|$ of the initial conditions as in (1.5). So in eq. (2.8) the Gaussian brackets stand for $\langle\cdot\rangle = \langle\varphi,\pi|\cdot|\varphi,\pi\rangle$ and the average over φ,π is only taken in the evaluation of observables. Furthermore these states are pure, hence in (2.14), the initial particle density $n^0_\alpha = 0$.

In this way we compute correlation functions with a generally non-Gaussian density operator $\hat\rho = \sum_i p_i|\varphi^{(i)},\pi^{(i)}\rangle\langle\varphi^{(i)},\pi^{(i)}|$, as

$$S_{xy} = \sum_i p_i[C^{(i)}_{xy} + \varphi^{(i)}_x\varphi^{(i)}_y] - \Big(\sum_i p_i\varphi^{(i)}_x\Big)\Big(\sum_j p_j\varphi^{(j)}_y\Big). \tag{2.61}$$

The $C^{(i)}_{xy}$ and $\varphi^{(i)}_x$ are computed with Gaussian pure states as in (2.8). This means that in the time-evolution the Gaussian approximation is used, while expectation values are calculated using the more general initial density operator.

It should be stressed that for typical realisations the mean field $\varphi^{(i)}_x$ is *inhomogeneous* in space, in contrast to the ensemble average $\sum_i p_i\varphi^{(i)}_x$ which is in fact homogeneous for the initial conditions we shall employ.

2.6 IMPLEMENTATION ON A LATTICE

2.6.1 QUANTUM MECHANICS

The discretization of the scalar field theory on a space-time lattice has some elegant features which we present briefly in this section; for fermions, see Ref. [20]. For simplicity we start with a simple quantum mechanical system of unit mass, with action

$$S = a_0\sum_t\left\{\frac{[q(t+a_0)-q(t)]^2}{2a_0^2} - V[q(t)]\right\}, \tag{2.62}$$

where a_0 is the time step, $t = a_0 r$, with integer r. We define the quantum system by means of the path integral. The discretized path integral

$$Z = \int\Big[\prod_t dq(t)\Big]e^{iS} \tag{2.63}$$

corresponds to an evolution operator in Hilbert space that is a product of single step evolution operators given by

$$\hat U = \hat U_p\hat U_q, \tag{2.64}$$

with

$$\hat{U}_p = e^{-ia_0\hat{p}^2/2}, \qquad \hat{U}_q = e^{-ia_0 V(\hat{q})}, \tag{2.65}$$

where $\hat{p}$ and $\hat{q}$ are canonical operators satisfying $[\hat{q},\hat{p}] = i$. A finite time-evolution then takes the "Trotter form"

$$\hat{U}_q\hat{U}^r = \hat{U}_q \ldots \hat{U}_p\hat{U}_q\hat{U}_p\hat{U}_q\hat{U}_p\hat{U}_q \ldots \hat{U}_q, \tag{2.66}$$

The Heisenberg operators

$$\hat{p}(t) = \hat{U}^{r\dagger}\hat{p}\,\hat{U}^r, \qquad \hat{q}(t) = \hat{U}^{r\dagger}\hat{q}\,\hat{U}^r, \qquad t = a_0 r, \tag{2.67}$$

satisfy the discretized equations of motion in leapfrog fashion,

$$\hat{p}(t+a_0) = \hat{p}(t) - a_0 V'(\hat{q}(t)), \tag{2.68a}$$

$$\hat{q}(t+a_0) = \hat{q}(t) + a_0\hat{p}(t+a_0). \tag{2.68b}$$

With $\hat{q}(t) \to q(t)$, $\hat{p}(t) \to (q(t)-q(t-a_0))/a_0$, the above equations (2.68) are identical in form to the classical equations obtained from the stationary action principle.

Making a unitary transformation

$$\hat{T} = e^{-ia_0 V(\hat{q})/2}\,\hat{U}e^{ia_0 V(\hat{q})/2}, \tag{2.69}$$

we get an equivalent operator $\hat{T}$, that becomes the Hermitian and positive transfer operator upon analytically continuing to imaginary time (see e.g. Ref. [49]), writing $a_0 = e^{-i\theta}|a_0|$, $\theta = 0 \to \pi/2$,

$$\hat{T} \to e^{-|a_0|V(\hat{q})/2}\,e^{-|a_0|\hat{p}^2/2}\,e^{-|a_0|V(\hat{q})/2}. \tag{2.70}$$

Specialising to the harmonic case $V(q) = \omega^2 q^2/2$ we can diagonalize the time evolution in terms of creation and annihilation operators $\hat{c}^\dagger$ and $\hat{c}$,

$$\hat{T}\hat{c}\hat{T}^\dagger = e^{ia_0\omega^{(e)}}\,\hat{c}, \qquad \hat{T}\hat{c}^\dagger\hat{T}^\dagger = e^{-ia_0\omega^{(e)}}\,\hat{c}^\dagger, \tag{2.71}$$

with

$$\hat{c} = \frac{1}{\sqrt{2\omega^{(n)}}}(\omega^{(n)}\hat{q} + i\hat{p}), \tag{2.72}$$

and

$$\cos(a_0\omega^{(e)}) = 1 - \frac{1}{2}a_0^2\omega^2, \tag{2.73a}$$

$$\omega^{(n)} = \frac{1}{a_0}\sin(a_0\omega^{(e)}) = \omega\sqrt{1-\frac{1}{4}a_0^2\omega^2}, \tag{2.73b}$$

and the conjugate relation for $\hat{c}^\dagger$. The creation and annihilation operators satisfy the standard commutation relation $[\hat{c}, \hat{c}^\dagger] = 1$. The superscripts e and n distinguish the "exponent omega" (eigenvalue omega) $\omega^{(e)}$ from the "normalisation omega" (eigenvector omega) $\omega^{(n)}$, and both go over to the "original omega" ω in the continuous time limit $a_0 \to 0$. The ground state is given by

$$\hat{c}|0\rangle = 0, \qquad \langle q|0\rangle = \nu e^{-\omega^{(n)} q^2/2}, \tag{2.74}$$

with ν a normalisation constant and

$$\hat{T}(\hat{c}^\dagger)^n|0\rangle = e^{-i(n+1/2)a_0\omega^{(e)}}(\hat{c}^\dagger)^n|0\rangle. \tag{2.75}$$

The evolution becomes unstable when $a_0^2\omega^2 > 4$, for which $\omega_k^{(e)}$ is imaginary. The eigenvalues of $\hat{T}$ are then no longer phase factors and its eigenfunctions no longer normalisable, despite its formally unitary form. This is of course avoided by taking a_0 sufficiently small. The discretization errors in $\omega^{(e)}$ and $\omega^{(n)}$ are of order a_0^2.

It is natural to identify the Hamiltonian $\hat{H}$ from $\hat{T} = \exp(-ia_0\hat{H})$, but this leaves a modulo $2\pi/a_0$ ambiguity for the eigenvalues of $\hat{H}$ (the imaginary time version is unambiguous). To pin down $\hat{H}$ more precisely we can use the Baker-Campbell-Hausdorff series for combining the exponents in $\hat{T}$, which gives $\hat{H} = \hat{p}^2/2 + V(\hat{q}) + \mathcal{O}(a_0^2)$. We shall neglect the corrections of order a_0^2. The exact $\hat{H}$ is time-independent. In practise, the expectation value of the approximate $\hat{H}$ is constant in time up to small fluctuations, as expected for a leapfrog algorithm.

2.6.2 FIELD THEORY: HARTREE APPROXIMATION

For the application to the Hartree approximation it will be more convenient for us to work with the unitarily-related creation and annihilation operators that diagonalize the operator $\hat{U}$,

$$\begin{aligned}\hat{a} &= e^{ia_0V(\hat{q})/2}\,\hat{c}\,e^{-ia_0V(\hat{q})/2} \\ &= \frac{1}{\sqrt{2\omega^{(n)}}}\left(\frac{1-e^{-ia_0\omega^{(e)}}}{ia_0}\hat{q} + i\hat{p}\right),\end{aligned} \tag{2.76a}$$

$$\hat{U}\hat{a}\hat{U}^\dagger = e^{ia_0\omega^{(e)}}\,\hat{a}, \tag{2.76b}$$

for $V = \omega^2 q^2/2$. Note that $\hat{a} \to \hat{c}$ in the limit $a_0 \to 0$.

The generalisation of the above quantum mechanical model to our scalar field is straightforward. The lattice action on a space-time lattice with spatial/temporal

lattice distance a/a_0 is given by

$$S[\varphi] = a_0 a \sum_{x,t} \left\{ \frac{[\varphi(x,t+a_0)-\varphi(t,x)]^2}{2a_0^2} - \frac{[\varphi(x+a,t)-\varphi(t,x)]^2}{2a^2} - \frac{1}{2}\mu^2\varphi(t,x)^2 - \frac{1}{4}\lambda\varphi(t,x)^4 \right\}, \tag{2.77}$$

where we assume a periodic physical size $L = Na$. The operator description in Hilbert space follows from the lattice regularised path integral. In the Hartree approximation we write the operator fields in terms of a complete set of mode functions,

$$\hat{\varphi}(t,x) = \varphi(t,x) + \sum_k [\hat{b}_k f_k(t,x) + \hat{b}_k^\dagger f_k(t,x)^*], \tag{2.78a}$$

$$\hat{\pi}(t,x) = \pi(t,x) + \sum_k [\hat{b}_k \dot{f}_k(t,x) + \hat{b}_k^\dagger \dot{f}_k(t,x)^*], \tag{2.78b}$$

where the use of

$$\dot{f}(t,x) = \frac{f(t,x) - f(x,t-a_0)}{a_0}, \tag{2.79}$$

is inspired by equation (2.68b) (using instead the forward derivative $\dot{f}_k(t,x) = [f(x,t+a_0)-f(t,x)]/a_0$ gives equivalent results). Imposing canonical commutation relations for both $\hat{\varphi}$, $\hat{\pi}$ and $\hat{b}_k$, $\hat{b}_k^\dagger$, leads to the orthonormality and completeness relations

$$a\sum_x [i\dot{f}_k(t,x) f_l^*(t,x) - i f_k(t,x)\dot{f}_l^*(t,x)] = \delta_{kl}, \tag{2.80a}$$

$$\sum_k [i f_k^*(t,x)\dot{f}_k(y,t) - i f_k(t,x)\dot{f}_k^*(y,t)] = \frac{\delta_{xy}}{a}. \tag{2.80b}$$

The time-independence of the orthonormality conditions corresponds to Noether charges of symmetries of the effective action on the lattice, as explained in Section 2.2. We use the static solutions of the Hartree equations in constructing the set of mode functions. Their equation of motion

$$\frac{f_k(x,t+a_0) - 2f_k(t,x) + f_k(x,t-a_0)}{a_0^2} = \frac{f_k(x+a,t) - 2f_k(t,x) + f_k(x-a,t)}{a^2} - m^2 f_k(t,x), \tag{2.81}$$

can be written in the leapfrog form (2.68). The solution of the recursion relation (2.81) can be written as

$$f_k(t,x) = \frac{e^{ikx - i\omega_k^{(e)} t}}{\sqrt{2\omega_k^{(n)} L}}, \qquad k = \frac{2\pi j}{L}, \qquad j = -\frac{N}{2}+1, \ldots, \frac{N}{2}, \tag{2.82}$$

giving

$$-\frac{2-2\cos(\omega_k^{(e)} a_0)}{a_0^2} + \frac{2-2\cos(ka)}{a^2} + m^2 = 0. \tag{2.83}$$

Defining a lattice $\omega_k^{(a)}$ as

$$\omega_k^{(a)} = \sqrt{m^2 + \frac{2-2\cos(ka)}{a^2}}, \tag{2.84}$$

we find the analogue of (2.73a),

$$\cos(a_0 \omega_k^{(e)}) = 1 - \frac{1}{2} a_0^2 (\omega_k^{(a)})^2, \tag{2.85}$$

which has real $\omega_k^{(e)}$ solutions for $a/a_0 \geq \sqrt{4 + a^2 m^2}$. In simulations we used $a/a_0 \geq 10$, which amply secured the stability. The normalisation in (2.82) is fixed by the orthonormality relation (2.80a), which gives the analogue of (2.73b)

$$\omega_k^{(n)} = \frac{\sin(a_0 \omega_k^{(e)})}{a_0} = \omega_k^{(a)} \sqrt{1 - \frac{1}{4} a_0^2 (\omega_k^{(a)})^2}, \tag{2.86}$$

The completeness relation (2.80b) is then also satisfied. When the mode functions have the form (2.82), the $\hat{a}_k$ defined by

$$\hat{\varphi} = \sum_k \hat{a}_k f_k + \text{h.c.}, \qquad \hat{\pi} = \sum_k \hat{a}_k \dot{f}_k + \text{h.c.}, \tag{2.87}$$

are related to $\hat{\varphi}$ and $\hat{\pi}$ as in the quantum mechanical case (2.76a). Note that $\omega_k^{(n)}$, $\omega_k^{(e)} \to \omega_k^{(a)}$ in the limit $a_0 \to 0$, and $\omega_k^{(a)} \to \sqrt{m^2 + k^2}$ as $a \to 0$.

2.6.3 PARTICLE NUMBER

We end this section with a properly discretized version of the instantaneous particle number n_k, using the stationary solution (2.82) and the two-point functions (2.49). Suppose the mean field is zero and

$$\langle \hat{b}_k^\dagger \hat{b}_k \rangle = n_k^0 = n_{-k}^0. \tag{2.88}$$

Then

$$S_k(t) = \left(n_k^0 + \frac{1}{2}\right) \frac{1}{\omega_k^{(n)}} \tag{2.89a}$$

$$U_k(t) = \left(n_k^0 + \frac{1}{2}\right) \frac{(\omega_k^{(a)})^2}{\omega_k^{(n)}}, \tag{2.89b}$$

where we used

$$\dot{f}_k(t,x)\dot{f}_k^*(y,t) = (\omega_k^{(a)})^2 f_k(t,x) f_k^*(y,t). \tag{2.90}$$

Inverting (2.89) we find that our definition of the instantaneous particle energy $\omega_k(t)$ does not need discretization corrections,

$$\omega_k^{(a)} = \sqrt{\frac{U_k(t)}{S_k(t)}} \equiv \omega_k(t). \tag{2.91}$$

On the other hand, compared to (2.57) the definition of instantaneous particle number needs important corrections for large ω_k:

$$n_k^0 + \frac{1}{2} = \sqrt{U_k S_k}\frac{\omega_k^{(n)}}{\omega_k^{(a)}} = \sqrt{U_k(S_k - \frac{1}{4}a_0^2 U_k)} \equiv n_k(t) + \frac{1}{2}, \tag{2.92}$$

using (2.86) and (2.91).

For larger energies the corrections can become quite important. Denoting the uncorrected particle number by $\tilde{n}_k = \sqrt{U_k S_k} - 1/2$, we find

$$\begin{aligned} \frac{\tilde{n}_k - n_k}{n_k} &= \frac{n_k + \frac{1}{2}}{n_k}\Big(\frac{1}{\sqrt{1 - \frac{1}{4}(a_0\omega_k^{(a)})^2}} - 1\Big) \\ &\approx \frac{n_k + \frac{1}{2}}{n_k}\frac{1}{8}(a_0\omega_k^{(a)})^2. \end{aligned} \tag{2.93}$$

Using a Bose-Einstein distribution at $T = m$ and the typical value $a_0 m = 1/80$ we find that the relative difference becomes unity for $\omega_k/m = 7.5$. At the lower temperature $T/m = 0.5$ this is the case already for $\omega_k/m = 4.3$.

2.7 NUMERICAL RESULTS

2.7.1 MONTE CARLO CHECK

In this section we will first check the expectation, that for weakly coupled fields the equilibrium particle densities, defined according to (2.56), indeed have a Bose-Einstein distribution, while the energies will have a free quasi-particle dispersion

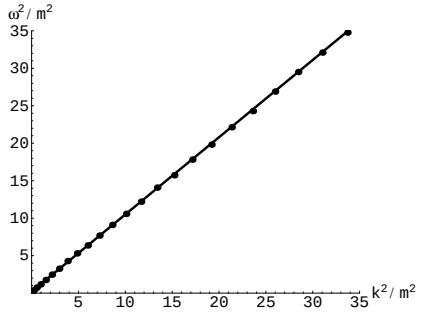

a: Large momenta

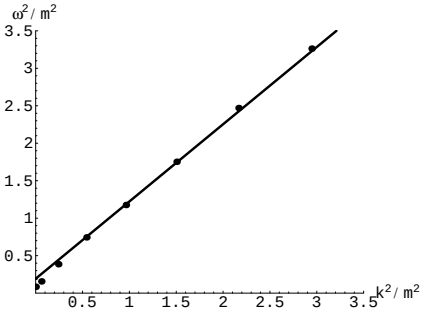

b: Small momenta: deviations from linear behaviour are visible.

Figure 2.4: Dispersion relation computed from a Monte Carlo simulation of the Euclidean time version of the model. The model parameters are: $\lambda/m^2 = 1/2v^2 = 1/4$, $Lm = 25.6$, $1/am = 10$ and $T/m = 1$, with 20 steps in the Euclidean time direction. Here k is the lattice momentum $\sqrt{2-2\cos(ak)}/a$. The statistical error bars are smaller than the symbols.

relation, approximately,

$$n_k = \frac{1}{e^{\omega_k/T}-1}, \qquad \omega_k^2 = m(T)^2 + \frac{2-2\cos(ak)}{a^2}. \tag{2.94}$$

The effective mass $m(T)$ of the quasi-particles is temperature dependent. In the following we shall use the zero temperature mass $m \equiv m(T=0)$ to scale dimensionful quantities.

To substantiate this expectation (2.94), we have performed several Monte Carlo simulations of the Euclidean time version of our model at parameter values in the same range as we will use for the Hartree simulations. In Fig. 2.4 we show the dispersion relation computed from such a Monte Carlo simulation. We chose a temperature $T/m = 1$ and measured S_{xy}. We stress that such a Monte Carlo simulation gives the *exact* (up to statistical errors) results for the finite temperature Green function. Making the assumption that n_k has the BE form, we computed the ω_k from S_{xy} using (2.56). As can be seen from the figure, the free form (2.94) for the quasi-particle dispersion relation holds very well, with $m(T)/m \approx 0.43$. This value is close to that found with the effective potential calculations in the Hartree approximation, as described in Section 2.3, which gives $m(T)/m \approx 0.41$ at $T/m = 1$. The

effects of the temperature and interactions show up almost exclusively in the value of the effective mass $m(T)$.

2.7.2 HARTREE ENSEMBLE APPROXIMATION: INITIAL CONDITIONS

We will now describe some Hartree simulations we used for obtaining the particle numbers $n_k(t)$. The mass and coupling parameters were chosen such that the system at zero temperature is in the "broken symmetry phase". The coupling was weak, $\nu^2 = m^2/2\lambda = 6$. Here and in the following m is the mass of the particles at zero temperature.

The system is discretized on a space-time lattice with spatial (temporal) lattice distance a (a_0), with $a_0/a = 0.1$. The number of spatial lattice sites, equal to the number of independent complex mode functions, will be denoted with $N = L/a$. The discretized Lagrangian gives rise to second order difference equations, with a time evolution which is equivalent to a first order leapfrog algorithm for $\pi_x(t) \equiv [\varphi_x(t + a_0) - \varphi_x(t)]/a_0$ and $\varphi_x(t)$.

The initialisation is similar to that used in [16, 17],

$$\varphi_x^{(i)} = \nu, \qquad \pi_x^{(i)} = Am \sum_{j=1}^{j_{max}} \cos(2\pi jx/L - \psi_j^{(i)}), \tag{2.95}$$

with random phases ψ_j uniformly distributed in $[0, 2\pi)$. The modes are initialised with the equilibrium form at zero temperature: the n_k^0 are all zero and the modes $f_k(x, 0)$, $\dot{f}_k(x, 0)$ are given by the plane waves (2.82) and their time derivative at $t = 0$, together with the definitions (2.85) and (2.86). The density operator is thus a superposition of coherent pure states as in (1.5).

2.7.3 TOWARDS EQUILIBRIUM

We first describe a simulation for which $\lambda/m^2 = 1/12$, $N = 256$, $mL = 32$, $j_{max} = 4$, $A = 1/\sqrt{2}$, such that the energy density is given by $E/Lm^2 = A^2 j_{max}/4 = 0.5$. A Bose-Einstein distribution describing particles with such an energy density would have a temperature $T/m \approx 1.08$, well below the phase transition at $T/m \approx 1.8$, as calculated from the finite temperature effective potential. We also chose these parameters so that the system may end up in a low temperature quantum regime and not in a classical regime with $T/m \gg 1$. A boring consequence is that the volume averaged mean field typically just oscillates around one of the two minima, we did not encounter an initial condition for which it crossed the barrier after $tm > 50$.

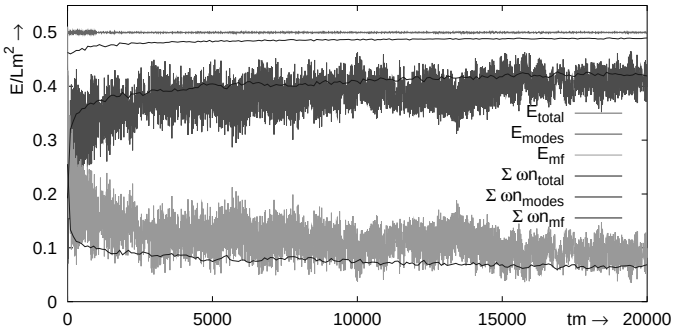

Figure 2.5: The total energy density E/Lm^2 (horizontal line at 0.5), energy density of the mean field (lower band) and of the modes (higher band). Also plotted are the various energy densities in the quasi-particle interpretation, $\sum_k n_k \omega_k / Lm^2$.

Initially the mean field carries all the energy in its low momentum modes $0 < k/m \leq \pi/4$ (zero momentum mode excluded). Due to interaction with the inhomogeneous mean field, the modes will not keep the vacuum form, but get excited. Fig. 2.5 shows the time dependence of the energy density for one of the members of the ensemble. The total energy is conserved up to a numerical accuracy of about 0.2%. The energy in the mean field (cf. (2.44) for its definition), initially equal to the total energy, is decreasing rapidly and after a time $tm \approx 100$ about 50% has been transferred to the modes. The mean field continues losing energy after that time but at a time tm of the order 20 000 some 15% is still left.

The development of the particle numbers $n_k(t)$ at early times is shown in Fig. 2.6a, including the mean field contribution, cf. (2.50a)–(2.50c).[3] Initially the mean field gives the main contribution since $n_k^0 = 0$ for the modes, but then the mode contribution rapidly takes over. Because the mean field contribution fluctuates strongly we used as many as 500 initial conditions for these early times, without coarsening over time. Fig. 2.6b shows the mode contribution to n_k as a function of ω (40 initial conditions were used for the data at $tm > 200$, with no coarsening over time). It starts out identically zero, rises rapidly and then appears to stabilise. The figure also shows a fit to the Bose-Einstein distribution with chemical potential μ at time $tm = 990$. A chemical potential is expected to develop temporarily at weak coupling, since elastic scattering dominates over processes like $2 \leftrightarrow 4$ scattering. The fitted temperature ($\beta m = 1.08$) is already approaching the earlier estimate

[3] In this and following figures an average is taken over $k = \pm|k|$. The distributions n_k for positive and negative k are equal within fluctuations.

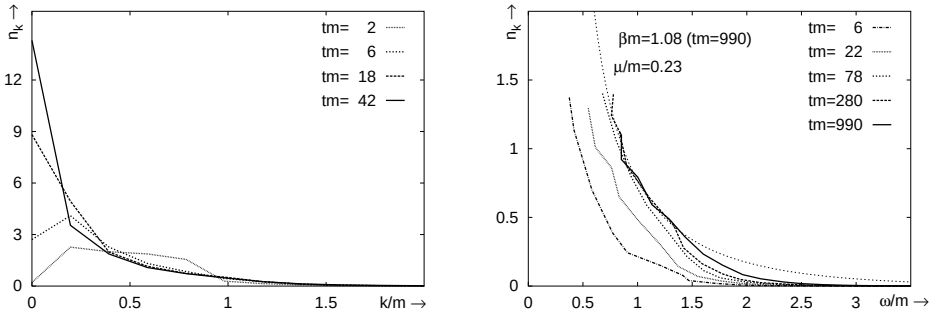

a: n_k versus k/m b: n_k (modes only) versus ω_k

Figure 2.6: Particle number n_k for early times, time increases from bottom to top.

$T/m \approx 1.1$ based on the energy density. The complete distribution function (including the mean field contribution) reaches much larger values at these early times (by a factor $3-4$) and the curves appear closer together. However the plots are noisier, due to the strongly fluctuating mean field.

To study the tail of the distribution more easily, a plot of $\log(1+1/n)$ is shown in Fig. 2.7a. This function is linear in ω for a Bose-Einstein distribution with slope equal to the inverse temperature β and offset equal to the $\beta\mu$. We indeed see linear Bose-Einstein behaviour developing at low momenta with gradual participation of the higher momentum modes. Including the contribution of the mean field, shown in Fig. 2.7b, a more rapid convergence and higher occupation numbers can be seen, giving a higher fitted temperature and smaller chemical potential, compared to the data in Fig. 2.7a. The trend seen in Figs. 2.7a and 2.7b continues at larger times, as shown in Fig. 2.8 for the contribution of the modes only. A plot where the mean field contribution is included looks similar. For this simulation an average is taken over a time interval $tm = 24$, approximately 3.5 oscillation periods, and only 10 initial configurations. The straight line is a Bose-Einstein fit with zero chemical potential at $tm = 6200$ in the region $\omega/m < 1.8$. We see that the slope is roughly constant in time and that the thermalized part of the distribution is extending to higher values of ω, roughly linear in $\log tm$.

In Fig. 2.9a a plot is made of the Bose-Einstein temperatures from the fits (modes only) as a function of time. For times $tm < 3000$ the fit is made over the interval $\omega/m < 1.4$ while for later times this is increased to $\omega/m < 1.8$. The figure shows an anti-correlation between T and μ which would be meaningful, i.e. not just a fitting artifact, if the particle density $n = \sum_k n_k/L$ is constant, or has evidently smaller fluctuations. This seems to be the case indeed: as shown in Fig. 2.9b, the density n

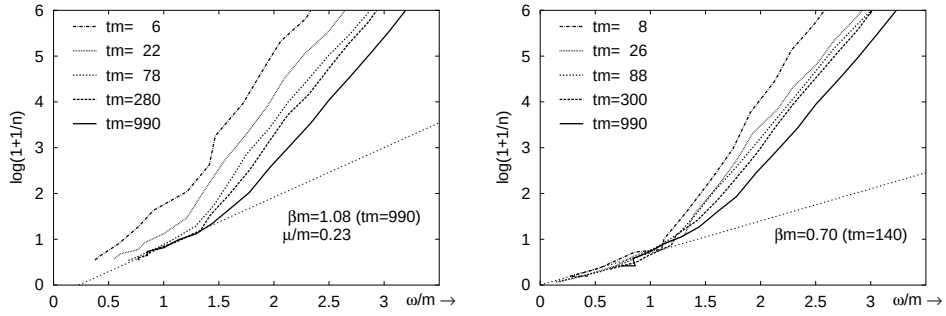

a: Modes only

b: Mean field and modes

Figure 2.7: Particle number $\log(1 + 1/n_k)$ versus ω_k for early times. The straight line is a Bose-Einstein fit for the latest time, over $\omega/m < 1.2$.

corresponding to the modes only is quite constant for times $tm > 100$, and in fact continues to remain so up to times of over 5000. On a larger time scale of order 10000 or so it drops somewhat. The initial approach of n/m (modes only) to the value ≈ 0.34 can be fitted to an exponential, which yields an equilibration time scale $\tau m = 15 - 20$, depending on the fitting range.

We have to be careful, however, that our μ is not an artifact of the fitting procedure. We believe this to be the case for the larger times $tm \gtrsim 40000$ where μ becomes negative. As can be seen (with difficulty) in Fig. 2.8, the distribution starts to deviate at low ω upwards from the straight line, corresponding to a suppression of n_k compared to the Bose-Einstein form. We interpret this as a contamination by classical behaviour $n_k \approx T_{cl}/\omega_k$, cf. (2.48), as will be argued later in this section.

Let us now make a comparison with analytical results derived from the equilibrium finite temperature effective potential (2.45). Around time $tm = 15000 \ldots 20000$ the temperature measured in the simulation is $T/m = 1.1$. The effective potential then gives for the thermal mass $m(T = 1.1)/m = \nu(T = 1.1)/\nu = 0.93$. We derive the thermal mass in the simulation from the dispersion relation of measured ω_k. It is in very good agreement with a free form: $\omega_k^2 = m^2(T) + k^2$. A straight line fit of ω^2 versus k^2 over the interval $tm = 15000 \ldots 20000$ gives a slope 1.00 and an offset $m(T = 1.1)/m = 0.908$. This is also in good agreement with the volume averaged value of the mean field, which is 0.91. These values are somewhat lower than the position of the minimum in the effective potential because of its asymmetric shape. However the difference is small because of the small amplitude of the mean field oscillations around this minimum.

The quasi-particle aspect can be investigated further by looking at the energy

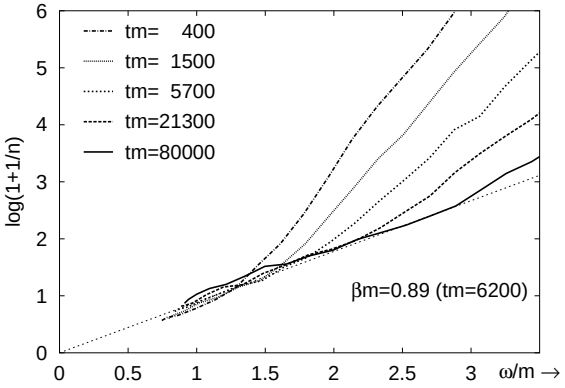

Figure 2.8: The particle numbers (modes only) at later times.

$\sum_k n_k \omega_k$, as plotted in Fig. 2.5. We have made a distinction between the particle number as derived from the mean field, quantum and total two-point function. We see that the total energy in the particles (mean field + modes) is only a few percent lower than the total energy is the system, as may be expected for a weakly coupled system. It is also interesting to note that, while the quantum modes initially carry only a small fraction of the total energy, they thermalize with the same temperature $1.1m$ the system would have if all energy would be distributed according to a Bose-Einstein distribution with zero chemical potential.

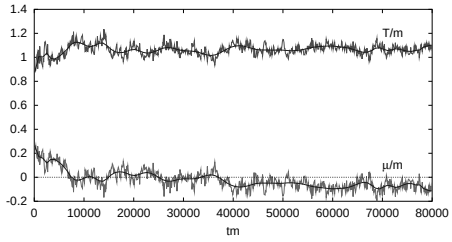

a: Bose-Einstein temperature. The smoother lines are drawn to guide the eye.

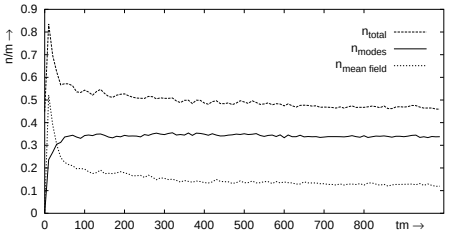

b: Particle densities $n/m = \sum_k n_k/Lm$

Figure 2.9: Bose-Einstein temperature and particle densities $n/m = \sum_k n_k/Lm$.

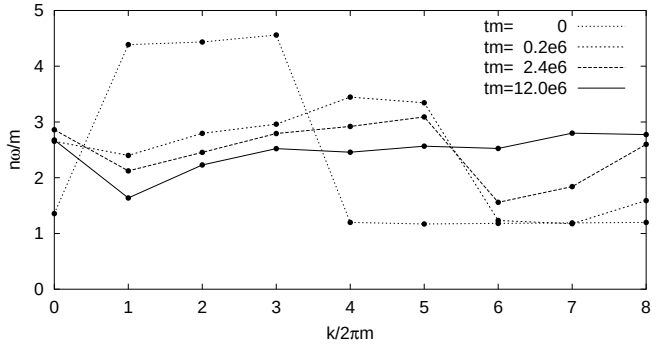

Figure 2.10: Energy distribution $n_k\omega_k/m$ (modes + mean field) for a small system with $N = 16, Lm = 1, E/Lm^2 = 36$.

2.7.4 LATE TIME BEHAVIOUR

We now turn to the very long time behaviour of the system, where we expect Bose-Einstein behaviour to be replaced by classical equipartition according to the effective Hamiltonian (2.22). The numerical computation of the equilibrium distribution functions in this regime is very difficult as it changes exceedingly slowly (cf. the slow log t-like population of the high momentum modes in Fig. 2.8). We therefore have carried out simulations in a smaller system at stronger coupling and at larger energy densities in order to make time scales a lot shorter. Here we present data for $N = 16$, $Lm = 1$, $\lambda/m^2 = 1$ and $E/Lm^2 = 36$, for which the system is in the "symmetric phase". In Fig. 2.10 we plotted $n_k\omega_k$ (modes + mean field) versus the integer $kL/2\pi = k/2\pi m$, for different times. Note that it was necessary to initially also excite the highest momentum modes, otherwise the system would not reach final equilibrium sufficiently closely even after a time of $12 \cdot 10^6$. Classical equipartition suggests $n_k\omega_k = T_{cl}$, giving a straight horizontal line in the plot. We see indeed flat behaviour, with lower momentum modes tending to have somewhat smaller occupation numbers, except for the zero mode. Runs at small coupling $\lambda/m^2 = 1/12$ in larger volumes $Lm = 4$ and $Lm = 16$ in the "broken phase" showed similar results, except that the zero modes were less exceptional.

So we do find approximate classical $n_k = T_{cl}/\omega_k$ behaviour at very large times. Classical equipartition leads to small temperatures $T_{cl} = O(1/N)$. If this behaviour sets in first for the low momentum modes, then these will appear to be underoccupied compared to the Bose-Einstein distribution at temperature $T > T_{cl}$. This is indeed the trend noticed earlier in Fig. 2.8, where the low momentum data at times

$tm > 20000$ lie above the straight line going through the data at larger momenta.

2.8 DISCUSSION

In this chapter we introduced the Hartree approximation and explained how its thermalization properties can be improved, by extending it with an initial ensemble average, thus allowing for the simulation of systems which are non-Gaussian.

We presented results of simulations mainly for a weakly coupled system in the broken symmetry phase. For such a weakly coupled system a near equilibrium description in terms of quasi-particles is expected to be reasonable, which we checked and confirmed in a Monte Carlo simulation.

Starting with distributions which are initially far out of equilibrium, in which only low momentum modes $k \lesssim m$ of the classical field were excited with low energy density, we observed approximate thermalization with a particle distribution function approaching the Bose-Einstein form. After a fairly rapid initial thermalization at low momenta, the gradual adjustment of progressively higher momentum modes is very slow. The energy in the mean field gets transferred to the two-point function and one might think that the system behaves as if the mean field were constant. However, this is not the case: up to large times $tm = 80000$ the mean field keeps fluctuating in space and time and carries a non-negligible fraction of the total energy.

It is hard to assign a time scale for the gradual adjustment of the distribution at higher momenta, however it appears to be at least two orders of magnitude larger than the equilibration time $\tau m \approx 20$ for the particle density, found at early times ($tm = O(10)$). Slow thermalization was also found in a recent study of the fully nonlinear classical system in the symmetric phase [18]. Using our parameter combination $\lambda T/m^3 \approx 1.1/12$ in their empirical fit $1/\tau m = 5.8\,10^{-6}\,(6\lambda T/m^3)^{1.39}$ would give $\tau m \approx 4\,10^5$.

On a large time scale, perhaps of the order of $tm = 10000$ or more, the distribution moves away from the quantum (Bose-Einstein) form towards classical equipartition. We never reached this classical equipartition for the weak coupling and low temperature used in this study, because of the very long computer time this would take. Only the use of very small systems, at high energy density and/or coupling enabled us to reach a situation resembling classical equipartition.

We have carried out many more simulations at higher energy densities, and larger couplings, in which the approximate quantum nature of the distribution at intermediate times was also evident. With higher energy density and/or larger coupling the effective coupling strength $n_k\lambda/m^2$ increases. Things then go quicker and the time scales of quantum versus classical equilibration get closer and might even get blurred. Furthermore, the Bose-Einstein distribution, on which we based

our analysis, might get distorted by non-perturbative effects. We may have seen such effects already in a significant enhancement of n_k at low momenta, in simulations at larger volume.

Summarising, on the one hand our intuitive expectation that there may be quantal thermalization in the Gaussian approximation, due to scattering of the mode particles via the arbitrary inhomogeneous mean field, appears to be validated, but on the other hand it is not clear how useful this approximation can be for equilibrium physics, e.g. at finite density. It is possible that starting closer to quantum thermal equilibrium the time to reach thermalization is reduced and the intermediate time regime of quantal equilibrium can be stretched to do useful computations. Then it will be interesting to compare the Gaussian approximation with the classical approximation and see which one fares best. We will address these aspects in the next chapter. In that chapter we will also investigate the possibility of using fewer mode functions, in order to safe on the numerical cost of the inhomogeneous Gaussian approximation, which is substantial: for an N^d spatial lattice, the computational time scales like N^{2d+1}.

2.A DIAGONAL COHERENT STATE REPRESENTATION

To derive the representation (1.5) consider first a quantum mechanical system of two degrees of freedom with canonical variables p and q. Let $|pq\rangle$ be a normalised coherent state, such that

$$\hat{a}|pq\rangle = \frac{1}{\sqrt{2\omega}}\,(\omega q + ip)\,|pq\rangle, \qquad \hat{a} \equiv \frac{1}{\sqrt{2\omega}}\,(\omega\hat{q} + i\hat{p}), \tag{2.96a}$$

$$\langle p'q'|pq\rangle = \exp\Big\{\frac{i}{2}\,(pq' - p'q) - \frac{1}{4\omega}[\omega^2(q-q')^2 + (p-p')^2]\Big\} \tag{2.96b}$$

$$\int \frac{dp\,dq}{2\pi}\,|pq\rangle\langle pq| = \hat{1}. \tag{2.96c}$$

where $\omega > 0$ is arbitrary. As is well known, the coherent states form a (over) complete set, so it should be possible to represent an arbitrary operator $\hat{\rho}$ in the form

$$\hat{\rho} = \int \frac{dp\,dq}{2\pi}\,\rho(p,q)\,|pq\rangle\langle pq|. \tag{2.97}$$

In our application $\hat{\rho}$ is a density operator, for which

$$\int \frac{dp\,dq}{2\pi}\,\rho(p,q) = 1. \tag{2.98}$$

Taking matrix elements of the above equation with $|p', q'\rangle$ and $\langle -p', -q'|$ gives

$$e^{(\omega^2 q'^2 + p'^2)/2\omega} \langle -p', -q'|\hat{\rho}|p', q'\rangle = \int \frac{dp\, dq}{2\pi} e^{i(p'q - pq')} e^{-(\omega^2 q^2 + p^2)/2\omega} \rho(p, q), \quad (2.99)$$

from which follows that the function $\rho(p, q)$ is given by the inverse Fourier transform

$$\rho(p, q) = e^{(\omega^2 q^2 + p^2)/2\omega} \int \frac{dp'\, dq'}{2\pi} e^{-i(p'q - pq')} e^{(\omega^2 q'^2 + p'^2)/2\omega} \langle -p', -q'|\hat{\rho}|p', q'\rangle. \quad (2.100)$$

A trivial example is a coherent state centred about (p_1, q_1), for which $\rho(p, q) = 2\pi\delta(p - p_1)\delta(q - q_1)$. Another simple example is given by the thermal density operator of the harmonic oscillator with Hamiltonian $H = (\omega^2 q^2 + p^2)/2$,

$$\hat{\rho} = \frac{1}{Z} \exp\left[-\beta\omega\left(\hat{a}^\dagger \hat{a} + \frac{1}{2}\right)\right], \quad (2.101)$$

with Z the partition function, such that $\mathrm{Tr}\,\hat{\rho} = 1$. Choosing the ω in the definition of the coherent states equal to the ω appearing in this $\hat{\rho}$, it follows that

$$\langle -p', -q'|\hat{\rho}|p', q'\rangle = \frac{1}{Z} \exp\left[-\left(e^{-\beta\omega} + 1\right)\frac{1}{2\omega}\left(\omega^2 q'^2 + p'^2\right) - \frac{1}{2}\beta\omega\right], \quad (2.102)$$

and

$$\rho(p, q) = \frac{1}{Z} \exp\left[-\left(e^{\beta\omega} - 1\right)\frac{1}{2\omega}\left(\omega^2 q^2 + p^2\right) + \frac{1}{2}\beta\omega\right]. \quad (2.103)$$

We recognise the inverse Bose-Einstein distribution, $\exp(\beta\omega) - 1$, in the exponent. For large temperatures, $\beta\omega \ll 1$, $\rho(p, q)$ approaches the classical Boltzmann distribution $\exp(-\beta H)$. In the limit of zero temperature we get the distribution representing the ground state,

$$\rho(p, q) = 2\pi\delta(p)\delta(q). \quad (2.104)$$

More examples can be found in Ref. [39, 40]. The generalisation to the scalar field is straightforward.

2.B EQUIPARTITION?

The effective Hamiltonian $H_{\mathrm{eff}}[\varphi, \pi, \xi, \eta]$ of the Gaussian approximation is conserved in time. So one may expect that after very large times the system reaches

classical equilibrium. Assuming ergodicity, time averages will then correspond to the Boltzmann distribution $\exp(-H_{\text{eff}}/T)$, under the constraints of the conserved generalised angular momenta $L_{\alpha a,\beta b}$, cf. (2.27). We shall now derive an approximate form for the particle distribution function n_k, corresponding to this classical equilibration.

In our derivation we assume the system to be weakly coupled, such that we may approximate H_{eff} in the Boltzmann distribution by a free field form (possibly after having shifted φ by its equilibrium value v such that $\langle\varphi\rangle = 0$),

$$H_{\text{free}} = \int dx \left[\frac{1}{2}\pi^2 + \frac{1}{2}(\partial\varphi)^2 + \frac{1}{2}m^2\varphi^2 + \sum_\alpha (|\eta_\alpha|^2 + |\partial\xi_\alpha|^2 + m^2|\xi_\alpha|^2)\right], \quad (2.105)$$

where m is an effective mass. For convenience we use a complex formalism for the mode functions, $\xi_\alpha = (\xi_{\alpha 1} - i\xi_{\alpha 2})/\sqrt{2} = \sqrt{n^0_\alpha + 1/2}\, f_\alpha$, cf. (2.21).[4] The generalised angular momenta are just the naturally conserved charges of the complex fields,

$$Q_\alpha = i\int dx\, (\xi^*_\alpha \eta^*_\alpha - \eta_\alpha \xi_\alpha) = L_{\alpha 1,\alpha 2} = n^0_\alpha + \frac{1}{2}. \quad (2.106)$$

We take them into account by introducing chemical potentials μ_α, such that the average charges are equal to their values set by the initial conditions, $Q_\alpha = n^0_\alpha + 1/2$. It is not immediately clear that this procedure is correct, because these initial values are not extensive and therefore relative fluctuations will be large, but the emerging formulae below look reasonable. Imposing the constraints exactly appears to be quite cumbersome, except for $N = 1$. Recall that N is the number of complex mode functions, which in the lattice regularisation is equal to the number of lattice sites: $N = \sum_k = \sum_\alpha$. Here we shall assume a sharp momentum cutoff $|k| < \Lambda$, for simplicity.

The classical grand canonical average will be indicated by an over-bar:

$$\overline{F} = \frac{1}{Z_c}\int [d\varphi\, d\pi][\prod_\alpha d\xi_\alpha\, d\eta_\alpha]\, \exp\Big[-\frac{1}{T}\Big(H_{\text{free}} - \sum_\alpha \mu_\alpha Q_\alpha\Big)\Big]\, F, \quad (2.107)$$

with Z_c the partition function such that $\overline{1} = 1$. Our approximation for n_k is now given by ($\omega_k = \sqrt{m^2 + k^2}$)

$$\begin{aligned} S(x,y) &= \frac{1}{L}\sum_k e^{ik(x-y)}\, \frac{n_k + 1/2}{\omega_k}, \\ &= \overline{\varphi(x)\varphi(y)} + \sum_\alpha \Big[\frac{n^0_\alpha + 1}{n^0_\alpha + 1/2}\, \overline{\xi_\alpha(x)\xi^*_\alpha(y)} + \frac{n^0_\alpha}{n^0_\alpha + 1/2}\, \overline{\xi^*_\alpha(x)\xi_\alpha(y)}\Big]. \end{aligned} \quad (2.108)$$

[4] We added a superscript 0 to n_α to indicate that these are the initial values at time $t = 0$, in order to avoid possible confusion with the n_k.

The calculation is a straightforward free field exercise. Introducing the classical analogues of the creation and annihilation operators,

$$\varphi(x) = \sum_k \frac{e^{ikx}}{\sqrt{2\omega_k L}} (a_k + a^*_{-k}), \qquad \xi_\alpha = \sum_k \frac{e^{ikx}}{\sqrt{2\omega_k L}} (a_{\alpha k} + b^*_{\alpha -k}), \tag{2.109}$$

and accordingly for the canonical momenta π and η_α, we get

$$H_{\text{free}} = \sum_k \left[|a_k|^2 + \sum_\alpha \left(|a_{\alpha k}|^2 + |b_{\alpha k}|^2 \right) \right] \omega_k, \tag{2.110a}$$

$$Q_\alpha = \sum_k \left[|a_{\alpha k}|^2 - |b_{\alpha k}|^2 \right]. \tag{2.110b}$$

It follows that

$$\begin{aligned} n_k + \frac{1}{2} &= \overline{|a_k|^2} + \sum_\alpha \left(\overline{|a_{\alpha k}|^2} + \overline{|b_{\alpha k}|^2} \right) \\ &= \frac{T}{\omega_k} + \sum_\alpha \left(\frac{T}{\omega_k - \mu_\alpha} + \frac{T}{\omega_k + \mu_\alpha} \right). \end{aligned} \tag{2.111}$$

The μ_α are to be determined by the conditions

$$\begin{aligned} n^0_\alpha + \frac{1}{2} &= \overline{Q_\alpha} = \sum_k \left(\overline{|a_{\alpha k}|^2} - \overline{|b_{\alpha k}|^2} \right) \\ &= \sum_k \left(\frac{T}{\omega_k - \mu_\alpha} - \frac{T}{\omega_k + \mu_\alpha} \right). \end{aligned} \tag{2.112}$$

Before turning to the case $n^0_\alpha = 0$ used mostly in this paper, we comment on the properties of the above equations. Suppose there is only one complex mode function ("quantum mechanics"): $N = 1$. Then the solution of the equations is given by

$$\mu = \sqrt{\omega^2 + \frac{T^2}{(n^0 + 1/2)^2}} - \frac{T}{n^0 + 1/2}, \tag{2.113a}$$

$$n + \frac{1}{2} = \sqrt{\left(n^0 + \frac{1}{2} \right)^2 + \frac{T^2}{\omega^2}} + \frac{T}{\omega}, \tag{2.113b}$$

for which $n \geq n^0$. We see that $\mu \to \omega$, $n \to n^0$ as $T \to 0$, and $\mu \to 0$, $n \to \infty$ as $T \to \infty$.

For finite N, eq. (2.112) for μ_α can be rewritten as a polynomial equation of degree 2N by multiplying the LHS and RHS by $\prod_k(\omega_k^2 - \mu_\alpha^2)$. So there are in principle 2N solutions for each μ_α. For $T \to 0$ we have a solution in which $\alpha \leftrightarrow k$ (as in (2.29b), behaving as

$$\mu_k = \omega_k - T/(n_k^0 + 1/2) + \cdots, \qquad n_k = n_k^0 + \cdots. \tag{2.114}$$

For the case $n_\alpha^0 \equiv 0$ it is natural to look for a solution in which all the chemical potentials are equal, $\mu_\alpha = \mu$. Eq. (2.112) then reduces to

$$\begin{aligned} \frac{1}{2} &= 2T\mu \sum_k \frac{1}{\omega_k^2 - \mu^2} \approx 2TL\mu \int_0^\Lambda \frac{dk}{\pi} \frac{1}{m^2 + k^2 - \mu^2} \\ &\approx \frac{TL\mu}{\sqrt{m^2 - \mu^2}}, \end{aligned} \tag{2.115}$$

for large volumes $mL \gg 1$ and large momentum cutoff $\Lambda/m \gg 1$ (the integral converges for $\Lambda \to \infty$). It follows that

$$\mu \approx \frac{m}{\sqrt{1 + 4T^2L^2}}. \tag{2.116}$$

On the other hand, we have from (2.111),

$$n_k + \frac{1}{2} = \frac{T}{\omega_k} + \frac{2NT\omega_k}{\omega_k^2 - \mu^2}, \tag{2.117}$$

which depends explicitly on the number of modes N. We see that $n_k + 1/2$ falls roughly like $1/\omega_k$, and there is a danger that n_k may get negative for large ω_k, which should not happen.

In fact, in our numerical simulations we always found the n_k to be positive, however it di not follow the distribution (2.117) for all k. Even after very large times we usually find that only a limited number of modes are able to thermalize approximately classically, except for small systems such as in Fig. 2.10.

If we approximate

$$N = \sum_k \approx L \int_0^\Lambda dk/\pi = L\Lambda/\pi, \qquad \omega_\Lambda \approx \Lambda, \tag{2.118}$$

the condition

$$n_\Lambda + 1/2 \approx 2TN/\Lambda \geq 1/2 \tag{2.119}$$

leads to

$$LT \geq \pi/4. \tag{2.120}$$

If this condition is not satisfied, more complicated solutions for the chemical potentials may be needed in which $\mu_k \approx \omega_k$, as in (2.114). We have explored such solutions on the lattice, using Mathematica. Despite ambiguities (e.g. funny behaviour of the alternating lattice modes), such solutions indicate that $n_k \omega_k$ is quite constant (but apparently not exactly), i.e. approximate equipartition.

So we tentatively conclude that, approximately, $n_k \approx T_{cl}/\omega_k$ is the predicted form for the particle distribution at very large times.

CHAPTER 3

STAYING THERMAL

In the previous chapter we introduced the Hartree ensemble approximation, which allows for non-perturbative inhomogeneous field configurations, as well as for approximate thermalization. We studied this latter phenomenon starting from far out-of equilibrium initial conditions. In this chapter we will further investigate the approximation in order to determine the different time scales present in the theory. We will therefore use ensembles with a *free* field thermal distribution as out-of-equilibrium initial conditions. The time scale characterising the time for which the system stays in approximate quantum thermal equilibrium is an indication of the time scales for which the approximation method stays reasonable. In the range of couplings and temperatures studiedi, it turns out to be two orders of magnitude larger than the time scale for thermalization.

In order to obtain more information about the intermediate time regime, in which the slower equilibration of the higher momenta takes place, but when the system is still behaving as being in approximate thermal equilibrium, we will also investigate the damping time, which has some unexpected features in 1+1 dimensions.

The final topic addressed in this chapter will be methods to reduce the numerical cost of solving all the inhomogeneous mode functions. We will therefore study the possibility of reducing the number of mode functions and its limiting case, the the use of classical dynamics.

3.1 INITIAL CONDITIONS

In order to solve the equations of motion (2.18), we must specify initial conditions for the mean field $\varphi^{(i)}$ and the modes $f_\alpha^{(i)}$ of the individual Hartree trajectories as well as the weights p_i of the Hartree ensemble (cf. Section 2.5). This amounts to specifying the initial density operator $\hat{\rho}$. As explained in the introduction, Chapter 1, we use coherent (pure) states to represent the initial density operator, hence

we use initial modes functions as in the vacuum state (with the initial particle density n_α^0 equal to zero), as in equation (2.82).

We will not choose the initial φ as far out of equilibrium as we did in Chapter 2, where we took a superposition of only a few low momenta modes. Here we choose the mean fields from an ensemble with a Bose-Einstein (BE) distribution for the φ and π momentum modes as in (1.6),

$$p_k(\varphi_k, \pi_k) \propto \exp[-(e^{\omega_k/T_0} - 1)(\pi_k^2 + \omega_k^2(\varphi_k - \delta_{k0}v)^2)/2\omega_k]. \tag{3.1}$$

Then the initial density operator is that of a free field thermal *quantum* ensemble (cf. Appendix 2.A),

$$\hat{\rho} = \prod_k \int d\varphi_k d\pi_k \; p_k(\varphi_k, \pi_k)|\varphi_k, \pi_k\rangle\langle\varphi_k, \pi_k| \propto e^{-\hat{H}_0/T_0}. \tag{3.2}$$

It should be stressed that this ensemble is *not* in equilibrium, even though the particle densities we compute from the initial conditions (after averaging over a large number of realisations) have a BE distribution. This is clear, because the mode functions do not contribute at all to the initial particle density. In each individual run we therefore expect quick excitation of the mode functions from their vacuum state, i.e. quantum particles will be created, using energy from the mean field. Moreover we use the free field dispersion relation $\omega_k^2 = m^2 + [2 - 2\cos(ak)]/a^2$ in the initial distribution (3.1), with the zero temperature mass $m \equiv m(0)$. In thermal equilibrium this should become the temperature dependent mass $m(T)$ of the quasi-particles. Nonetheless we expect that these initial conditions will lead to a much faster thermalization than initial conditions of the form (2.95).

3.2 WEAK COUPLING

In the previous chapter, using the far out-of-equilibrium initial conditions (2.95), we found that particles of increasingly higher energy are created and acquire densities with a BE distribution. However, this thermalization progressed rather slowly to high energies, such that the low momentum particle densities already started to deviate from a BE distribution before particles with energies of a few times the temperature could participate in the equilibrium. These two phenomena – particles being created with densities that have a BE distribution and the gradual emerging of equipartition-like features – will be investigated below using the thermal initial conditions (3.2).

To probe the large time behaviour we shall use stronger coupling and higher energy densities than in the previous Chapter 2. However, first we show results at the same coupling as used there. The coupling constant $\lambda/m^2 = 1/2v^2 = 1/12$

is in the "broken symmetry phase" of the model. We will use a somewhat smaller volume $Lm = 25.6$, with a lattice cut-off $1/am = 10$.

As before, we plot $\log(1 + 1/n_k)$ rather than n_k itself, because in this way a BE distribution shows up as a straight line with a slope equal to the inverse temperature. The scattering in the data points is due to the use of only a few Hartree realisations (only two initial conditions). The result at low temperature, $T_0/m = 1$, is plotted in Figures 3.1a-c. It shows the evolution is very slow and there is hardly a sign of emerging classical features even at the largest time $tm \approx 50\,000$. Even though the particle distribution does not change, there is a persistent, slow transfer of energy from the mean field into the modes. At $tm = 200$, 50% of the energy is still in the mean field, at $tm = 6000$ this has dropped to 25% and at $tm = 50\,000$ it is still some 15%. The effective mass stays roughly constant, $m(T)/m \approx 0.94$, which is consistent with the prediction from the effective potential for $T_0/m = 1$.

At higher temperature, $T_0/m = 5$, but with the same weak coupling, there is again a wide window in which the particles have a BE distribution without significant distortions, see Figures 3.1d-f. However, we see classical-like features emerging for $tm \gtrsim 4000$: compared to the BE distribution, the low momenta modes become under-occupied, while the high momenta modes become over-occupied. We find that, at the latest time $tm \approx 50\,000$, the distribution for $\omega/m \lesssim 7$ can be described reasonably well with an ansatz $n_k = c_0 + T_{cl}/\omega_k$. Without the constant $c_0 \approx 0.25$ the fit would be poor.

In this simulation we find an interesting behaviour of the effective mass, shown in Fig. 3.2. For comparison, we also show in Fig. 3.3 the effective mass calculated using the Hartree effective potential at the same model parameters. First the mass is steadily decreasing, which is appropriate when the temperature is decreasing and the system is in the hot, symmetric phase. At $tm \approx 14000$ there is a sharp turnover and the mass starts to increase, as in the cold, broken phase. The temperature at that point $T_{cl}/m \approx 1.6$, obtained from a classical fit, is close to the temperature $T_c/m = 1.8$ of the first order phase transition, computed from the effective potential.[1] Also the average mean field fluctuates around zero before and around $v \approx 1.8$ after the transition, reasonably close to the effective potential prediction $v \approx 2$ for $T/m \sim 1.6 - 1.8$. The reasonable quantitative agreement between the simulation, which shows classical features, and the effective potential computation, which assumes a BE distribution, illustrates that the thermal mass is dominated by the low-energy particles, for which there is little difference between a BE and classical distribution.

[1] Recall that in the exact theory there would be a cross-over instead of a first order phase transition.

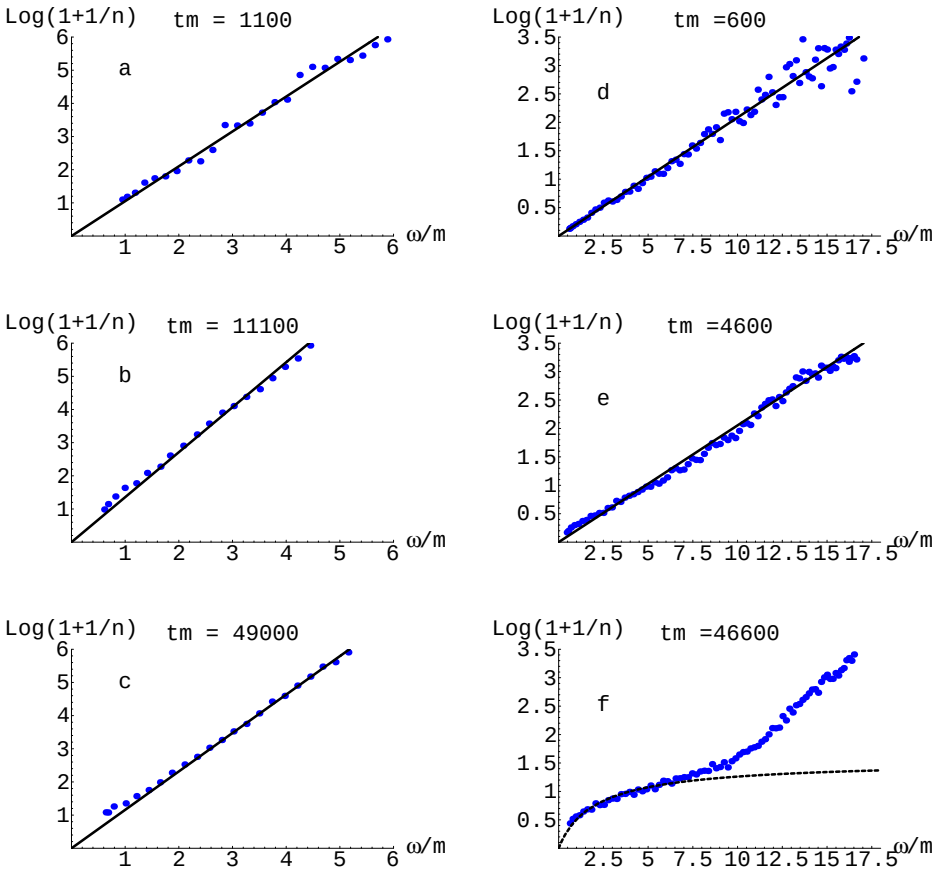

Low initial temperature $T_0/m = 1$.

High initial temperature $T_0/m = 5$.

Figure 3.1: Particle densities as a function of energy, plotted as $\log(1 + 1/n)$. The model parameters are: $\lambda/m^2 = 1/2v^2 = 1/12$, $Lm = 25.6$, $1/\alpha m = 10$.

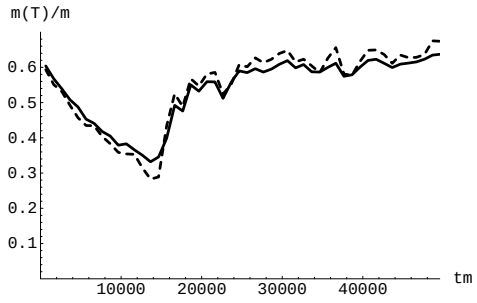

Figure 3.2: Time dependence of the effective thermal mass $m(T)$ for the same model as shown in Figs. 3.1d-f. The mass is determined as the lowest energy ω_0 (dotted line) or from a quadratic fit to the dispersion relation (full line).

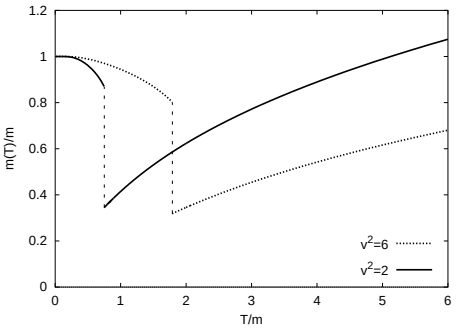

Figure 3.3: Temperature dependence of the effective mass computed using the Hartree effective potential, $\lambda/m^2 = 1/4$ (solid line) and $1/12$ (dotted line), $mL = 16$ (the volume dependence is very small).

3.3 STRONGER COUPLING

We now turn to the stronger coupling $\lambda/m^2 = 1/2v^2 = 1/4$, in order to make processes evolve faster. In Fig. 3.4a we show particle densities n_k computed only from the mode functions. We ignore the contribution from the mean field in (2.61), because we want to focus on the particles described by the mode functions. In Fig. 3.4a one sees that already after a short time, $tm \gtrsim 10$, particles have been created over a wide range of energies, $\omega/m \lesssim 6$. The densities are reasonably well described by a BE distribution with a time dependent temperature. This temperature initially increases rapidly from $T/m = 0$ at $tm = 0$ to $T/m \approx 0.6$ at $tm = 10$ and then gradually increases further to $T/m \approx 0.9$ at $tm = 100$. (Recall that the temperature of the initial condition is $T_0 = m$.)

Figs. 3.4b-c, which are obtained using both the modes and mean fields in the computation of the correlation functions, show that the densities of particles with large momenta tend to remain at a BE distribution also for later times, with a very slowly increasing temperature $T/m = 0.93 - 1.13$. However, one also clearly sees deviations from the BE distribution developing, starting at the low ω-side of the spectrum.

From these data we infer two time scales: First there is the rate at which the

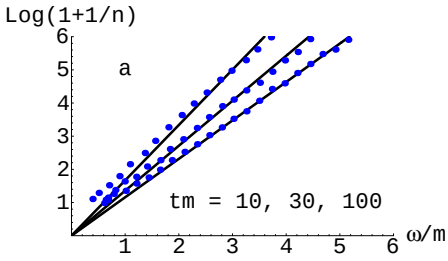

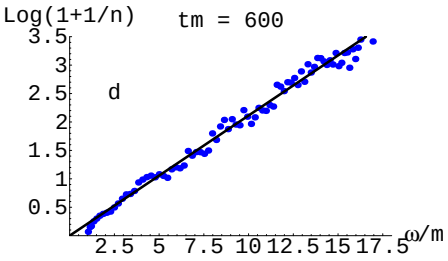

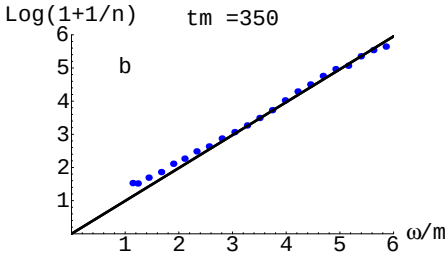

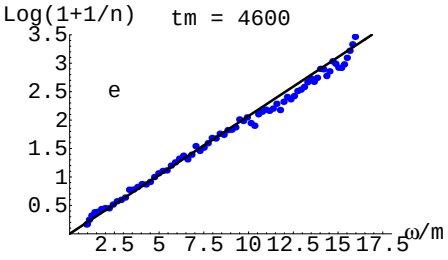

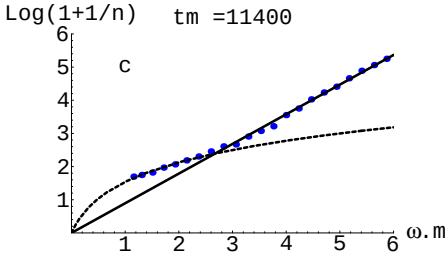

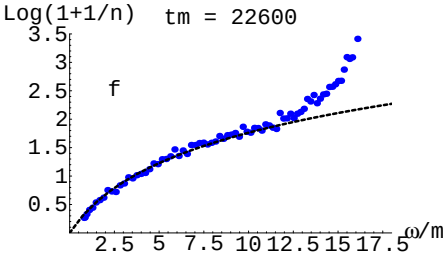

Low initial temperature $T_0/m = 1$.

High initial temperature $T_0/m = 5$.

Figure 3.4: The same as Fig. 3.1, but at a stronger coupling $\lambda/m^2 = 1/4$.

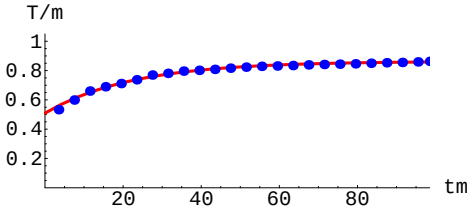

a: BE temperature, from the modes only.

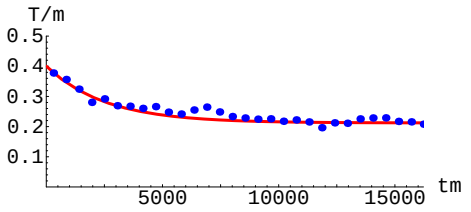

b: Classical temperature, from the modes and mean field.

Figure 3.5: Time dependence of temperatures for the data of Figs. 3.4a-c.

temperature of the BE distribution of the quantum particles is established. Second there is a rate at which the classical-like distribution sets in. Fig. 3.5 shows the time dependence of these two processes. The BE temperature was computed by fitting $\log(1+1/n) = \omega/T$ (only using the mode function contribution) for $2 \lesssim \omega/m \lesssim 4$. The classical temperature was found from fitting $n = T_{cl}/\omega$ for $\omega/m \lesssim 2$. The time dependence of these temperatures is reasonably well described by an exponential approach to an equilibrium value,

$$T_{BE}(t) = A - Be^{-t/\tau_{BE}} \qquad \text{and} \qquad T_{cl}(t) = A' + B'e^{-t/\tau_{cl}}. \tag{3.3}$$

We find $m\tau_{BE} \approx 20$ and $m\tau_{cl} \approx 2500$, showing quantitatively that the approximate BE thermalization happens much faster than the emergence of classical-like behaviour (Note that T_{cl} becomes much lower than T_{BE}, which itself is somewhat smaller than T_0, in agreement with the eventually expected classical equipartition).

At higher initial temperature, the distribution roughly follows the same development. Surprisingly enough the distribution keeps its approximate BE form much longer, while at higher temperatures one expects a stronger effective coupling, and thus shorter time scales. In Figs. 3.4d-f the initial temperature is $T_0/m = 5$. At this higher temperature and on a correspondingly larger energy scale, the deviations from a BE distribution appear less pronounced at early times. But even at $tm = 4600$ the particle densities are reasonably well described by a BE distribution with a temperature $T/m \approx 4.8$. At this time, there is a small reduction of the density of low momentum particles (n is up to 15% smaller than the BE density, but this is hard to see on the log-plot). At the same time the density of particles, with ω/m in the region $10-12$, increases a little. This trend continues and at $tm = 22600$ there is classical behaviour for $\omega/m \lesssim 12$.

The dashed line in Fig. 3.4f is a fit of the form $n = T_{cl}/\omega$, which gives a "classical" temperature $T_{cl}/m \approx 2.1$. The good quality of this fit for $\omega/m \lesssim 12$ suggests that the BE distribution gradually turns over into classical equipartition. How-

λ/m^2	1/12		1/4	
T_0/m	1	5	1	5
$m\tau_{BE}$	35	35	25	25
$m\tau_{cl}$	> 15000	3000-5000	2500-3500	2000-5000

Table 3.1: Results for the BE equilibration time, τ_{BE}, and the time scale for the drift towards classical equipartition, τ_{cl}, obtained from fits to T_{BE} and T_{cl} as in Fig. 3.5, as well as similar fits to the time dependence of $\sum_k n_k$.

ever, for still larger times the distribution is no longer well described by a simple $n \propto 1/\omega$-dependence. We did not determine the final equilibrium distribution, because of the extremely long (computer) time this would require.

In Table 3.1 we summarise our results for τ_{BE} and τ_{cl}, including also fits to the time dependence of the particle density $\sum_k n_k$, computed from the modes only or mean field plus modes, as in Figs. 3.5. These results do not show a clear dependence on the coupling or temperature, contrary to the expectation of much smaller time scales at higher temperature and/or stronger coupling. We believe that this is accidental, due to the fact that at $T_0/m = 5$ and/or $\lambda/m^2 = 1/4$ the system is in the "symmetric phase", while it is in the "broken phase" for $T_0/m = 1$ and $\lambda/m^2 = 1/12$. In Chapter 4, where we will discuss the symmetric phase in great detail, we will see that in this phase the system evolves much more slowly than in the "broken phase". Further note that the numbers in the table are subject to systematic uncertainty, since the mode system starts far from equilibrium and the time dependence not always follows an unambiguous exponential relaxation. This applies in particular for the simulation at $\lambda/m^2 = 1/4$, $T_0/m = 1$, which is very close to the "phase transition".

Besides looking at the particle number distribution, it is interesting to follow the effective mass $m(T)$ in time. Comparing it with the temperature dependence computed analytically using the Hartree effective potential, as in Section 2.3, gives another measure for the effective temperature of the system. The simulation of Figs. 3.4a-c gave an effective mass which increased slightly in the range $m(T)/m = 0.84 - 0.89$. From the effective potential calculation we then infer that the temperature should be in the range $0.5 \lesssim T/m \lesssim 0.7$, i.e. in the "low temperature" phase of the model, cf. Fig. 3.3, this is confirmed by checking the values of the mean field. This temperature is considerably lower than the BE temperature $T/m = 1.0(1)$, estimated from the particle distribution at higher momenta, but is consistent with the temperature obtained from fitting n_k at the smaller ω_k with a classical distribution. The same is found for the high-temperature simulation of Figs. 3.4d-f: $m(T)/m$ decreases from 1.12 at the start to 0.60 at $tm = 22600$, which corresponds, using the

effective potential, to a decrease from $T/m \approx 5$ to $T/m \approx 2$, consistent with the observed $T_{cl}/m \approx 5$ to $T_{cl}/m \approx 2.1$. As mentioned before, the difference between the classical and BE distribution is unimportant for the dominant n_k, those at low momenta.

3.4 DAMPING RATE: TWIN PEAKS

Thus far, we have discussed the initial equilibration of the low momentum modes of the $\lambda\varphi^4$ system. We found their particle distribution to approach the Bose-Einstein form, with a time scale of $tm = 15 - 20$. We also looked at the late time regime, and studied the approach towards a classical-like distribution, with a time scale of about two orders of magnitude larger. However, the intermediate regime, in which the higher momenta modes of the distribution approach the Bose-Einstein form rather more slowly, we have not yet described in detail. To get more information in this regime we will now turn to auto-correlation functions.

3.4.1 INTRODUCTION: NUMERICAL RESULT

For a homogeneous ensemble at finite temperature, the spatial Fourier transform $F_k(t)$ of the symmetrised auto-correlation function

$$F_k(t-t') = \int dx\, e^{-ik(x-x')} \left[\frac{1}{2}\langle\{\hat{\varphi}(x,t), \hat{\varphi}(x',t')\}\rangle - \langle\hat{\varphi}(x,t)\rangle\langle\hat{\varphi}(x',t')\rangle\right] \qquad (3.4)$$

can be expressed in terms of the spectral function by standard formulae, which we will discuss in Section 3.4.2. In case of weak coupling the spectral function is expected to exhibit a strong peak around the mass shell of the quasi-particles, which leads to exponential decay of $F_k(t)$ in an intermediate time regime. The decay rate is called "the plasmon damping rate".

In the Hartree ensemble approximation $F_k(t)$ can be written as the sum of a mean field part and a contribution from the mode functions. It is easiest to compute the mean field part. This would give no information in case of constant mean fields, since it would be identically zero. However, we expect mean field and modes to be sufficiently coupled to gain useful information on the damping rate, when only the mean field part us used. Even at late times $tm = 30\,000 - 80\,000$ we observed the back reaction $3\lambda\sum_\alpha |f_\alpha(x,t)|^2$ of the modes on the mean field to be strongly fluctuating in space and time. Fluctuations in the modes will then cause corresponding fluctuations in the mean field.

We have numerically computed the mean field part $F_{0mf}(t)$ at $k = 0$, obtained

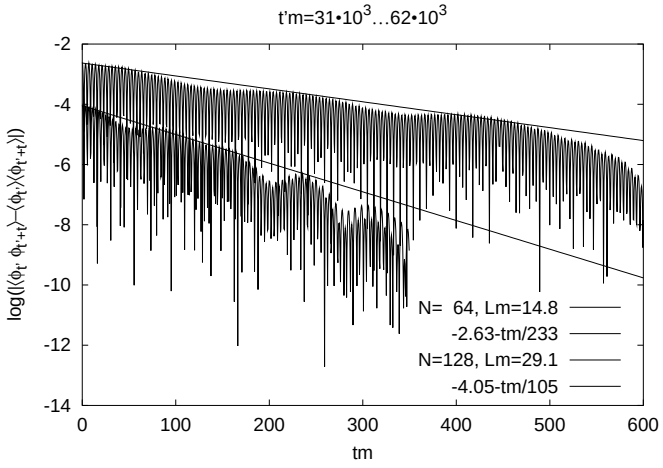

Figure 3.6: Numerically computed auto-correlation functions $\log|F_{0mf}(t)|$ versus time t in units of the inverse temperature dependent mass m_T. The coupling is weak, $\lambda/m_T^2 = 0.11$. The temperature $T/m_T \approx 1.4$ for the smaller volume (with significant deviations from the Bose-Einstein distribution) and ≈ 1.6 for the larger volume (reasonably BE).

by taking a time average after an initial equilibration period $t \in (0, t_0)$:

$$\begin{aligned} F_{0mf}(t) = &\frac{1}{(t_1 - t_0)} \int_{t_0}^{t_1} dt'\, \tilde{\varphi}_0(t+t')\tilde{\varphi}_0(t') \\ &- \frac{1}{(t_1 - t_0)^2} \int_{t_0}^{t_1} dt'\, \tilde{\varphi}_0(t+t') \int_{t_0}^{t_1} dt'\, \tilde{\varphi}_0(t'). \end{aligned} \tag{3.5}$$

where

$$\tilde{\varphi}_0(t) = \frac{1}{\sqrt{L}} \int_0^L dx\, \varphi(x,t) \tag{3.6}$$

No average was taken over initial conditions. Fig. 3.6 shows two examples of $F_{0mf}(t)$, for which the average was taken, after an equilibration time of $t_0 m \approx 31000$, over the interval $(t_0 m, t_1 m) \approx (31000, 62000)$. We see roughly exponential decay modulated by oscillations. At first the oscillations looked suspicious to us, as if there were strong memory effects and no damping, but other simulations *with* averaging over initial conditions (to be discussed in the next chapter) gave similar results. A natural question is now, does $F_k(t)$ also have such modulations?

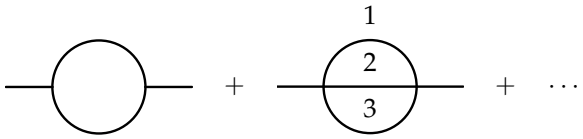

Figure 3.7: Diagrams leading to thermal damping.

3.4.2 CALCULATION OF $F(t)$

The function $F(t)$ can be expressed in terms of the zero momentum spectral function $\rho(p^0)$,

$$F(t) = \int_{-\infty}^{\infty} \frac{dp^0}{2\pi}\, e^{-ip^0 t} \left(\frac{1}{e^{p^0/T} - 1} + \frac{1}{2} \right) \rho(p^0), \tag{3.7}$$

and the latter in turn in terms of the retarded self-energy $\Sigma(p^0)$,

$$\rho(p^0) = \frac{-2\mathrm{Im}\,\Sigma(p^0)}{[m^2 - (p^0 + i\epsilon)^2 + \mathrm{Re}\,\Sigma(p^0)]^2 + [\mathrm{Im}\,\Sigma(p^0)]^2}. \tag{3.8}$$

The self-energy can be calculated in perturbation theory. The one and two loop diagrams in the imaginary time formalism which have nontrivial energy-momentum dependence are shown in Fig. 3.7. Diagrams not shown give only rise to an effective temperature dependent mass, which we assume to be the mass in the propagators of the diagrams in Fig. 3.7, after adding a counterterm that sets the real part of Σ to zero at $p^0 = m$. The one loop diagram is present only in the "broken phase", for which $\langle\hat{\varphi}\rangle \neq 0$; remember there is really only a symmetric phase in 1+1 dimensions, but this is due to symmetry restoration by non-perturbative effects which will not obliterate the one-loop damping. The corresponding self-energy has been calculated in Ref. [50], for example. It only leads to damping for frequencies $p_0^2 > 4m^2$, which are irrelevant for the quasi-particle damping at $p_0^2 = m^2$. So from now on we concentrate on the two-loop diagram. After analytic continuation to real time one finds that it is given by the sum of two terms, $\Sigma_1 + \Sigma_2$ (see e.g. Ref. [51]). The first has an imaginary part corresponding to $1 \leftrightarrow 3$ processes requiring $p_0^2 > 9m^2$, so it does not contribute to plasmon damping. The second is given by

$$\begin{aligned}\Sigma_2 = &-\frac{9\lambda^2}{16\pi^2} \int \frac{dp_2\, dp_3}{E_1 E_2 E_3} \frac{(1+n_1)n_2 n_3 - n_1(1+n_2)(1+n_3)}{p^0 + i\epsilon + E_1 - E_2 - E_3} \\ &+ \left[(p^0 + i\epsilon) \to -(p^0 + i\epsilon)\right],\end{aligned} \tag{3.9}$$

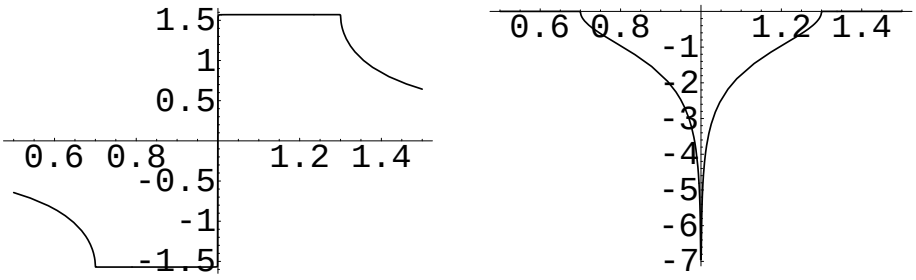

Figure 3.8: Real (left) and imaginary (right) part of $-i\log\left(i/z+\sqrt{1-1/z^2}\right) = \arcsin(1/z)$, equation (3.11), for $z=(p^0+i\epsilon-m)/(0.13m)$, $m=1$, $\epsilon/m=10^{-4}$.

where λ is the coupling constant (introduced as $\mathcal{L}_1=-\lambda\varphi^4/4$), and

$$E_1=\sqrt{m^2+(p_2+p_3)^2}, \qquad E_i=\sqrt{m^2+p_i^2}, \qquad i=2,3;$$
$$n_i=\frac{1}{\exp(E_i/T)-1}, \qquad i=1,2,3.$$

Its imaginary part corresponds to $2\leftrightarrow 2$ processes, which contribute to plasmon damping in the regions near $p_0=\pm m$.

Now the usual definition of the thermal plasmon damping rate (at zero momentum) in terms of the retarded self-energy,

$$\gamma=-\mathrm{Im}\,\Sigma(m)/2m, \tag{3.10}$$

leads to a logarithmically *divergent* answer. This is a collinear divergence which is absent in more than one space dimension. Inspection shows that the singular part of Σ_2 is given by the non-relativistic region of the integral in (3.8). Using polar coordinates $p_2=p\cos\varphi$, $p_3=p\sin\varphi$ this non-relativistic ($p<\kappa\ll m$) contribution is proportional to

$$\int_0^\kappa p\,dp\int_0^{2\pi}\frac{d\varphi}{2\pi}\,\frac{1}{p^0+i\epsilon-m+(p^2/2m)\sin 2\varphi} = m\left[-i\log\left(\frac{i}{z}+\sqrt{1-\frac{1}{z^2}}\right)\right], \tag{3.11a}$$

$$z=\frac{p^0+i\epsilon-m}{\kappa^2/2m}, \tag{3.11b}$$

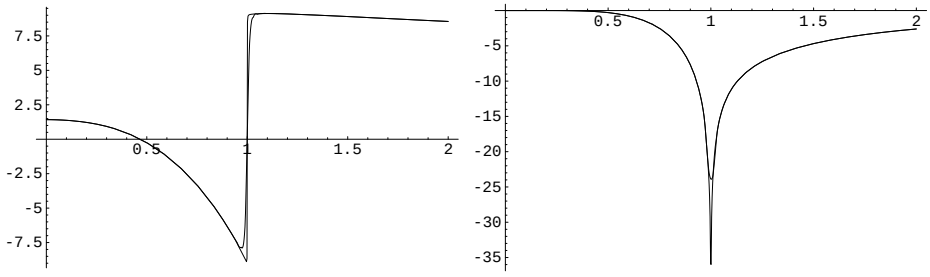

a: Real part. b: Imaginary part.

Figure 3.9: Plot of $\Sigma(p^0)/(9\lambda^2/16\pi^2)$ obtained by linear extrapolation $\epsilon = 0.02, 0.01$ to zero, together with a matching to the logarithmic singularity ($T = m = 1$).

where $p^0 \approx m$. This function is plotted in Fig. 3.8.

A natural way out of this difficulty may be to continue the self-energy analytically into the lower half of its second Riemann sheet, $p^0 \to m - i\gamma$, and replace (3.10) by the improved definition

$$m^2 - (m - i\gamma)^2 + \Sigma(m - i\gamma) = 0. \tag{3.12}$$

The analytic continuation of the self-energy into the region $\mathrm{Im}\, p^0 < 0$ poses the puzzle how to deal with the logarithmic branch point coming from the collinear singularity at $p^0 = m$. However, the ambiguity is present only in the real part of Σ. For weak coupling $\lambda/m^2 \ll 1$ we get, from (3.12), the equation

$$\frac{\gamma}{m} = \frac{9\lambda^2}{16\pi m^4} \frac{e^{m/T}}{\left(e^{m/T} - 1\right)^2} \left[\log \frac{m}{\gamma} + c(T)\right]. \tag{3.13}$$

The constant c has to be determined by matching a numerical evaluation of Σ to the logarithmic singularity, eq. (3.11), at $p^0 = m$.

We evaluated Σ_2, equation (3.9), for $T = m$ by numerical integration with $\epsilon/m = 0.02, 0.01$ and linear extrapolation $\epsilon \to 0$. The result is shown in Figs. 3.9a and 3.9b, together with a matching to the logarithmic singularity, giving $c \approx -0.51$. For example, Eq. (3.13) now gives $\gamma/m = 0.061$, for $\lambda/m^2 = 0.4$.

To see how well this γ describes the decay of the correlator $F(t)$ we evaluated this function directly from (3.7) and (3.8). The divergence in $\mathrm{Im}\,\Sigma(p^0)$ at $p^0 = m$ leads to a *zero* in the spectral function $\rho(p^0)$. So is there a peak at all in $\rho(p^0)$? Fig. 3.10 shows what happens: the "usual" peak has separated into two twins!

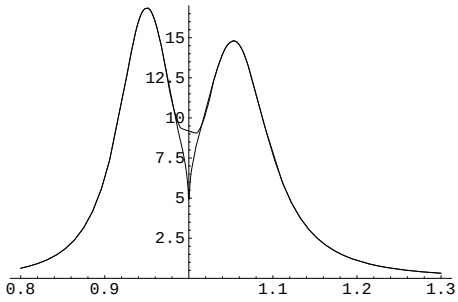

Figure 3.10: The spectral function $\rho(p^0)$ near $p^0 = m = 1$, corresponding to the self-energy shown in Figure 3.9 ($T = m$, $\lambda = 0.4m^2$).

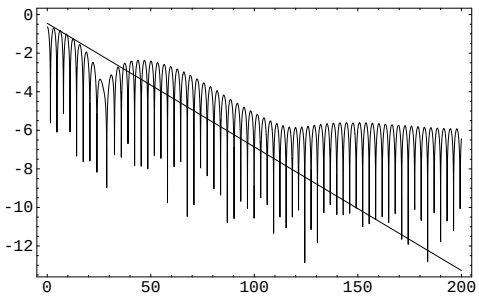

Figure 3.11: Plot of $\log|F(t)|$ versus mt for $T = m$, $\lambda = 0.4m^2$. The straight line represents $\exp(-\gamma t)$.

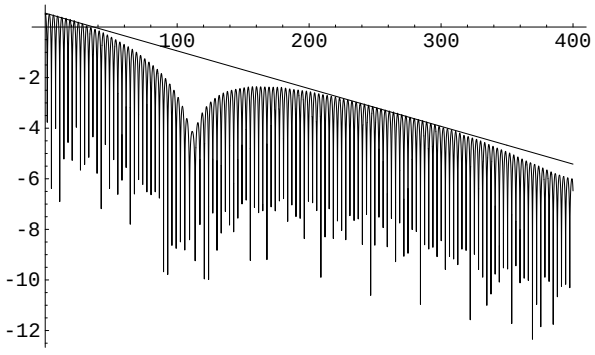

Figure 3.12: $\ln|F(t)|$ versus mt with $\lambda/m^2 = 0.11$, $T/m = 1.63$, corresponding to Fig. 3.6. The straight line is given by $\exp(0.55 - t/67)$.

Fig. 3.11 shows the resulting $F(t)$. The effect of the double peak is indeed an oscillating modulation on top of the roughly exponential decay. The decay corresponding to $\exp(-\gamma t)$, with γ given by (3.13), is also indicated in the plot: it does not do a good job in describing the average decay beyond the first interference minimum. The "Twin Peaks" phenomenon implies that the usual definition of damping rate (3.12) is unreliable in 1+1 dimensions. Fig. 3.12 shows the result of a calculation of $F(t)$ with parameters taken from the numerical simulation shown in Fig. 3.6, with the larger volume. In this case ϵ was kept finite, $\epsilon/m = 0.005$, which may be more realistic, since one expects damping effects in the propagators in the diagrams in Figure 3.7 to smear out the infinity in $\mathrm{Im}\,\Sigma$ anyway.

Figs. 3.6 and 3.12 are reasonably similar, the straight lines in Figure 3.6 indicate damping times $\tau m_T \approx 105$ and ≈ 233. We use the finite temperature mass here to set the scale as it appears naturally in resummed perturbation theory. For the first example (with the larger volume) the corresponding particle distribution was found to be reasonably of the Bose-Einstein form, with zero chemical potential and temperature $T/m_T \approx 1.6$. The two loop perturbative calculation gives a $\tau m_T \approx 67$ for this temperature, which we consider encouragingly close to the Hartree ensemble result ≈ 105. We should however warn the reader that the numerical computation of auto-correlation functions is quite difficult and that there may be large *statistical* errors in the numbers given.

Summarising, we are encouraged by the similarities in the qualitative features of the numerical and analytical auto-correlation functions. Quantitatively, the damping times are also of the same order of magnitude (105 versus $67m^{-1}$), but a really accurate computation of the relevant auto-correlation functions has not yet been done, as it will require a lot more numerical effort. We will leave the subject and turn to a different topic, numerical improvements of the method.

3.5 REDUCED NUMBER OF MODE FUNCTIONS

If the positive results for the performance of the Hartree ensemble method at shorter times carry over to more realistic models in $3+1$ dimensions, one has to confront the problem of the high computational cost of this approach. Taking the continuum limit on a finite volume in d dimensions, i.e. increasing the number of lattice sites N in each direction, the cost of our approach increases $\propto N^{2d+1}$: there are $O(N^d)$ fields which have to be updated $O(N)$ times, assuming a fixed value of the time-step a_0/a.

Most of this cost comes from having to solve all N^d mode functions f_α. However, many of these modes would represent particles with very high momenta $|k| \gg T$. Such particles have very low densities and should be irrelevant for the physics at lower scales. This suggests reducing the number of mode functions in

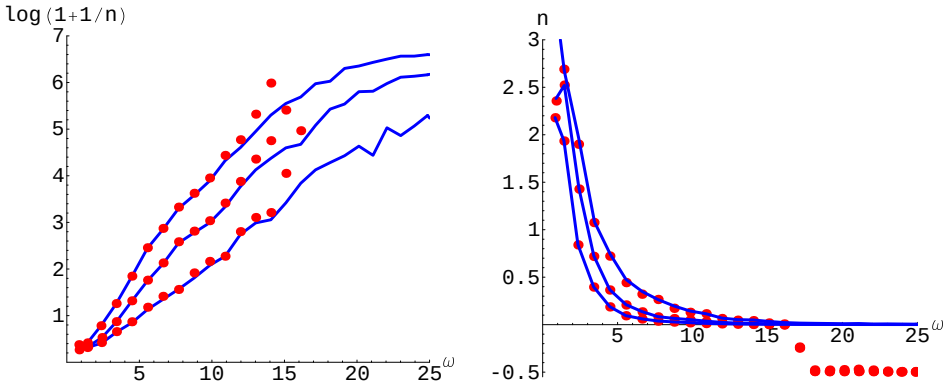

Figure 3.13: Particle densities at $tm = 50, 90, 300$, obtained from simulations using the full number of modes (drawn lines) and using only modes for which $\omega_k/m < 17 \approx 3T/m$. The left figure shows $\log(1 + 1/n_k)$, the right shows the density n_k itself ($Lm = 5.7$, $1/am = 22.3$ and $\lambda m^2 = 1/12$).

our simulations. We have tested this idea by comparing a simulation, on a lattice with $N = 128$ sites, using all 128 mode functions, with the same simulation using only 32 mode functions. This induces a maximum energy

$$\frac{\omega_{max}}{m} \approx \frac{\sqrt{2 - 2\cos(32\pi/128)}}{am} \approx 17, \tag{3.14}$$

which is much larger than the temperature $T/m \approx 6.8$ that we will use in the test. The ω_{max} here refers to the energy of the initial mode functions which are plane waves.

In order to make as detailed a comparison as possible, we show the results for the particle density obtained from the mode functions only, leaving out the contribution of the mean field in (2.61). As shown in Fig. 3.13, this partial distribution changes with time during thermalization (cf. Fig. 3.4a). The drawn lines represent the data obtained with the full number of mode functions. The dots represent the results obtained using the reduced number of modes. The left figure shows the familiar $\log(1 + 1/n_k)$ form of the density, the other figure shows the density n_k itself. As is evident, these results reproduce the data from the reference simulation, accurately up to $\omega/m \approx 12$, which is close to $\omega_{max}/m \approx 17$. Notice that the densities, computed from eq. (2.56), drop to $n = -0.5$ for $\omega/m \gtrsim 17$ (Fig. 3.13 right). For these high momenta there are no more mode functions available to provide the vacuum fluctuations that should lift the density to zero. It indicates that at high mo-

menta there is still a roughly one-to-one correspondence between mode functions and momentum labels of the particles.

3.6 CLASSICAL APPROXIMATION

Even using fewer mode functions, the Hartree approach is much more expensive than the classical approximation (which has no mode functions). So it is important to check if our results cannot in some way be mimicked by a classical approximation. The standard way to implement the latter at high temperature, is to average over initial configurations drawn from the Boltzmann distribution. Up to modifications by the interactions this implies a classical distribution function $n(\omega) = T/\omega$, with a slow fall off, causing Rayleigh-Jeans type divergences (actually, in $1+1$ dimensions such divergences are absent in $\varphi\varphi$-correlation functions [10]).

Here we want to ask a somewhat different question: to what extend can classical dynamics be used to represent a thermalized system with a Bose-Einstein distribution for the particle densities? To investigate this we shall use the same BE-type initial conditions (3.1) as in the Hartree case, as well as the much more out-of-equilibrium conditions of the form (2.95). We perform similar simulations and analyses as before, but now without mode functions, and with $n_k + 1/2 \to n_k$ in (2.56), as there is now no quantum vacuum contribution. Typically, the classical dynamics produces data with more noise, since the average contribution of the many mode functions tends to smoothen results in the Hartree-dynamics. We counter this noise by averaging over 40-50 initial conditions, which is more than we typically use with Hartree dynamics. We note in passing, that the necessity to use a larger ensemble to obtain data of the same quality as with Hartree dynamics, diminishes the computational advantage of using classical dynamics considerably.

At the same weak coupling and low temperature as in Figs. 3.1a-c, we find that the classical system also preserves the Bose-Einstein distribution of the initial conditions very well. Even at the largest simulated time, $tm = 50\,000$, there is no compelling sign of equipartition in the particle distribution. This, however, may only show that the relaxation time scale of the classical dynamics is very long, cf. [18], and that we are seeing remnants of the initial condition rather than thermalization.

To speed-up the dynamics, we increased the temperature to $T_0/m = 5$ and the coupling to $\lambda/m^2 = 1/4$, as was used in Figs. 3.4d-f for Hartree dynamics. The classical results are shown in Figs. 3.14a-c. Now the initial BE-distribution still persists for some time, however already at $tm \approx 600$ there are clear signs of equipartition setting in, whereas with Hartree dynamics, effects of similar magnitude only emerged at $tm \gtrsim 6000$. The gradual move from the initial state towards classical equipartition happens much faster than in the Hartree ensemble simulations.

Of course one might argue that this initial persisting of the BE distribution is

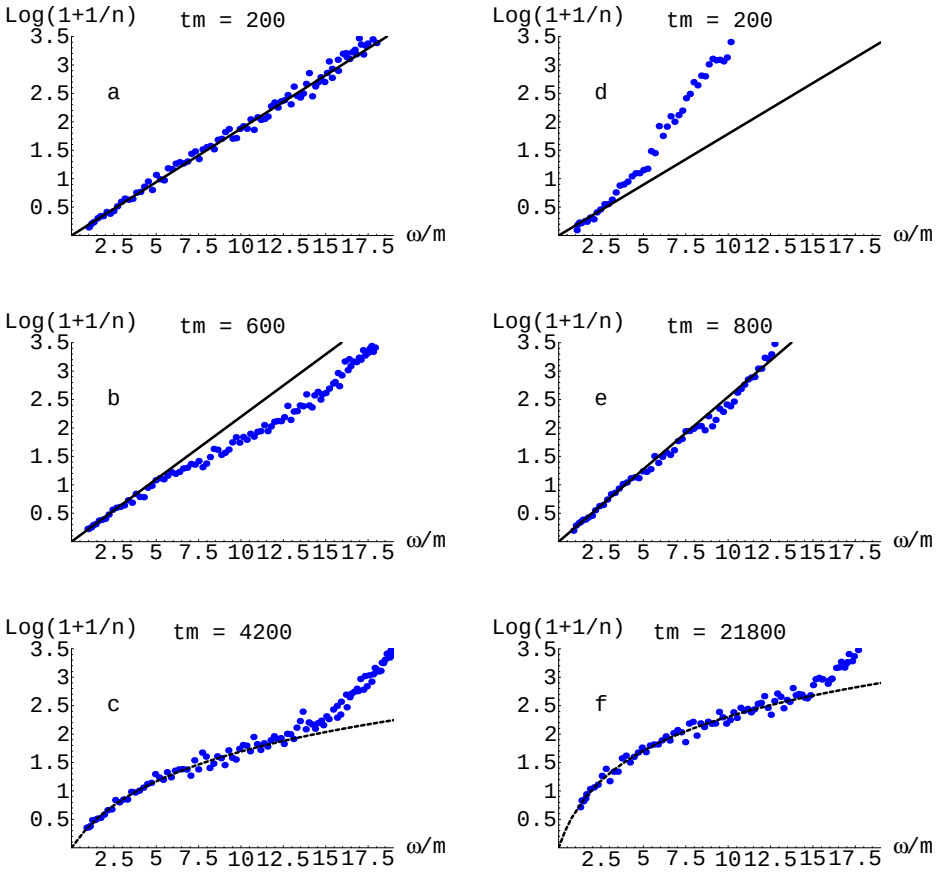

BE-type initial conditions with temperature $T_0/m = 5$.

Only a few of the low momentum modes of the mean field carried all energy.

Figure 3.14: Same as Figs. 3.4d-f, but using classical dynamics. $\lambda/m^2 = 1/4$, $Lm = 25.6$ and $1/am = 10$.

of little significance, since it only demonstrates that it takes time to loose the effect of the initial conditions. In more realistic models we might not be able to specify initial conditions sufficiently close to thermal equilibrium and then one may not expect to encounter a BE distribution. Yet, somewhat surprisingly, starting with the far out-of-equilibrium initial condition (2.95), we see that as the model steadily moves towards classical equipartition, the particles are distributed in a BE-like way in an intermediate stage. This can be seen in Figs. 3.14d-f, showing particle density distributions at simulation times in the range $tm = 200 - 20\,000$. At tm around 800 the particle densities follow a BE-like distribution over a wide range of energies. The coupling strength in this simulation is $\lambda/m^2 = 1/4$, at weaker coupling this intermediate stage with BE-like distribution persists longer. However, it always smoothly turns towards classical equipartition on much shorter time scales than when using Hartree dynamics (although, as mentioned earlier, the final equilibration to the classical distribution takes place on a very long time scale).

3.7 DISCUSSION

From the results in the previous chapter, combined with those from this chapter, the following picture has emerged for the 1+1 dimensional $\lambda\varphi^4$ model in the "broken phase": the initial energy, which is put solely in the mean field of a realisation, is subsequently transferred to the mode functions. This process takes place fairly locally in momentum space, i.e. mean field modes with momentum k excite primarily particle modes with momenta close to k, and the modes then thermalize locally to a BE distribution. In the previous chapter this approximate thermalization was more conspicuous because the initial distribution was further out of equilibrium. Here the BE distribution was put into the initial condition for the mean fields. However, the corresponding density operator is still out of equilibrium because of the "wrong" initial thermal mass. The thermalization process is fairly rapid, within a time $\tau_{BE} \approx 25-35\, m^{-1}$, for $\lambda/m^2 = 1/4, 1/12$ and $T_0/m = 5, 1$, as determined from the time-dependence of the BE temperature or the particle density $\sum_k n_k$ (cf. Table 3.1).

This time scale is similar to our findings with initial mean fields containing only low momenta, cf. Chapter 2. The subsequent thermalization of higher momenta is very slow. We ascribe this to a weakening of the non-linearities when the mean field looses much of its energy. When the mean field fluctuates around its (temperature dependent) equilibrium value, with diminishing amplitude, the dynamics becomes approximately that of Hartree with a homogeneous mean field, suggesting lack of thermalization. This also explains why the evolution to a classical-like distribution is much slower with the Hartree ensemble approximation than using classical dynamics.

However, the fluctuations die out very slowly and even at very large times of order $10^4\ m^{-1}$ there is still O(10%) of the energy in the fluctuating mean field. Nonlinear fluctuations remain, which lead eventually to classical-like equipartition (according to the effective Hamiltonian and conserved "charges", see Section 2.2). The time scale for such classical equipartition setting in, is one of the results of this chapter. We find that the system remains in an approximate quantal thermal state for times of the order $\tau_{cl} \gtrsim 100\,\tau_{BE}$ (cf. Table 3.1).

This is an encouraging result. For example, in a crude application of our 1+1 dimensional results to 3+1 dimensional heavy ion collisions, identifying m with the mass of the σ-resonance $m_\sigma = 600 - 1200$ MeV, say 900 MeV, a time-span of $100\,\tau_{BE} = 2000\,m^{-1}$ would correspond to a reasonable length of about 450 Fermi. Within such a time-span the Hartree ensemble method may be a definite improvement on the classical dynamics usually employed for e.g. the "disoriented chiral condensate".

For application to 3+1 dimensions it is important that the numerical efficiency of the Hartree method can be significantly improved by using only a limited number of mode functions, corresponding to particles with sufficiently high densities (see Sect. 3.5).

Leaving out the mode functions altogether, i.e. using classical dynamics, the results were qualitatively similar to those with Hartree dynamics, but the emergence of classical particle distributions happens faster by roughly an order of magnitude. So this may not be good enough for practical applications.

With respect to thermalization, it is good to keep in mind that in the Boltzmann approximation, the collision term corresponding to $2 - 2$ scattering is identically zero, due to kinematical constraints in the φ^4 model in 1+1 dimensions. So thermalization has to come from inelastic scattering and/or off-shell effects. It is then important to realise that such effects are more pronounced in the "broken phase" of the model, which has a three point vertex and finite (as opposed to zero) range interactions. As mentioned in Chapter 2 and will be explained in detail in Chapter 4, thermalization is drastically less efficient in the "symmetric phase" at similar values of λ/m^2. It is sobering to recall the huge thermalization times found in Ref. [18] in the classical approximation, in the "symmetric phase". For example, using $\lambda/m^2 = 1/4$, $T/m = 0.2$, the empirical formula (rewritten in our conventions),

$$1/m\tau_{cl} = 5.8\,10^{-6}(6\lambda T/m^3)^{1.39}, \tag{3.15}$$

leads to a relaxation time $m\tau_{cl} \approx 1.3\,10^5$. This is much larger than the $m\tau_{cl} \approx 2500$ found in the "broken phase" (Sect. 3.3).

An interesting question is how the two time scales τ_{BE} and τ_{cl} are related to particle scattering and damping. We presented a perturbative computation (which includes direct scattering through the setting-sun diagram), indicating that the damp-

ing time would be of the order of the BE-relaxation time τ_{BE} (i.e. much shorter than the relaxation time away from BE behaviour). Preliminary numerical results for the damping time were found to be consistent with these values.

This is a favourable result for the Hartree ensemble method. However the gradual drift away from a BE distribution and the corresponding cooling of the system reveals a shortcoming. This is additional to the incorrect prediction by the Hartree method, of the order of phase transitions. Further improvements are needed, in particular if large time scales are to be investigated.

CHAPTER 4

THE SYMMETRIC PHASE

In Chapter 2 we introduced the Hartree ensemble approximation and studied its thermalization properties in the "broken phase" at weak coupling. In Chapter 3 we further studied this system and derived time scales for the initial approximate thermalization and the late time "classicalization". So far we have not paid much attention to the "symmetric phase", and this will be the topic of this chapter. We will especially focus on the difference in the dynamical evolution of observables such as the particle distribution, energy exchange and auto-correlation functions. Approximate thermalization is found only for relatively large energy densities and couplings.

4.1 INITIAL CONDITIONS

In the simulations which will be discussed in this chapter, we used two different initial conditions for the mean field, a sum of standing waves with a flat distribution of phases, which we also used in the broken phase in Chapter 2, and a single Gaussian wave packet, as studied by Bettencourt et al. [52].

The first is given by equation (2.95):

$$\phi^{(i)}(x) = 0, \qquad \pi^{(i)}(x) = Am \sum_{j=1}^{j_{max}} \cos(2\pi j x/L - \psi_j^{(i)}), \tag{4.1}$$

where the maximum momentum $2\pi j_{max}/L$ is typically of the order of the mass m and the constants $\psi_j^{(i)}$ are random phases with a flat distribution (i.e. they are uniformly distributed in $[0, 2\pi)$). We shall call such $\rho[\phi, \pi]$ flat ensembles. The energy, which is independent of the phases ψ_j, is given by

$$\frac{E}{m} = \frac{A^2 L m j_{max}}{4} \tag{4.2}$$

We use both A and j_{max} to vary the total energy density.

The second initial condition is a Gaussian wave packet:

$$\pi(x) = 0, \qquad \phi(x) = \Phi \exp\left[-\frac{x^2}{2A}\right]. \tag{4.3}$$

Its energy is given by

$$\frac{E}{m} = \frac{\Phi^2}{8}\sqrt{\frac{\pi}{Am^2}}\left(2 + 4Am^2 + \sqrt{2}A\lambda\Phi^2\right). \tag{4.4}$$

We will restrict ourselves to $Am^2 = 2$ and use Φ to vary the total energy in the system. For this type of initial conditions we do not average over multiple runs, so $\rho[\phi, \pi]$ is a delta functional and $\hat{\rho}$ is a coherent pure state.

4.2 NUMERICAL RESULTS

In this section we will first discuss the particle distribution in order to study its equilibration behaviour and to search for thermalization. Then we will examine the energies and auto-correlation function to analyse the time scales in the theory.

4.2.1 FLAT ENSEMBLE

In the flat ensemble of initial conditions, the initial mean field ϕ of a realisation is equal to its vacuum expectation value 0, while its momentum is the sum of waves with random phase, as specified in (4.1). In the simulations an average was taken over 10 or 20 initial conditions, while all non-zero modes up to $k_{max} = 2\pi j_{max}/L = \pi m/2$ were excited. Simulations have been carried out for three different couplings $\lambda/m^2 = 1/6, 1/8, 1/12$ and three different energy densities $E/Lm^2 = 4, 2, 1$, as well as for the combination $\lambda/m^2 = 0.1$ and $E/Lm^2 = 0.4$. In most simulations, the number of lattics points $N = 128$, the volume $Lm = 32$, and the temporal lattice distance $a_0 = a/10$.

PARTICLE DISTRIBUTION FUNCTION

Figure 4.1 shows the particle number obtained for coupling $\lambda/m^2 = 1/6$ and energy density $E/Lm^2 = 4$. As in the previous chapters we compare the out-of-equilibrium particle densities with a Bose-Einstein (BE) distribution

$$n_k = \frac{1}{e^{(\omega_k - \mu)/T} - 1}, \tag{4.5}$$

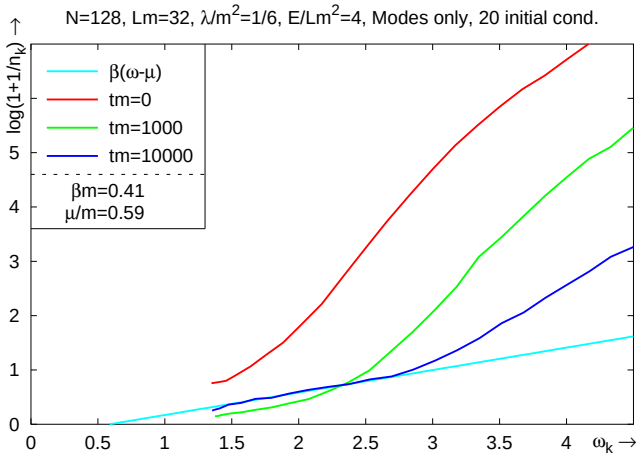

Figure 4.1: The particle numbers $\log(1 + 1/n_k)$ in the modes as a function of ω_k. Average over 20 flat ensemble initial conditions. $\lambda/m^2 = 1/6$, $E/Lm^2 = 4$, at times up to $tm = 10^4$. Time increases from the top curve to the bottom curve.

and therefore $\log(1 + 1/n_k)$ versus ω_k/m is plotted, since a BE distribution then shows up as a straight line with slope m/T and offset $-\mu/m$ (T temperature, μ chemical potential). For this largest coupling and energy density in our study, we find approximate thermalization to the BE form, with a temperature $T/m = 2.4$ and chemical potential $\mu/m = 0.6$. In contrast to what was found in the broken phase, a substantial chemical potential is needed to make a reasonable fit. Another difference is the larger time scale involved: in the broken phase at an energy density $E/Lm^2 = 0.5$ and the same $\lambda/|\mu^2_{\rm ren}| = 1/6$ ($\lambda/m^2 = 1/12$), we could already recognise BE behaviour with $T/m \approx 1$ at a time $tm \lesssim 100$, while here, at an 8 times larger energy and roughly 2 times larger effective BE temperature we can only clearly do so at time $tm \gtrsim 2000$. A fit of the local temperature $T(t)$ approaching approximate equilibrium gives an equilibration-time scale $m\tau_{\rm BE} = 1500 - 1600$ (exponential fit over $k/m < 1.7$, $100 < t < 6000$).

For most parameters used in Bose-Einstein features can be recognised in the low momentum part of the distributions, and linear fits can be made as in Figure 4.1. The results of these fits are shown in Table 4.1. Fits marked with a star were made at $tm = 59000 \cdots 60000$, all others at $tm = 9000 \cdots 10000$. Including the mean field in the two-point functions, typically gives the same temperature within errors, but a noticeably larger value (+ 0.05) for μ/m, corresponding to a higher particle num-

		$E/Lm^2 = 1$	$E/Lm^2 = 2$	$E/Lm^2 = 4$
$\lambda/m^2 = 1/6$	βm	1.12	0.71	0.41
	μ/m	0.95	0.83	0.59
$\lambda/m^2 = 1/8$	βm	0.89*	0.60	0.45
	μ/m	0.62	0.76	0.80
$\lambda/m^2 = 1/12$	βm	$--$	0.68*	0.40
	μ/m	$--$	0.76	0.85

Table 4.1: Inverse temperature β and chemical potential μ as derived from a Bose-Einstein fit to the particle numbers (modes only). See text for further explanation.

ber. The chemical potential is also more sensitive to the exact fit-interval than the temperature. In the two *-marked runs a thermal distribution could be recognised only at $tm \gtrsim 20000$ ($\lambda/m^2 = 1/12$) and $tm \gtrsim 45000$ ($\lambda/m^2 = 1/8$).

For the run at $\lambda/m^2 = 1/12$, $E/Lm^2 = 1$, we did not find a thermal-like distribution even at the latest simulation time $tm = 10^5$. We see that the energy is transferred from the mean field to the modes and the system equilibrates "locally in k", but the total particle number remains roughly unchanged. The same was found at the lower energy density $E/Lm^2 = 0.4$, and also for the Gaussian wave packet initial condition. We interpret this as a resonance phenomenon in the equation of motion of the mode functions, which will be described in Section 4.3.1.

Comparing the results at $E/Lm^2 = 2$ and 4 it seems that the temperature only depends on the energy density and not on the coupling. This appears to hold even for the particle distribution function itself, as illustrated in Figure 4.2, where the distributions for different couplings are plotted at different times. The different times, at which the curves in the figure overlap, suggest that the equilibration time scale for the particle distribution is proportional to λ^{-3}. The same power is found in the simulations at the energy density $E/Lm^2 = 2$. The results in Table 4.1 show that the temperature is roughly proportional to $\sqrt{E/L}$, which can be understood from the scaling behaviour in Figure 4.2: there is no other scale left. The same argument should apply to the chemical potential. However, this quantity is more dependent on time than the temperature and runs at different parameters are best compared at different times as in Figure 4.2, which we have not done in Table 4.1.

The independence of coupling suggests that a representation of the energy in terms of almost free quasi-particles will be reasonably good. This will be checked in the next section.

Figure 4.3 shows the distribution for late times, when it starts to deviate from the BE form. Note the difference in vertical scale compared to Figure 4.1. At $tm = 15000 - 20000$ classical-like deviations become visible in the form of concave be-

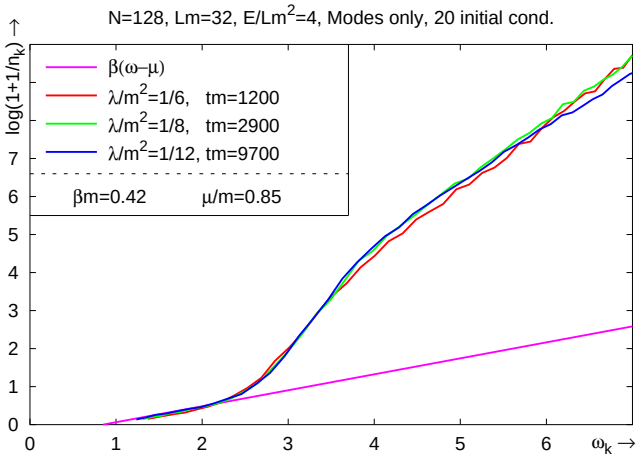

Figure 4.2: Scaling behaviour of the particle distribution at fixed energy density but differing couplings and times.

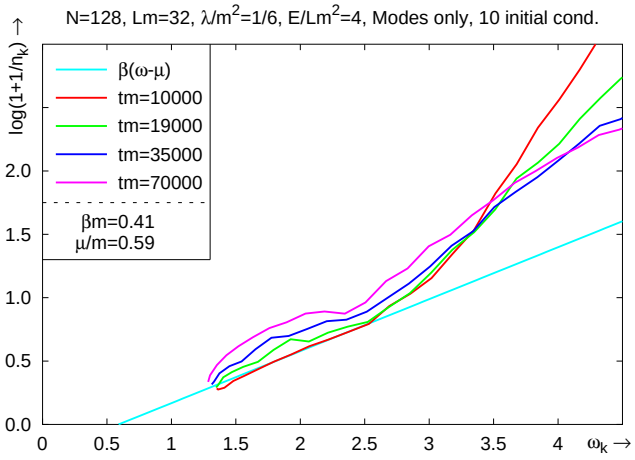

Figure 4.3: The particle numbers $\log(1 + 1/n_k)$ in the modes as a function of ω_k at large times $tm > 10^4$. In the small k region time increases from bottom to top, in the large k region time increases from top to bottom.

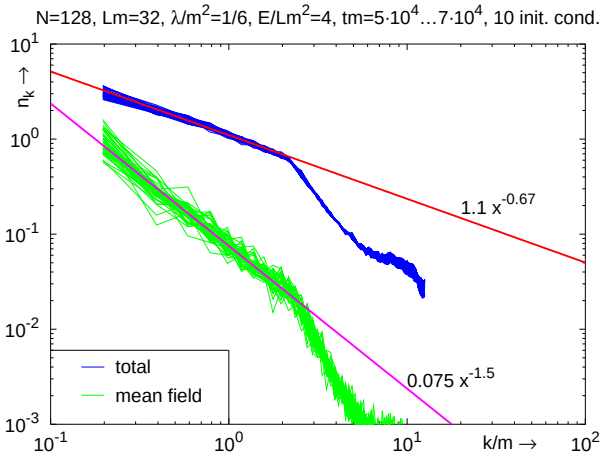

Figure 4.4: Log-log plot of the particle numbers for mean field alone, and combined with modes, versus k/m, at large times.

haviour at low ω_k: for $n_k = T/\omega_k$ the second derivative $\Rightarrow (\partial/\partial\omega_k)^2 \log(1+1/n_k)$ is negative.

The mean field in this time region behaves very interestingly. In Figure 4.4 we plotted the particle numbers at $tm = 50\,000 \cdots 70\,000$ as a function of momentum k, both for the mean field alone and for the total two-point function, using a log-log scale and leaving out the zero mode. While the high-momentum modes are still exponentially suppressed, the low-momentum modes have acquired a power-law distribution. The quantum-modes-only distribution does *not* behave as a power-law (cf. Figure 4.3). The particle numbers as obtained from the mean field only and those including the modes have different powers, -1.5 and -0.67 respectively. Already much earlier, around $tm = 8000$, this distribution starts to emerge, with 20% larger powers.

The power-law behaviour in the low momentum modes of the mean field apparently influences the quantum modes, in that their low momentum modes are enhanced in comparison to the classical T/ω_k. We have seen this clearly in a plot of $n_k\omega_k$ ($\to T$ for classical thermal equilibrium) which shows a peak at $k = 0$ and a "classical plateau" at the interval $k/m = 1.0 \ldots 2.2$. Similar behaviour has also been found in the other runs at $\lambda/m^2 = 1/6$, $E/Lm^2 = 2$ and $\lambda/m^2 = 1/8$, $E/Lm^2 = 4$.

In a purely classical simulation using the same set of parameters power-law behaviour is *not* found. This suggests that the interaction of the mean field with

with the quantum modes plays a crucial role, even though the latter do not show power-law behaviour.

TIME SCALES FOR ENERGY EXCHANGE

In the previous section we obtained the scaling behaviour $\propto \lambda^{-3}$ for the time scale of approximate equilibration based on the particle distribution. In this section we will use the energy density in the different parts of the field, as in (2.44), to find the short-time equilibration behaviour. Figure 4.5 shows the results from one of the simulations at $\lambda/m^2 = 1/6$, $E/Lm^2 = 4$, plotted at different time scales. In Figure 4.5a, showing the early stage, the energy as obtained from the quasi-particles is also included. The quasi-particle picture appears to give a reasonable representation of the energies, with a roughly constant 10% mismatch in the total energy. We furthermore see that the total energy in the quasi-particle picture is almost constant, corresponding to a quasi-particle number that is itself almost constant. This is consistent with the chemical potential found in the BE fits. We have checked that the dispersion relation of the quasi-particle energies is close to that of free particles, $\omega_k = \sqrt{m_{\text{eff}}^2 + k^2}$, but with an effective mass m_{eff} that is larger than m, in concordance which the effective potential. m_{eff} can be obtained from e.g. the minimum values of ω_k in Figure 4.1.

Looking at the contributions E_{mf} and E_{modes} to H_{eff}, we see a relatively rapid transfer of energy from the mean field to the modes until a time of the order $tm \approx 50$. This exchange takes place fairly locally in momentum space, as is found by examining the mean field and mode contributions to n_k, a phenomenon that we call local k-space equilibration. At time $tm \approx 100$ most of the particle number already comes from the modes, whereas the total distribution is still reasonably close to its initial form. After this time $tm \approx 50$, energy is still going to the modes, but with a slower rate. The behaviour in this second region, from $tm \approx 50$ till $tm \approx 2000$, (see Figure 4.5b) can be fitted reasonably well with an exponential form

$$A + Be^{-t/\tau}, \tag{4.6}$$

yielding $\tau m \approx 100 - 150$. If we look at the long time behaviour, as plotted in Figure 4.5c, we see there is also a much longer time scale of the order 6000, on which energy is going back into the mean field. This time scale is comparable to the time scale of the emerging power-law behaviour, discussed in Section 4.2.1. The appearance of this power law is accompanied by a large increase in the particle number in the zero mode of the mean field and therefore also in the average energy density of the mean field. We recall that classical behaviour only becomes visible at larger time scales of the order 15000.

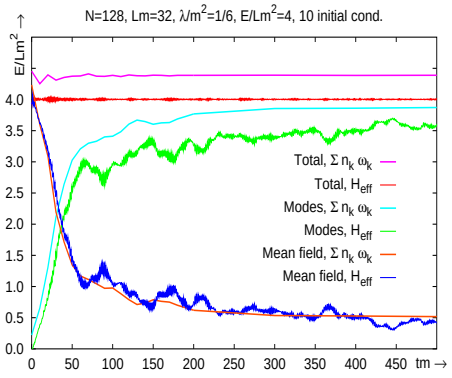

a: Short times. From top to bottom at $tm = 450$: $\sum_k n_k \omega_k$ (mean field + modes), E from H_{eff}, $\sum_k n_k \omega_k$ (modes only), E_{modes}, $\sum_k n_k \omega_k$ (mean field), E_{mf}.

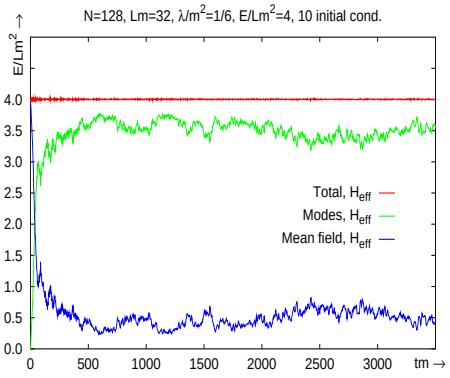

b: Intermediate times.

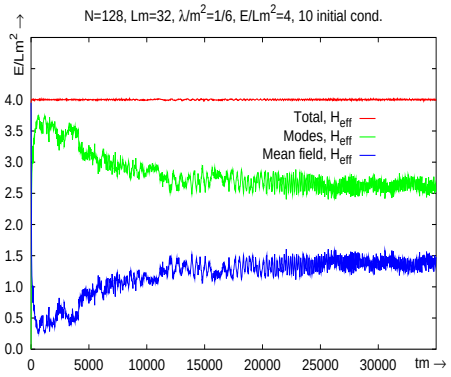

c: Long times.

Figure 4.5: Different contributions to the energy density for the flat ensemble at high energy-density $E/Lm^2 = 4$ and stronger coupling $\lambda/m^2 = 1/6$.

τm	$E/Lm^2 = 1$	$E/Lm^2 = 2$	$E/Lm^2 = 4$
$\lambda/m^2 = 1/6$ ($tm < 500$)	137	70	39
$\lambda/m^2 = 1/8$ ($tm < 800$)	215	108	50
$\lambda/m^2 = 1/12$ ($tm < 2500$)	688	207	112

Table 4.2: Initial energy-exchange time scales for the flat-ensemble initial conditions.

τm	Peak 1 & 2	Peak 1 & 3
symmetric, Hartree	160 ± 31	360 ± 35
symmetric, classical	90 ± 18	156 ± 34
broken, Hartree	49 ± 11	84 ± 14
broken, classical	41 ± 14	63 ± 16

Table 4.3: Auto-correlation times for flat ensemble type initial conditions. In all cases the coupling $\lambda/|\mu^2_{ren}| = 1/6$. In the symmetric phase $v^2 = 0$, $\lambda/m^2 = 1/6$ and $E/Lm^2 = 4$, whereas in the broken phase $v^2 = 6$, $\lambda/m^2 = 1/12$, and $E/Lm^2 = 0.5$.

In order to make a quantitative comparison between different couplings and energies for the initial rapid exchange of energy between mean field and modes, related to the local thermalization, we fitted the energy-density in the mean field to a function of the form (4.6). The results are summarised in Table 4.2. Using the energy in the quasi-particle picture, instead of the effective Hamiltonian, gives the same results.

Leaving out the run at the lowest coupling and energy, $\lambda/m^2 = 1/12, E/Lm^2 = 1$, which we did not see thermalize, the time scale is roughly proportional to E^{-1} at constant coupling and to $\lambda^{-3/2}$ at constant energy density:

$$\tau^{-1} \approx Cm(E/Lm^2)(\lambda/m^2)^{3/2}. \tag{4.7}$$

We have checked this behaviour explicitly by plotting the different energies as a function of $(\lambda/m^2)^{3/2}(E/Lm^2)\,t$, from which we obtained $C = 0.10$.

For the lower energy density $E/Lm^2 = 0.4$ the results are very similar to our simulation of the Gaussian wave packet, which we will describe in Section 4.2.2. In particular, we encountered the local k-space equilibration. By initially exciting only a few modes this process can be seen even more clearly. We have not simulated

long enough at this low energy density, using the flat initial distribution, to see the emergence of classical behaviour.

AUTO-CORRELATION TIME SCALES

To further investigate time scales, we also analysed the time-dependent auto-correlation function of the mean field, as in Section 3.4. Using flat ensemble initial conditions in both the symmetric and the broken phase, with either Hartree or classical dynamics, the auto-correlation function was obtained from the average mean field only:

$$C(t) = \overline{\langle \bar{\phi}(t_0 - t/2)\bar{\phi}(t_0 + t/2)\rangle}^{t_0} - \text{d.c.} \tag{4.8}$$

Here $\bar{\phi}(t)$ denotes the spatially averaged mean field, the overline indicates averaging over a large time-interval (which greatly reduces fluctuations) and the initial ensemble, d.c. stands for the disconnected piece. Figure 4.6 shows an example in the large-time region, where the particle-number distribution has the behaviour shown in Figure 4.4. The average was taken over the time interval $tm = 50\,000 \ldots 70\,000$, and ten initial configurations from the flat ensemble. We recall that the evident damping is seen also upon using only a single configuration, such as was done in Section 3.4, it is not caused by the average over initial conditions. The dip-like structure can be understood as being caused by interfering "twin peaks" in the spectral function, as explained in Section 3.4.2. The damping time is quantified using a "fit" of the form $\exp(-t/\tau)$ through the first and second peak. Using the third peak would give a roughly twice as large τ. The results are given in Table 4.3, where the errors are obtained with the jackknife method [53]. In the table a comparison is made with results from the classical approximation, and with results obtained in the broken phase.

In the broken phase there is hardly any difference between the classical and the Hartree result, although the Hartree result seems to indicate a slightly larger value. We recall that the particle distribution in this case approximates the Bose-Einstein form reasonably well, and furthermore, that the damping time is within a factor of two of the analytically computed value using perturbative quantum field theory in the two-loop approximation.

In the symmetric phase the Hartree result is roughly twice the classical value. It is hard to interpret this in any detail as the distribution function in the Hartree case is so "unconventional" (cf. Figure 4.4) and also the classical case is far from thermalized. However, there is a much more striking difference between the broken- and symmetric-phase results. At an eight times larger energy, the auto-correlation time in the symmetric phase is not smaller, but instead larger by a factor $3-4$. One would expect qualitatively the opposite effect. For example, for a thermalized system at a temperature T, the damping rate may be expected to scale, in the classical approx-

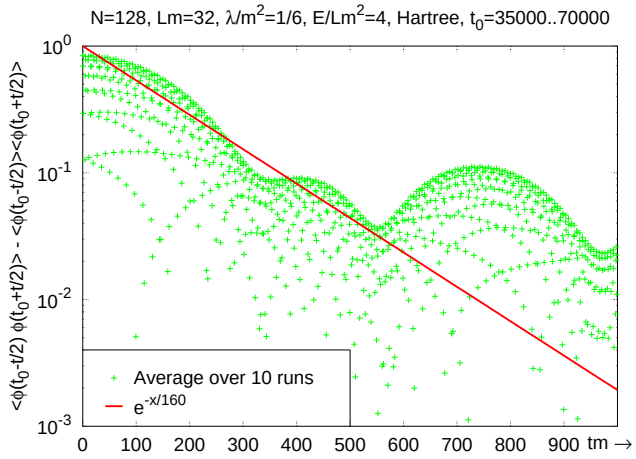

Figure 4.6: Auto-correlation function for the average mean field using the flat Hartree ensemble. The lower "arcs" are an effect of sampling the oscillations $\propto \log|\cos m_{\rm eff} t|$ at discrete times.

imation, as $(\lambda T)^{1/3}$, and bluntly using the values $\lambda T/m^3 = (1/6)(1/0.41)$ (symmetric, Table 4.1) and (1/12) 1.1 (broken, Section 2.7.3) would give $\tau_{\rm symm}/\tau_{\rm broken} = 0.62$ instead of the factor $3-4$.

Comparing with the time scale for energy exchange, we see that at high energy density the damping time is $4-9$ times larger than the energy-exchange time (cf. Table 4.3 and the upper-right entry in Table 4.2). The systematics of this are unclear to us, since at the lowest energy density (and smaller coupling) we find on the contrary that the damping time is about half the time scale for energy exchange (see also Sect. 4.2.2 for the Gaussian wave packet: $\tau_{\rm damp} \approx 3500$, $\tau_{\rm exch} \approx 7000$).

4.2.2 GAUSSIAN WAVE PACKET

In this section we focus on the initial condition specified by the Gaussian wave packet (4.3) with $\lambda/m^2 = 0.1$, $Am^2 = 2$ and $\Phi = 2.60106$ (this value appeared in the preprint version of [52]), which gives an energy $E/m^2 = 12.6$. We used a volume $Lm = 32$, giving an energy density $E/Lm^2 = 0.394$ which is practically equal to the smallest energy density 0.4 studied in the previous section with the flat ensemble. It is however still an order of magnitude larger than the highest energy densities studied in [52]. In this case the number of lattice points $N = 256$, while

the temporal lattice distance $a_0 = a/10$, as before. We checked for finite volume and discretization effects by using different parameters and found that they do not influence the results discussed.

PARTICLE DISTRIBUTION FUNCTION

The initial Gaussian wave packet spreads and oscillates in the course of time and after $t \gtrsim L/2$ the packet meets itself due to the periodic volume. This can be seen from the plots of the mean field $\phi(x)$, see Figure 1 in [52], which we have verified.

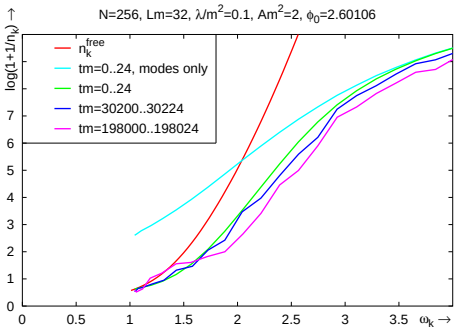

Figure 4.7: Time development of particle number. The order in the key corresponds to the curves from top to bottom at $\omega_k/m = 2.5$.

The initial wave-packet (4.3) represents a pure state, that can still be analysed in terms of particle numbers and frequencies obtained from the two-point functions, as in (2.56). It is interesting to compare the so-obtained n_k with the coarse-grained particle distribution at later times. If we assume free-field evolution we can calculate n_k analytically, and it turns out that its average over (half) an oscillation period is time-independent and close to the initial distribution, for large volumes. As derived in Appendix 4.A this free-particle distribution for the Gaussian wave packet initial condition (4.3) is given by

$$n_k^{\text{free}} = \frac{\pi A \Phi^2 \sqrt{m^2 + k^2}\, e^{-k^2 A}}{L}. \tag{4.9}$$

In Figure 4.7 we plotted this free form, together with the particle numbers obtained in a simulation. We find it quite remarkable that already the earliest (time-averaged) distribution deviates significantly from the initial form (4.9). A closer look shows that this deviation originates entirely from the first period $tm = 0 \ldots 2\pi$. After that short time the distribution is almost stationary. Only after a time $tm = \mathcal{O}(10^5)$ we see deviations arise. However, in the mean time there is an extensive exchange of energy between the modes and the mean field: initially all particle number and energy is contained in the mean field, while in the later stage it is just the opposite.

After $tm \approx 30000 - 40000$ classical behaviour, i.e. $n_k \to T/\omega_k$, starts to emerge: the lower-momentum modes become under-occupied, while the higher modes be-

come over-occupied. At no stage does the distribution resemble the the Bose-Einstein form (4.5). We recall that also with the flat ensemble we did not see quantum thermalization at similarly low energy densities.

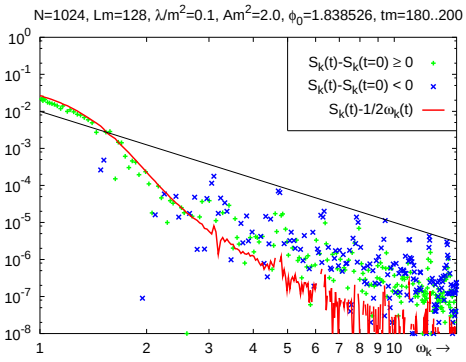

Figure 4.8: The power spectrum $S_k(t) - S_k(0)$ and $n_k(t) - 1/2\omega_k(t) = S_k(t) - 1/2\omega_k$ for $tm = 180 \cdots 200$. The line represents a power $\propto \omega^{-3}$ touching the negative values of $S_k(t) - S_k(0)$.

Bettencourt et al. [52] studied the power spectrum of the subtracted two-point function $S_k(t) - S_k(0)$ at times $tm \lesssim 200$. This appeared to show power behaviour $\sim k^{-3} - k^{-4}$, which was interpreted as evidence for the absence of BE-like thermalization. As mentioned above we also see no BE thermalization at this low energy density, however we find that the power behaviour is not without ambiguities. The aim of the subtraction in $S_k(t) - S_k(0)$ was to eliminate the vacuum contribution $1/2\sqrt{m^2 + k^2}$ from S_k. At large k this is a rather delicate procedure, for instance, a quasi-particle behaviour

$$S_k(t) = \frac{n_k(t) + 1/2}{\sqrt{m(t)^2 + k^2}}, \tag{4.10}$$

with a thermal-like mass $m(t)$ that is expected to be larger than m in the symmetric phase, would give a negative result at large k,

$$S_k(t) - S_k(0) \approx -\frac{m(t)^2 - m^2}{4k^3}, \tag{4.11}$$

were we neglected an assumed exponentially small $n_k(t)$.

We would like to stress here the good features of the observables n_k and ω_k defined in (2.56). In Fig. 4.8 we have plotted

$$S_k(t) - 1/2\omega_k(t) = \frac{n_k(t)}{2\omega_k(t)}, \tag{4.12}$$

as well as $S_k(t) - S_k(0)$, for the same parameters ($\Phi = 1.838526$, $Am^2 = 2$, $Lm = 128$, $N = 1024$) and in the same time regime as used in [52]. (We averaged over $tm = 180 - 200$, which hardly affects $n_k(t)/2\omega_k(t)$ as it is practically constant.) The plot of $S_k(t) - S_k(0)$ looks very similar to the ones shown in Ref. [52]. There is a lot of scatter at large ω_k ($\approx k$) and a more detailed analysis shows negative values

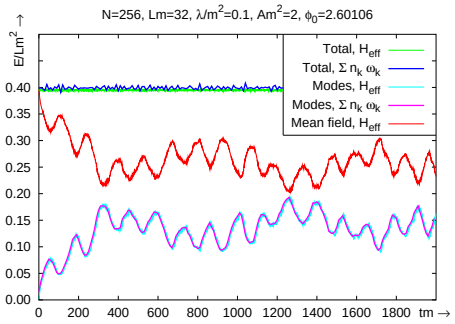

a: Short times. From top to bottom: energy from modes and mean field, energy from mean field, energy from modes.

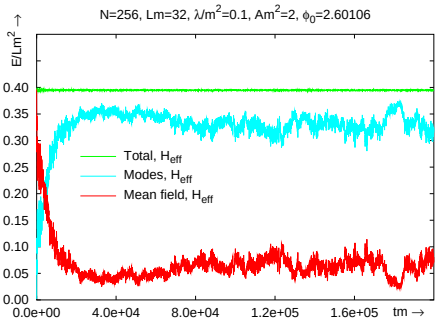

b: Long times.

Figure 4.9: The different energies for the Gaussian wave packet initial condition.

interspersed with positive values (indicated separately for the power spectrum. On the other hand $n_k/2\omega_k$ shows less scatter and is mostly positive (only for $\omega_k > 4$ do negative values occur). Note however, that the larger ω region could be affected by lattice artifacts.

ENERGY DENSITIES AND TIME SCALES

To get an estimate of the time scales involved, we compare the energy densities in the mean field, in the modes and in the total field for the Gaussian wave packet initial condition, as we did in Sect. 4.2.1 for the flat ensemble at higher energy densities. For short times these are plotted in Figure 4.9a, together with the energy as derived from the quasi-particle picture (2.60). For long times they are plotted in Figure 4.9b.

We see that the quasi-particle representation of the energies is in this case extremely good, there is hardly any visible difference with the exact energies based on H_{eff}.

Furthermore, for early times (Fig. 4.9a) there is an oscillatory behaviour with a period $tm \approx 130$. Note that, due to the periodic boundary conditions on the system with size $Lm = 32$, the Gaussian packet already "meets itself" after a time $tm = 16$, much shorter than this resonance time. The resonance is caused by the difference between the effective mass terms of the modes and mean field, $\approx 2\lambda\phi^2$. This mass-difference has a small value, fluctuating around $0.030 - 0.050$, corresponding to a period $210 - 126$, approximately the observed period.

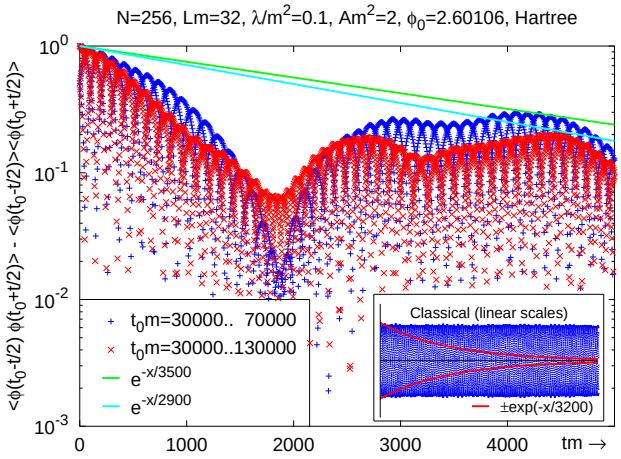

Figure 4.10: The auto-correlation function as determined from the average mean field only. The result when using classical dynamics is shown in the insert on a linear scale, with an exponential fit to the Hartree result.

The rate at which energy flows to the modes can be seen at long times (Fig. 4.9b). The energy in the mean field in the interval $tm < 60\,000$ can be fitted reasonably well to an exponential function of the form (4.6), yielding an equilibration time scale $\tau m \approx 7000$, roughly two orders of magnitude larger than what was found in the broken phase at similar energy densities and couplings.

Using a sum of waves as initial condition at similar energy density shows the same kind of resonance in the energy exchange between mean field and modes, with period ≈ 170 and mass difference fluctuating around $0.02 - 0.04$, consistent with the found period. When an average is taken over the flat ensemble, the oscillations die out after $tm \approx 4000 - 5000$.

TIME SCALES FROM THE AUTO-CORRELATION FUNCTION

We also evaluated the auto-correlation function for the Gaussian wave packet. Since we do not average over initial conditions we cannot calculate a statistical error. We therefore averaged over two different time intervals, giving some idea of the size of the statistical uncertainty. The result is plotted in Figure 4.10. At this low energy, the damping time is roughly half the energy equilibration time. The inset shows – on a linear scale – the result for classical dynamics, using identical initial con-

ditions. The exponential curve is a fit to the Hartree result: classically there is no visible damping.

It would be interesting to compare the result with the flat initial ensemble at the same energy density. However, for these low energies we need to simulate for very long times, which is quite a numerical effort. We therefore only calculated the autocorrelation times for the faster evolving high energy runs discussed in Section 4.2.1.

4.3 SCATTERING

In this section we will discuss scattering features of the Hartree approximation. We shall give an interpretation of our finding that the initial mean-field particle-distribution is approximately taken over by the modes, the modes appear to equilibrate with the mean field, primarily when they have the same wave number. We call this "local k-space equilibration". Such a process occurs especially at low energy density and weak coupling. After a discussion of higher-order scattering and thermalization we end with a fresh look at the possibility of scattering of two localised wave packets: they *can* scatter indeed in the Hartree approximation, especially in the broken phase.

4.3.1 LOCAL k-SPACE EQUILIBRATION

The effective Hamiltonian (2.22) can be seen as describing interacting classical fields ϕ and f_α. It will be convenient to split the modes f_α in a free part and a perturbation:

$$f_\alpha = f_\alpha^0 + g_\alpha, \qquad f_\alpha^0 = \frac{e^{ik_\alpha x - i\omega_\alpha t}}{\sqrt{2\omega_\alpha L}}, \tag{4.13}$$

with $\omega_\alpha^2 = m^2 + k_\alpha^2$. We will show in the following, that for not too large coupling and energy, the equation of motion for g_α reduces to that of a driven harmonic oscillator. Making use of the corresponding scattering diagrams we then conclude that, approximately, the only momentum modes of g_α that are excited are those also present in the mean field. Since we will focus on the initial behaviour, when the system is still far from equilibrium and there is no temperature yet, we will only use zero-temperature perturbation theory.

We can write out the effective Hamiltonian in terms of the classical fields ϕ, g_α and the external field f_α^0. In the symmetric phase and to second order in g_α, this

leads to the following interaction terms and corresponding vertex factors

$$\frac{1}{4}\lambda\phi^4 \qquad 6\lambda \tag{4.14a}$$

$$3\lambda\phi^2\sum_\alpha \mathrm{Re}(f_\alpha^0 g_\alpha^*) \qquad 3\lambda \tag{4.14b}$$

$$\frac{3}{2}\lambda\phi^2\sum_\alpha |g_\alpha|^2 \qquad 3\lambda \tag{4.14c}$$

$$6\lambda\sum_{\alpha,\beta}\mathrm{Re}(f_\alpha^0 g_\alpha^*)\mathrm{Re}(f_\beta^0 g_\beta^*) \qquad 3\lambda \tag{4.14d}$$

whereas in the broken phase, writing $\phi = v + \phi'$, we also have the three-point interactions

$$\lambda v\phi'^3 \qquad 6\lambda v \tag{4.15a}$$

$$6\lambda v\phi'\sum_\alpha \mathrm{Re}(f_\alpha^0 g_\alpha^*) \qquad 3\lambda v \tag{4.15b}$$

$$3\lambda v\phi'\sum_\alpha |g_\alpha|^2 \qquad 3\lambda v \tag{4.15c}$$

In a first approximation we neglect the back-reaction on the mean field and assume it is just oscillating around its minimum as a superposition of waves:

$$\phi(x,0) = \sum_{i=1}^{i_{max}} A_i \sin(\omega_{K_i} t)\cos(K_i x - \psi_i) \tag{4.16}$$

where ψ_i are random phases and $\omega_{K_i} = \sqrt{m^2 + K_i^2}$.

The exact Hartree dynamical equation for the mode perturbation $g_\alpha(x)$ in terms of its Fourier transform $g_{\alpha k}$ is given by

$$(\partial_t^2 + \omega_k^2)g_{\alpha k} = -3\lambda\int dx\left(\phi(x)^2 + C_{ren}(x)\right) \times\left(\frac{e^{i(k_\alpha - k)x - i\omega_\alpha t}}{\sqrt{2\omega_\alpha}} + \frac{1}{L}\sum_{k'} e^{i(k'-k)x} g_{\alpha k'}\right). \tag{4.17}$$

Neglecting for the moment the higher order terms, those containing C_{ren} and $g_{\alpha k}$ in the integral, the x-integration can be performed, resulting in a sum over plane waves. The equation is that of a driven harmonic oscillator

$$(\partial_t^2 + \omega_k^2)g_{\alpha k}(t) = \sum_j B_j e^{-i\Omega_j t}, \tag{4.18}$$

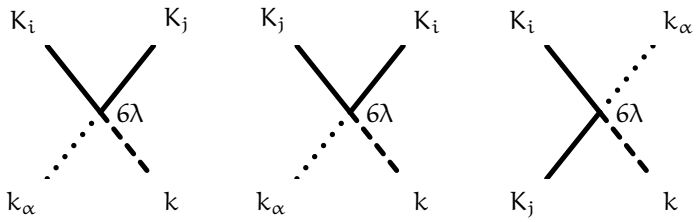

Figure 4.11: Tree level scattering diagrams involving a single perturbation mode g_α. Drawn lines denote ϕ, a dotted line f^0_α, and the dashed line denotes g_α. Time runs from left to right.

which leads to resonances that grow linearly in time for $\omega_k^2 = \Omega_j^2$. By inserting the explicit form (4.16) in (4.17) we find for each pair K_i, K_j four different resonance relations:

$$\omega_k = \pm\omega_\alpha \pm \omega_{K_i} \pm \omega_{K_j}, \tag{4.19}$$

(with uncorrelated $\pm$), while the x integration gives four different momentum relations:

$$k = k_\alpha + \eta_1 K_i + \eta_2 K_j, \tag{4.20}$$

where $\eta_{1,2} = \pm 1$.

These two relations describe energy-momentum conservation in scattering processes involving a single 4-point vertex, the interaction (4.14b). Only $2 \to 2$ processes involving this vertex can conserve energy and momentum. Furthermore, in $1+1$ dimensions (since all particles have the same mass) it follows that the pair of incoming momenta must be equal to the pair of outgoing momenta. From the energy relation (4.19) it then follows there are three possible diagrams, drawn in Figure 4.11, creating a g_α particle with momentum k. The momentum relation (4.20) now gives us three possibilities,

$$k = \eta_2 K_j \qquad k_\alpha = -\eta_1 K_i \tag{4.21a}$$

$$k = \eta_1 K_i \qquad k_\alpha = -\eta_2 K_j \tag{4.21b}$$

$$k = k_\alpha \qquad \eta_1 K_i = -\eta_2 K_j \tag{4.21c}$$

For the last possibility $k = k_\alpha$, the contribution of the $\phi(x)^2$ term is just a constant. These terms only give rise to a time-dependent mass shift between the modes and mean field. We can conclude that, to leading order, the only excited modes are given by

$$g_{\pm K_i, \pm K_j}. \tag{4.22}$$

Note that only if just one mean field mode is exited (i.e. if $i_{max} = 1$) the modes will remain diagonal.

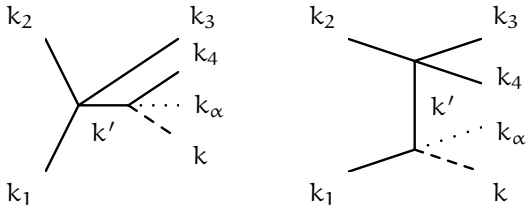

Figure 4.12: Leading $2 \to 4$ scattering diagrams creating a g_α particle in the symmetric phase. The intermediate line represents the retarded Green function.

We will now look at the neglected terms. The renormalized mode-sum $C_{\rm ren}(x)$ is equal to

$$C_{\rm ren}(x) = \sum_\alpha \left({f^0_\alpha}^*(x) g_\alpha(x) + f^0_\alpha(x) g^*_\alpha(x) + |g_\alpha(x)|^2 \right) \tag{4.23}$$

As we just showed, in lowest order, g_α is only nonzero for $k_\alpha \in \{K_i\}$ and therefore the only nonzero Fourier components of $C_{\rm ren}(x)$ are the same as those in $\phi(x)^2$: $k = \pm K_i \pm K_j$. Therefore, including the first order result for $C_{\rm ren}(x)$ in equation (4.17) will not change the set of excited modes. Finally, taking into account the last term in (4.17), using the first order result (4.22), we can also find its contribution. The x integration gives a $\delta_{k',k\pm K_i\pm K_j}$. The frequencies of the correction to g_α are therefore of the form $\omega_{k\pm K_i\pm K_j}$ and we still find exactly the same relation as followed from (4.19) and (4.20).

The above treatment can be extended by making a systematic expansion in λ,

$$\phi = \phi_0 + \lambda\phi_1 + \lambda^2\phi_2 + \cdots, \qquad f_\alpha = f^0_\alpha + \lambda f^1_\alpha + \lambda^2 f^2_\alpha + \cdots, \tag{4.24}$$

and using Green function techniques along the lines of Ref. [22].

As a check we performed a simulation, exciting only two modes K_1 and K_2 at low energy ($E/Lm^2 = 0.04$) and small coupling ($\lambda/m^2 = 1/12$). The assumption of a free oscillating mean field turned out to be extremely good. We also checked the explicit form of one of the modes by examining $|f_{K_1}|^2$. We expect f to contain the two Fourier modes K_1 and K_2, and therefore $|f|^2$ to contain momenta $2K_1$, $2K_2$, $K_1 + K_2$ and $K_1 - K_2$. These were indeed the only modes found. In similar simulations at higher energy we found the back-reaction to ϕ to become more important,however the set of excited modes remained the same.

4.3.2 HIGHER ORDER SCATTERING

In order for the system to thermalize it is necessary that particles can change their momenta by scattering. As mentioned above, $2 \to 2$ scattering cannot change the

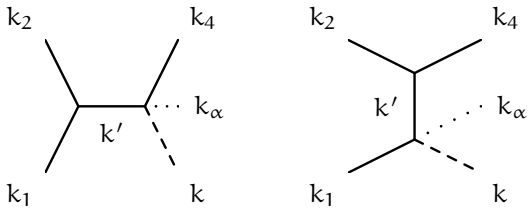

Figure 4.13: Leading $2 \to 3$ scattering diagrams creating a g^k_α particle in the broken phase.

initial momenta in 1+1 dimensions (with re-summed off shell propagators this restriction does not apply, cf. the thermalization found in Ref. [54]). Therefore at least one extra vertex is needed. In the symmetric phase only four-point vertices exist, as in (4.14). The interaction (4.14b) is leading over (4.14c) and (4.14d), because it is first order in g_α. Furthermore initially all energy is in the mean field and the leading contribution to g-particle production comes from the two diagrams in Figure 4.12.

At this point it is interesting to realise what happens if the mean field is homogeneous. In that case g_α always carries momentum k_α ($K_i = 0,\ \forall i$). For inhomogeneous systems this restriction is lifted and thermalization becomes possible.

In the broken phase both the couplings (4.14) and (4.15) contribute and there are three- and four-point interactions. The leading contribution to g-particle production in this case comes from the two diagrams in Figure 4.13. Intuitively one expects the finite range of the interaction in the broken phase, due to off-shell particle exchange, to lead to more efficient thermalization than the zero range interaction in the symmetric phase. This is indeed what we observed.

4.3.3 SCATTERING OF TWO WAVE PACKETS

We end this section by shortly coming back to the possibility of indirect scattering in the Hartree approximation. Consider an initial two-particle state described by wave packets $\psi_{1,2}$:

$$|\psi_1\psi_2\rangle = \hat{b}^\dagger[\psi_1]\hat{b}^\dagger[\psi_2]|0\rangle, \qquad \hat{b}^\dagger[\psi] = \sum_{\mathbf{k}} \psi_{\mathbf{k}} \hat{b}^\dagger_{\mathbf{k}}. \tag{4.25}$$

Then

$$C_{\text{ren}}(\mathbf{x}, t; \mathbf{x}, t) = |\psi_1(\mathbf{x}, t)|^2 + |\psi_2(\mathbf{x}, t)|^2 \tag{4.26}$$

with

$$\psi(\mathbf{x}, t) = \sum_{\mathbf{k}} \psi^*_{\mathbf{k}} f_{\mathbf{k}}(\mathbf{x}, t). \tag{4.27}$$

If we now linearize the Hartree equations in the "broken phase", writing $\phi = v + \phi'$, keeping terms linear in ϕ', while treating $|\psi|^2$ as being of the same order as ϕ', gives

$$(\partial_t^2 - \Delta + m^2)\phi' = -3\lambda\left(|\psi_1|^2 + |\psi_2|^2\right) \tag{4.28a}$$

$$(\partial_t^2 - \Delta + m^2 + 6\lambda v\phi')\psi_{1,2} = 0. \tag{4.28b}$$

If the wave packets approach each other within a distance of order $1/m$ they will scatter.

So the interaction of the quantum modes with the classical modes of the inhomogeneous mean field does lead to indirect scattering. Note that in the symmetric phase $v = 0$ and the back-reaction of the mean field disturbance ϕ' to the particle waves $\psi_{1,2}$ is suppressed.

4.4 DISCUSSION

We will start this discussion with a summary of the behaviour at high and low energy density. This appears to be the distinguishing criterion for the thermalization behaviour of the Hartree approximation for inhomogeneous systems, rather than, for example, an initial state being pure, as for the Gaussian wave packet, or mixed, as for the flat ensemble.

At high energy density $E/Lm^2 \gg 1$, we see that the distribution n_k acquires features of a thermal quantum, i.e. Bose-Einstein distribution. There is a time- and coupling-dependent chemical potential, of order unity in mass units. The temperature is roughly proportional to $\sqrt{E/L}$ and independent of the coupling. The coupling determines the time scale on which the approximate thermalization becomes visible. The initial rapid exchange of energy between modes and mean field occurs on a time scale described by (4.7). The quasi-particle picture is reasonable, although there is a curious mismatch between the total energy as derived from the effective Hamiltonian and that obtained from the quasi-particles, equations (2.22) and (2.60).

After a very long time the energy flows back into the mean field, which is accompanied by the emergence of a power-law distribution for n_k as a function of momentum k. Such power-law behaviour has not been found in the broken phase, and also classical simulations do not show such a behaviour, indicating that the back reaction of the modes plays an essential role. It is interesting to note that Boyanovsky et al. [55] also found power-law behaviour for the occupation numbers, although it is unclear if the same mechanism is behind their finding. In their study of a $3+1$ dimensional $O(N)$ model in the large N approximation, the power-law is caused by a nonlinear resonance of the back reaction of the modes on themselves, with terms of the form $1/(\omega_k - m)$, diverging as $1/k^2$ in the limit $k \to 0$. This

would give a $1/k^4$ behaviour for the particle number, different from what is found here. Furthermore, we only find power-law behaviour in the total- and mean-field-particle numbers, but not in that of the modes. The difference in power and the absence of power-law behaviour in the modes makes it improbable that the physical mechanism behind the resonances is the same.

In a very recent article [56], Micha and Tkachev obtained a particle distribution, falling off as $1/k^s$. In their simulations, the phenomenon is caused by turbulance. The power s has a value in the range $1.5 - 1.7$, for the $3 + 1$ dimensions they use, precisely what we find for the mean field distribution. However, their system is different from ours in several important ways and we are as yet unable to say if our finding can be explained by the same turbulance phenomenon.

At low energy density $E/Lm^2 \ll 1$, for the flat ensemble as well as for the pure-state wave packet, we do not find approximate thermalization to a BE distribution. Instead, the form of the total distribution n_k remains the same for times that are many tens of thousands in units of m^{-1}. The distribution then slowly turns over into a classical distribution. However, there is still an extensive exchange of energy between the mean field and the modes, leading to what we call local k-space equilibration. At low energy, the time scale for this process is much longer than would follow from (4.7), found at high energy densities. Furthermore, at short times the energy densities in the mean field and modes separately show a remarkable oscillatory behaviour, not seen at higher energies, which is caused by a difference in the effective mass of the mean field and modes.

We obtained several time scales: for approximate Bose-Einstein thermalization, for the early-time exchange of energy between mean field and modes, for the auto-correlation function and for the evolution to a classical distribution. Most of these are much longer in the symmetric phase than in the broken phase:

• In the previous chapters, we found the BE-thermalization-time scale in the broken phase is of the order $25 - 35$ for $E/Lm^2 = 0.5$, while here, in the symmetric phase, $m\tau_{BE} = 1500 - 1600$ for $E/Lm^2 = 4$ (both at $\lambda/|\mu^2_{ren}| = 1/6$).

• The energy-exchange time scale in the broken phase gives a result that is close to τ_{BE}, whereas in the symmetric phase it is related to local k-space equilibration, much shorter than τ_{BE}, and it shows the behaviour (4.7). For $E/Lm^2 = 0.5$ and $\lambda/|\mu^2_{ren}| = 1/6$, Eq. (4.7) gives $\tau m \approx 300$, much longer than the $25 - 40$ we found in the broken phase at the same energy and coupling,

• Also the damping time, obtained from auto-correlation functions is much longer than in the broken phase, even at much higher energy and larger coupling. Compared to the value obtained using classical dynamics, it is roughly twice as large. In the broken phase, both values are comparable in size. At low energies the damping time seems to be much longer, but this needs more study.

• The last time scale is that of classical equilibration. Since we are just solving a

large number $(2N^2+1)$ of local classical non-linear equations, one may expect classical equipartition to set in at some point. This equipartition is, however, non-trivial because of the large number of conserved charges (2.27). For example, the emerging classical temperature is of order E/N and not E/N^2 (recall that for N spatial lattice sites there are $2N^2$ real degrees of freedom in the mode functions). Depending on energy and coupling we can already see a first emergence of classicality at times $\tau m = \mathcal{O}(10^4)$. This is still about an order of magnitude longer than what was found in the broken phase in Chapter3. However, full classical equilibrium is expected only for huge times, much larger than the $\tau m = \mathcal{O}(10^6)$ found in the broken phase for an artificially small system at $E/lm^2 = 36$, Fig. 2.10, and beyond the already large times of order 10^5 reached in this study.

Remarkably, the equilibration time scale found in [18] using classical dynamics appears to be *shorter*. The empirical formula [18]

$$\frac{1}{m\tau_{\text{class}}} = 5.8\ 10^{-6} \left(\frac{6\lambda T}{m^3}\right)^{1.39}, \tag{4.29}$$

with $T = E/N$ the classical equilibrium temperature, would give equilibration times $tm = \mathcal{O}(10^5)$ – $\mathcal{O}(10^7)$ for the various parameters used here. This difference, in equilibration time scales, can be interpreted as follows. Classical dynamics has also been studied in the Hartree approximation, the latter then shows up as an unstable fixed point of the full dynamics [18]. This Hartree fixed point depends on the initial conditions. In our case the mode functions are initialised with quantum-vacuum form (2.29b), and the resulting dynamics (seen as a classical system with order N^2 fields) appears to linger for a very long time near a Hartree fixed point, longer than when using classical dynamics.

For our inhomogeneous initial conditions we have not been able to pin down the fixed point analytically, but intuitively one may expect the system to be close to it when the mean field has lost most of its energy and has started fluctuating about a homogeneous average. Making a homogeneous approximation to this situation would lead to a Hartree stationary state. Such a state can have an arbitrary particle distribution n_k, which, given our out-of-equilibrium initial conditions, turns out to have BE features when the energy density $E/Lm^2 \gg 1$. Apparently, when the energy density is small, $E/Lm^2 \ll 1$, the system leaves the fixed-point region before BE-like thermalization sets in, because we have seen only classical-like equilibration emerging in this case.

Finally, we comment on the results of Bettencourt et al. [52]. As mentioned in Sect. 4.2.2, we have essentially confirmed their numerical results. The energy density in the simulations in [52] was rather low, namely $E/Lm^2 = 0.00042$ and 0.0045, so in view of our results summarised above, no sign of a BE distribution is to be expected with the Hartree approximation at the times $tm \lesssim 200$ covered in

[52], nor at any time later.

It is remarkable that at larger energies $E/Lm^2 \gg 1$ we do find Bose-Einstein behaviour, but of course, the fact remains that the Hartree approximation needs to be improved in order to achieve thermalization at all energies. This may take huge times at low energy densities.

It has been remarked [52] that the Hartree approximation is expected to be valid up to times $tm \sim m^2/\lambda = \mathcal{O}(10)$. We agree with this statement when applied to the detailed time-evolution of observables, but it does not necessarily apply to observables such as our quasi-particle distribution $n_k(t)$ or energy $\omega_k(t)$, that are coarse-grained in time and space and/or averaged over initial conditions in the Hartree ensemble approximation. For comparison, consider a gas of classical point particles with Lennard-Jones interactions. Any numerical approximation to the detailed time evolution will soon go dismally wrong due to the chaotic nature of the system, but this does not preclude an accurate evaluation of, say, a coarse-grained particle-distribution function. With this in mind we have studied our system for times as large as seemed necessary, which led to very large times indeed. First experience [57] indicates that the situation is not very different in 3+1 dimensions, where also large equilibration times may be expected for the ϕ^4 model at moderate couplings and energy densities.

4.A CALCULATION OF THE PARTICLE NUMBER OF THE GAUSSIAN WAVE-PACKET

We calculate here the initial two-point functions for the Gaussian wave packet initial condition (4.3), the corresponding particle number n_k and energy ω_k, and their subsequent free field expressions. The calculations will be made in the continuum limit, in a finite periodic volume.

The mean field contributions to the two-point functions are given by

$$S(x,y)^{mf} = \overline{\phi(x)\phi(y)} - \overline{\phi(x)}\ \overline{\phi(y)}, \tag{4.30a}$$

$$U(x,y)^{mf} = \overline{\pi(x)\pi(y)} - \overline{\pi(x)}\ \overline{\pi(y)}, \tag{4.30b}$$

where we shall average, at first, only over space, e.g.

$$\overline{\phi(x)\phi(y)} = \frac{1}{L}\int_0^L dz\, \phi(x+z)\phi(y+z). \tag{4.31}$$

The initial mean field is given by (4.3), or in terms of its Fourier transform:

$$\phi_k = \int dx\, e^{-ikx}\phi(x) = \Phi\sqrt{2\pi A}\ e^{-k^2A/2}. \tag{4.32}$$

Since $\pi(0) = 0$, the free-field (i.e. for $\lambda \to 0$ and $\mu \to \mu_{\rm ren} = m$) evolution of ϕ_k in time is given by:

$$\phi_k(t) = \phi_k(0)\cos(\omega_k^{(0)} t), \tag{4.33}$$

where $\omega_k^{(0)} = \sqrt{m^2 + k^2}$. A straightforward calculation gives

$$S_k^{\rm mf} = \Big(1 - \delta_{k,0}\Big)\frac{\phi_k^2 \cos^2(\omega_k^{(0)} t)}{L}, \tag{4.34a}$$

$$U_k^{\rm mf} = \Big(1 - \delta_{k,0}\Big)\frac{(\omega_k^{(0)})^2 \phi_k^2 \sin^2(\omega_k^{(0)} t)}{L}, \tag{4.34b}$$

where the delta functions come from the disconnected pieces. The modes just contribute the vacuum fluctuations:

$$S_k^{\rm modes} = \frac{1}{2\omega_k^{(0)}}, \qquad U_k^{\rm modes} = \frac{\omega_k^{(0)}}{2}. \tag{4.35}$$

Adding the contributions in (4.34) and (4.35) and applying the definition (2.56), the initial instantaneous particle number and frequency become

$$n_k(0) = \frac{1}{2}\left(\sqrt{2\omega_k^{(0)}\phi_k^2/L + 1} - 1\right), \tag{4.36a}$$

$$\omega_k(0) = \frac{\omega_k^{(0)}}{\sqrt{2\omega_k^{(0)}\phi_k^2/L + 1}}. \tag{4.36b}$$

Using free field dynamics the instantaneous particle number would get an oscillating component according to (4.34). If, apart from the volume average, we also course-grain in time, the disconnected parts of S and U vanish, while both $\cos^2$ and $\sin^2 \to 1/2$. We then find

$$n_k^{\rm free} = \frac{\omega_k^{(0)}\phi_k^2}{2L}, 1 \qquad \omega_k^{\rm free} = \omega_k^{(0)}, \tag{4.37}$$

which are time-independent.

For large volumes $2\omega_k^{(0)}\phi_k^2/L \ll 1$, expressions (4.36a) and (4.36b) reduce to (4.37). For the parameters as used in Section 4.2, $A = 2$, $\Phi = 2.60106$, $Lm = 32$, we find

$$\frac{2\omega_k^{(0)}\phi_k^2}{L} \approx 5.3\sqrt{1 + k^2/m^2}\, e^{-2k^2/m^2}. \tag{4.38}$$

By plotting $n_k(0)$ (or $\log[1+1/n_k(0)]$) versus $\omega_k(0)$ we find that this only compares well with a similar plot of $n_k^{\rm free}$ versus $\omega_k^{\rm free}$ for $k \gtrsim 2m$. So at times $tm \gg 1$ it is best to use the time-averaged free-field determinations for the comparison with the interacting Hartree evolution.

CHAPTER 5

KINKS

In the mid-nineteenseventies an extensive number of nontrivial classical solutions to nonlinear wave equations were found. Their localization in space is an important aspect of these classical solutions. Furthermore, in this classical theory, they are often (absolutely) stable as a result of the topology of space, it takes an infinite amount of energy to remove them. Because of their localised character they are referred to as solitons.

The ϕ^4 theory, in the broken phase, also contains solitons, the so-called kink.[1]. In an infinite volume, the field necessarily has to be in one of the two minima for $x \to \pm\infty$, in order to keep the total energy finite. It still leaves two separate sets of solutions: the field is in the same minimum in both limits, or it is in the two different minima. The latter "sector" corresponds to the kink or antikink solution. The field configuration needs to cross the potential barrier at some point in space, but the exact position doesn't influence the energy. An infinite set of degenerate solutions exists, only differing in the point where they go over the barrier.

An excellent introduction on the topic can be found in Ref. [58]. In this final chapter we will discuss kinks (and antikinks) in the Hartree approximation, comparing the results with the classical theory.

5.1 CLASSICAL KINK SOLUTIONS

It is possible to calculate the lowest non-trivial solution using a very elegant and general method, the Bogomol'nyi equation[59]. In the broken phase the classical

[1] According to the strict definition of Ref. [58], the ϕ^4 defects should be called solitary waves, since they cannot pass each other, they can only bounce

static Hamiltonian (energy) is given by

$$\begin{aligned} E &= \int dx\, \frac{1}{2}(\phi')^2 + \frac{\lambda}{4}\left(\phi^2 - v^2\right)^2 \\ &= \int dx\, \frac{1}{2}\left(\phi' \pm \sqrt{\frac{\lambda}{2}}(\phi^2 - v^2)\right)^2 \mp \phi'\sqrt{\frac{\lambda}{2}}(\phi^2 - v^2) \\ &= \int dx\, \frac{1}{2}\left(\phi' \pm \sqrt{\frac{\lambda}{2}}(\phi^2 - v^2)\right)^2 \mp \left[\sqrt{\frac{\lambda}{2}}(\frac{1}{3}\phi^3 - v^2\phi)\right|_{\phi(-\infty)}^{\phi(\infty)}, \end{aligned} \tag{5.1}$$

where $\phi' = \partial_x \phi$. The boundary term is equal to a finite constant and determines the topological sector, trivial or nontrivial. For given boundaries the energy is therefore bounded from below by the first term which is larger than or equal to zero, the so-called Bogomol'nyi bound. The lowest energy state can be found by solving the simple first order differential equation

$$\phi' = \mp\sqrt{\frac{\lambda}{2}}(\phi^2 - v^2), \tag{5.2}$$

which has solutions

$$\phi = \begin{cases} \pm v \tanh\left[\frac{m}{2}(x - x_0)\right] \\ \pm v \end{cases} \tag{5.3}$$

Here x_0 is the point where ϕ goes through 0 and $m = \sqrt{2\lambda v^2}$ is the mass in the broken vacuum. In the top line, the $+$ solution corresponds to a kink, the $-$ solution to an antikink. The width of the kink is inversely proportional to the mass.

The kink energy density can be found from (5.1) using (5.2)

$$e_{\text{kink}} = \frac{\lambda}{2}(\phi^2 - v^2)^2 = \frac{1}{2}\lambda v^4 \left(\tanh^2\left[\frac{m}{2}(x - x_0)\right] - 1\right)^2. \tag{5.4}$$

Both the solution (5.3) and the energy density (5.4) are plotted in Fig. 5.1.

The kink mass, defined as the energy of the static kink or antikink, can be found either by integrating (5.4) or directly, from the boundary term in (5.1)

$$M_{\text{kink}} = \frac{2}{3}\sqrt{2\lambda}v^3 = \frac{2}{3}mv^2 = \frac{m^3}{3\lambda}. \tag{5.5}$$

Note that it diverges in the limit $\lambda \to 0$, showing the non-perturbative nature of the configuration.

From the static kink solution (5.3) we can easily find a moving kink solution by a Lorentz transformation:

$$\phi(x,t) = v \tanh\left[\gamma\frac{m}{2}(x - x_0 - ut)\right], \tag{5.6}$$

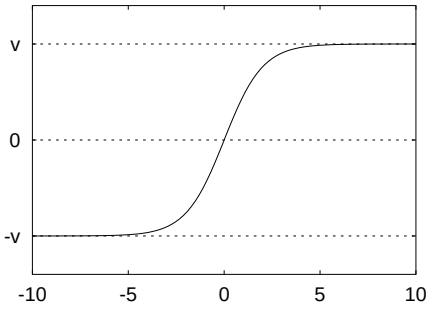

a: Classical kink solution at $x_0 = 0$

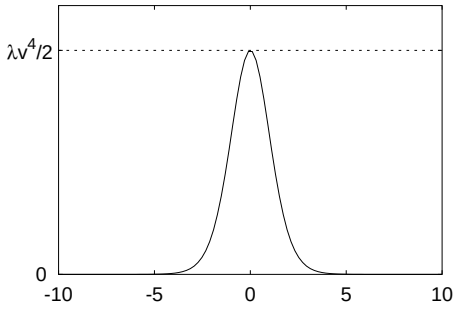

b: Energy density of the solution in 5.1a

Figure 5.1: Classical kink solution (5.3) and its energy density (5.4) as a function of x, spatial distance, in units m^{-1}.

where $\gamma = 1/\sqrt{1-u^2}$. Note that this is not a solution of the Bogomol'nyi equation (5.2), since it is not static. However it is a solution to the manifestly Lorentz covariant field equations. The total energy of this moving solution is equal to $E_{kink} = \gamma M_{kink}$, as expected for a relativistic particle. A Lorentz boost therefore has the effect of increasing the kink mass while decreasing its width. Since we do not change the total volume and the separation between the kink and antikink in the rest frame, while their width becomes smaller, the relative distance in the comoving frame becomes larger and we therefore expect the pair to become much more stable.

We end this section by mentioning some consequences of the use of a finite volume. The sector is determined by the kind of boundary conditions: using periodic boundary conditions there is no net kink number. A kink-antikink pair can be considered. Although it is inherently unstable, the survival time depends heavily on the volume, as a result of the exponential attraction between them. When using anti-periodic boundary conditions, the kink number is ± 1. By shifting the kink over 1 lattice size L through the boundary, the kink number changes sign, i.e. only its absolute value is conserved.

Another unwanted side effect of the use of a (anti)periodic lattice is radiation, resulting from discretization errors, which interferes with the kink-antikink themselves. Some solutions have been proposed, see for example Gleiser and Sornborger [60] and Speight and Ward [61, 62, 63]. In Ref [60] a damping method is used to remove the radiation before it can interfere. Speight and Ward propose a lattice discretization preserving the Bogomol'nyi bound, thereby also removing the

radiation resulting from the discretization.

However, according to Ref. [64] this solution is only suitable for free kinks. In dynamical systems a standard discretization would be simpler and has the same accuracy. We will not bother too much about this issue. If we want to accurately follow an approaching pair during a long time, large lattices will be used and the kink and antikink will be put close together initially: the radiation is mainly emitted backwards and reenters via the periodic boundary condition. By putting them close together it then takes a long time for the radiation to reach the soliton pair.

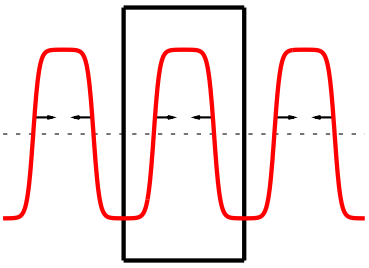

Figure 5.2: Kink-antikink initialisation procedure.

Finally, the use of (anti)periodic boundary conditions in a finite volume introduces a small mismatch in the derivative of the field at the edges, especially if the kink and antikink are close. We therefore use the setup drawn in Figure 5.2: we take several configurations in several adjacent volumes and use the resulting configuration in one of them:

$$\phi_{K\overline{K}}(x,t)\Big|_{t=0,a_0} = -v + v\sum_{n=-N}^{N}\Big\{\tanh\Big[\gamma\frac{m}{2}(x+[x_0-ut]+n\cdot L)\Big] - \tanh\Big[\gamma\frac{m}{2}(x-[x_0-ut]+n\cdot L)\Big]\Big\}, \tag{5.7}$$

where N is typically around 8.

5.2 HARTREE KINKS AT REST

Although interesting in itself the classical theory is not the full story and it is therefore important to study quantized kink solutions. In order to study dynamical processes, like collisions, one has to use approximation schemes, which are non-perturbative, real-time and which can handle inhomogeneous configurations. For this purpose the inhomogeneous Hartree approximation as studied in Chapters 2 and 3 should be particularly appropriate, being a non-perturbative semi-classical approximation scheme.

5.2.1 INITIAL CONDITION

Unlike in the classical theory, we cannot use the Bogomol'nyi argument to derive a static soliton solution to the Hartree equations (2.18). However, if the coupling is not too large, or more precisely, if the two vacua are well separated and the barrier between them is high, the quantum corrections will be relatively small. Furthermore, away from the physical position of the kink, the field resides in one of the vacua and an exact solution of the Hartree equations is known. Therefore using the classical kink solution as initial condition for the mean field, while using the free field plane wave solutions for the mode functions will be close to a Hartree kink solution. After the configuration has evolved from such an initial condition using the Hartree equations of motion, it will, at least for a while, oscillate around the actual stationary solution, provided that the vacuum expectation value v is (substantially) larger than 1.

A way to improve on this initial condition is to add a damping term $-\Gamma\partial_t\phi$ to the mean field equation (2.5)[2] and evolve from the aforementioned initial condition to obtain an approximately stationary solution, which can then be used as a new initial condition. We will discuss this setup further in Section 5.3, when considering colliding kinks.

The numerical results presented in the next subsection are all obtained using the simple initial condition, with mode functions of free field form and equation (5.7) for the mean field.

5.2.2 NUMERICAL RESULTS: STATIC KINK DECAY

Here results are presented for the evolution of a kink-antikink configuration, initially at rest at a maximum distance in the periodic volume. A comparison will be made, between Hartree and classical dynamics, using identical initial conditions, in the sense that the mean field in the Hartree simulation is equal to the field in the classical simulation. Hartree simulations at small and large coupling will also be compared. In this case the same physical volume will be used. Finally the effect of damping on the lifetime of the kink-antikink pair is discussed. The combined results are shown in Figure 5.3, in the form of contour plots of the energy-density for the four different simulations. Figure 5.3a shows a classical simulation at $\lambda/m^2 = 1.25$, Figure 5.3b shows the same simulation, using Hartree dynamics, Figure 5.3c shows the same Hartree simulation, with a damping $\Gamma = 0.4m$ switched on while $tm \leq 15$. Finally Figure 5.3d shows the result for a Hartree simulation at a weaker coupling $\lambda/m^2 = 1/12$, without a damping term in the equations of motion. We have plotted a contour plot of the (total) energy-density, as it shows the position of the kink more clearly than the mean field.

[2]Note that it is not possible to do this at the level of the action or Hamiltonian.

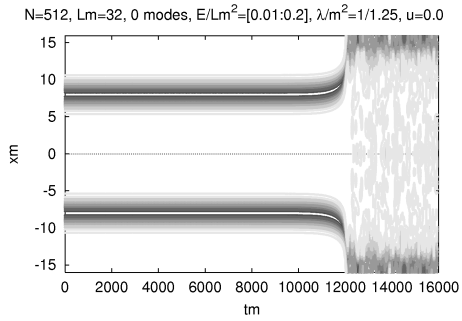

a: Classical, $\lambda/m^2 = 1/1.25$.

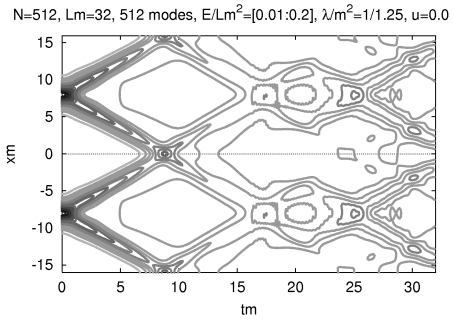

b: Hartree, $\lambda/m^2 = 1/1.25$.

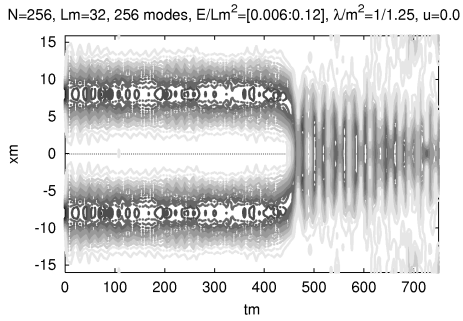

c: Hartree, $\lambda/m^2 = 1/1.25$, with damping $\Gamma = 0.4m$ till $tm = 15$. Plot energy in mean field.

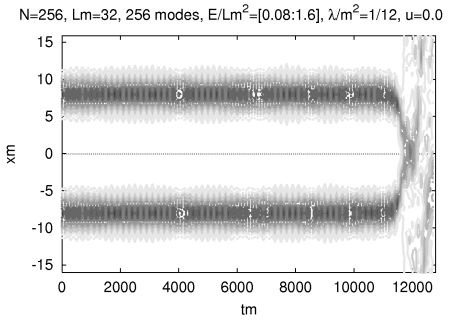

d: Hartree, $\lambda/m^2 = 1/12$.

Figure 5.3: Energy density contour plot for kink-antikink annihilation from rest, for different couplings, classical and Hartree. All plots, except 5.3c, show total energy density.

Figures 5.3a and 5.3b, showing the results for two identical initial conditions, using classical and Hartree dynamics respectively, indicate there is an enormous difference in annihilation time, mainly caused by the fact that the initial form of the Hartree pair is only approximately stationary, as explained in the introduction of this chapter. For such a large coupling the barrier is low, and the mode functions for a stationary Hartree solution are very different from the plane wave form.

It is important to mention that, although it seems from Figure 5.3b that the (anti)kink splits into two (anti)kinks, this is not actually the case. The mean field just "contracts" over the barrier, thereby annihilating both kink and antikink. In this process some energy is send off in opposite directions, but this cannot be seen as kink-antikink pairs. This was checked explicitly by making animations of the mean field.

By comparing the results in Figures 5.3b and 5.3c we see that the difference in survival time between classical and Hartree does indeed partially come from the approximately stationary Hartree initial condition: after the damping is switched off at $tm = 15$, the kink-antikink pair survives till $tm \approx 450$. Switching off the damping at a later instant increases the surviving time: using $tm = 40$ instead of $tm = 15$ results in a surviving time of $tm \approx 500$, i.e. the surviving time increases by 50 due to an increase in "switch-off" time of 25. When we do not switch off the damping, the pair survives till at least $tm = 2000$. We haven't simulated this system for longer, but we do not expect it will ever decay.

We checked the influence of the precise value of the damping constant, by also simulating at $\Gamma = 0.2m$ and $\Gamma = 0.8m$. At the smaller value of $\Gamma = 0.2m$, the pair survived during a slightly shorter time-interval $\Delta tm = 20$, at a larger damping of $\Gamma = 0.8m$ the difference is only $\Delta tm = 2$. From this we derive, that using a damping constant $\Gamma = 0.2m$ during a time $tm = 15$ already removes almost all of the fluctuations around the stationary configuration. However the remaining configuration is still much less stable than its classical counterpart. This is further supported by a comparison of the total energy-density with the depicted mean field energy density: it turns out that the total energy density is much smoother, apparently the modes in part cancel out the kink-antikink inhomogeneities, which probably also facilitates the final annihilation of the pair.

Since there is still oscillatory motion in the configuration left after the damping, it would be desirable to keep the damping in effect. However, we found it also has a very long-time effect on the energy-density. Using $\Gamma = 0.4m$ the energy very slowly decreases with a time scale of the order 200. This time scale depends on the volume, so it seems to be a finite volume artifact, however we do not understand the physical process behind it, it impels us not to damp the equations longer than $tm \approx 15$. Until that time, we see a clear damping in the total energy density, with a rate corresponding to the damping term in the mean field equation. After this time

$tm \approx 15$, the energy density seems constant for a while, even when the equations are damped, but after this short time, the large time scale damping sets in. We will shortly come back to this in the next subsection, when discussing the quantum kink mass.

Finally, comparing Figure 5.3b at $\lambda/m^2 = 1/1.25$ with Figure 5.3d, we see that using the classical kink form for the mean field and plane waves for the modes at the weaker coupling, is much closer to a stationary solution, even without damping. The configuration is oscillating around an approximately stable solution for a extensive period of time, before annihilation. By comparing Figures 5.3d and 5.3c we find the width of the kink is smaller at the smaller coupling, due to a change in the effective potential caused by the quantum modes. Classically the width only depends on the mass m, which by construction is the same for both couplings. This change of width also explains why at larger coupling, the kink-antikink configuration is less stable: relative to their own size, they are closer to each other. Increasing the volume (and thereby also the initial distance between the kinks) thus also increases the surviving time enormously, as already mentioned above.

5.2.3 NUMERICAL RESULTS: KINK MASS

Classically the kink mass is given by equation (5.5). In the full theory this expression needs corrections. The first corrections were found by Dashen et al.[65], see also Rajaraman [58],[3] and more recently by Alonso Izquierdo et al.[66]. The result is obtained using a semi-classical perturbative expansion around the classical kink solution. The kink mass is then given by the lowest energy level. This mass has to be renormalized and the net result is:

$$M_{\text{kink}} = \frac{m^3}{3\lambda} + m\Big(\frac{\sqrt{3}}{12} - \frac{3}{2\pi}\Big) + \mathcal{O}(\lambda). \tag{5.8}$$

A partial calculation of the order λ correction can be found in Ref. [67]. In this reference and independently also in Ref. [68] a full calculation is done for the kink mass in the sine-Gordon model.

More recently lattice Monte Carlo studies of the kink mass have been carried out [69, 70]. In these papers two methods of calculating the kink mass were used: first using the fluctuation-fluctuation two-point function $\langle \mu(t)\mu(0)\rangle$ introduced in [71, 72], which in imaginary time should decay as $\exp(-M_K t)$. The second uses the difference in the ground state energy when periodic or anti-periodic boundary conditions are used. Both studies focus on a range of parameters, where λa^2 and

[3]Note that there are two errors in [58]: In equation (5.69) $\sqrt{p^2+1}(p^2+4)$, in the numerator of the first term in the integral, should be $(p^2+1)\sqrt{p^2+4}$ and $\sqrt{p^2+2}$ in the numerator of the second term in the integral should be $\sqrt{p^2+4}$. This second error comes from the transition of $2k^2 \to p^2$.

$-\mu_0^2 a^2$ are of order unity, i.e. at large lattice distances.[4] For most of our simulations, $\lambda a^2 = 1/(12 \cdot 8^2) = \mathcal{O}(10^{-3})$. In Ref. [70] it is found that at low values of $-\mu_0^2 a^2$, the Monte Carlo value lies between the semi-classical and classical regime while at larger values it lies below both of them. Using our parameters the semi-classical correction will therefore be too large, compared to the Monte Carlo value.

It is interesting to compare the results in the Hartree approximation with the semi-classical result from Ref. [65]. We have done this in simulations at weak coupling $\lambda/m^2 = 1/12$ and at strong coupling $\lambda/m^2 = 1/1.25$, also discussed in Subsection 5.2.2. We found that the Hartree approximation actually does better than the semi-classical approximation: the kink mass lies between the classical and the semi-classical value, closer to the exact (Monte Carlo) value.

For the stronger coupling $\lambda/m^2 = 1/1.25$, the order λ^0 correction is larger than the leading λ^{-1} term, and expression (5.8) gives a negative result. The Hartree approximation, using damped equations of motion and anti-periodic boundary conditions, gives a kink mass of about 75–80% of the classical kink mass, again better than the semi-classical approximation. At the weak coupling $\lambda/m^2 = 1/12$, the semi-classical result is $M_{\text{kink}} = 3.67$, i.e. 92% of the classical kink mass 4, while we find $M_{\text{kink}} \approx 3.8$, 95% of the classical value. In both cases the Hartree result lies between the semi-classical and the classical value and is closer to the Monte Carlo than the semi-classical results.

At the strong coupling we used a volume of $Lm = 32$ and a lattice distance $am = 1/8$, with different damping coefficients, $\Gamma/m = 0.2, 0.4, 0.8$. All three values give approximately the same result. At the weaker coupling, we only used one damping coefficient $\Gamma/m = 0.4$, but different lattice sizes, $Lm = 8, 16, 32, 64$ at a fixed lattice distance $am = 1/8$ and different lattice distances $am = 1/4, 1/8, 1/16$ at a fixed lattice size $Lm = 32$. The dependence on these both of these parameters is small and convergent.

After an initial stage during which the system behaves as one would expected from the damping term, a second stage of very slow damping sets in, during which energy is drained from the mode functions, while the mean field kinetic energy is already nearly zero. The damping rate depends on the volume, not on the lattice distance. We do not understand this stage, and prevent it by switching off the damping term before it sets in. The initial stage can be fitted well to an exponential decay, and it nearly damps out before the second stage sets in, we therefore do not expect to make a large error. Furthermore, we have seen in the previous subsection that damping longer than a certain time, does not further extend the lifetime of the highly unstable strong coupling kink-antikink pair any longer. At the smaller $\Gamma/m = 0.2$ it does lead to a slightly higher value of the total energy density by about 2%, as for this value of Γ the slow rate damping sets in before the initial stage

[4] Note that the horizontal axis, $\hat{\lambda}$, in Fig. 4 of Ref. [70] should be multiplied by 6

is over.

5.3 MOVING HARTREE KINKS

5.3.1 INITIAL CONDITION

In order to describe kink-antikink collisions, it is necessary to have a description of a moving Hartree kink as well. In the full quantum theory this poses a difficult problem, since we do not know how to transform the "quantum cloud" surrounding the kink. In the Hartree approximation we are saved by the fact that the field is completely expressed in terms of ordinary functions of x and t, and we can find a moving kink by performing a simple Lorentz transformation:

$$f(x,t) \to f'(x,t) = f(\gamma[x-ut], \gamma[t-ux]), \tag{5.9}$$

both on the mode functions and the mean field.

However, there are still a number of difficulties with finding a proper initial condition for a kink-antikink pair, moving toward each other. First of all, from equation (5.9) it is clear we need the mode functions on a backwards space-time line, while we do not know them in analytic form, only from a simulation. For the classical kink solution this problem does not exist, since it is not only stationary, but also static and known analytically. Secondly, we have to boost the kink and antikink, with their respective mode-functions, in opposite directions. This means that they have to be combined in a nontrivial way in the middle, they "shift into each other". It also means that we have to double the density of mode functions in k-space, since the physical space doubles. We have to decide how to do this in a consistent way. Finally there is the problem that the coordinates $\gamma(x-ut)$ and $\gamma(t-ux)$ will generally not fall onto space-time lattice points in the unboosted frame.

In order to circumvent these problems, we will just use the vacuum form as initial conditions of the mode functions. Since the vacuum is invariant under Lorentz transformations, we can use the same mode functions in a boosted frame. As mentioned before, the mode functions will be close to the vacuum form, if the vacuum expectation value v is large. By boosting the kink solutions, we reduce the width of the kinks, meaning we effectively increase the relative distance between them, leading to a much more stable solution, which is even further enhanced by the time dilatation.

Before we proceed we will outline a set of solutions for the aforementioned problems, which will yield a very accurate boosted kink-antikink solution and will therefore also be usable at strong coupling and low speeds. In the simulations we will in general only use the vacuum form mode functions.

The way to solve the stability problem of a kink is to use damped equations of motion, as we already used in the previous subsections, especially in combination with anti-periodic boundary conditions on the mean field to make the kink absolutely stable. The damping will give us stationary, but time-dependent solutions for the mode functions in the background of a kink, which subsequently can be Lorentz boosted.

The problem of the boosted coordinates not resulting from discrete lattice points in the unboosted coordinate can be adequately solved by linear interpolation, provided the lattice distance is not too large. The related matching problem is not a real problem: if the two functions approach each other with speed u, they shift into each other over a distance $ua_0 < a$, i.e. the mismatch is less than a lattice distance and the linear interpolation automatically solves the problem.

The remaining problem is combining the two sets of mode functions, of the separate kink and antikink configurations, into one set which is twice as large. One possible solution would be to determine both kink and antikink in a volume that already has the size of the combined configuration and then use an averaging procedure to combine the modes. This has the disadvantage that oscillatory functions with different phases are added. Another way, which we suggest, is to determine the two configurations in their original volume and combine them afterwards into one set. When using periodic mode functions, it follows from the anti-periodicity of the mean field that at all times

$$f_k(x,t) = f_{-k}(L-x,t), \tag{5.10}$$

provided this relation holds at $t = 0$ and $t = a_0$, which is true for the plane wave initial conditions we use. Note that at later times the k label is no longer equal to the Fourier label. We can therefore combine each mode function f_k with either itself or with f_{-k}, since both combinations yield continuous functions. The derivative will in general be discontinuous, possibly causing trouble in the equation of motion, but the energy density will be finite and even continuous.

We end this subsection with a summary of the steps one could follow to obtain a better initial state for a colliding kink antikink pair. First, using anti-periodic boundary conditions for the mean field and a damping term $-\gamma\dot{\phi}$, one evolves the Hartree equations, starting from a classical kink with free field mode functions. One thus obtains a stationary Hartree kink solution. One has to compute the modes and mean field on a backward space-time line. Then one constructs the mean field from the kink and its mirror image. The modes are constructed by combining $f_k(x,t)$

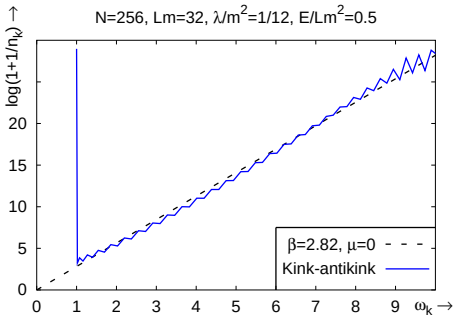

a: $tm = 0$, before the collision

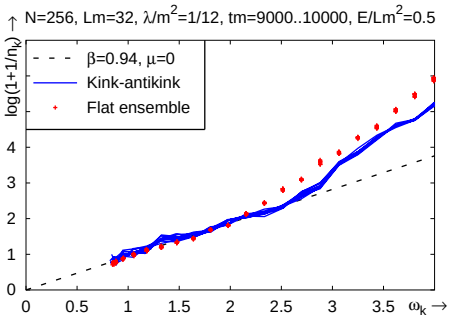

b: $tm \approx 10000$, after annihilation

Figure 5.4: Initial and late time form of the particle distribution for a Hartree kink-antikink collision. The initial form already seems close to a Bose-Einstein distribution.

with itself and with $f_{-k}(x,t) = f_k(L-x,t)$, thereby doubling their number:

$$f_{k,1}(x,t) = \begin{cases} f_k(x,t) & 0 \le x \le L \\ f_k(x-L,t) & L \le x \le 2L \end{cases} \tag{5.11}$$

$$f_{k,2}(x,t) = \begin{cases} f_k(x,t) & 0 \le x \le L \\ f_{-k}(x-L,t) & L \le x \le 2L \end{cases} \tag{5.12}$$

The latter combination can lead to functions in which the second derivative diverges as $1/a$, but the energy density is finite and continuous in the continuum limit. However it might cause problems in the equations of motion.

5.3.2 NUMERICAL RESULTS: THERMALIZATION FROM COLLIDING KINK-ANTIKINKS

We start the discussion of our numerical results with the thermalization properties of a colliding kink-antikink pair, by looking at the defining relation (2.55)–(2.56) for n_k. We simulated a kink-antikink collision in a volume $Lm = 32$ at a speed $\gamma = 2$, i.e. at an initial energy density $E/Lm^2 = 2 \cdot (4+4)/32 = 0.5$. At this energy density we found, in Chapter 2, a temperature $T/m \approx 1.0$, consistent with the effective potential (2.45).

In order to enable us to correctly interpret the result, we also measured the "particle number" at $tm = 0$. Of course at this time the system is so far from equilibrium

that we cannot interpret the result as quasi-particles, but it does give us an idea of the energy distribution as a function of k. The result is plotted in Figure 5.4a. The similarity with a Bose-Einstein distribution is remarkable and we have to be careful in interpreting the results. One of the indications that it is not a truly thermal distribution is its very low "temperature": at an energy density $E/Lm^2 = 0.5$ we expect to find a temperature around $T/m = 1.0$, whilst we found an value which was almost three times smaller. Furthermore, the particle number mainly comes from the even modes, as a result of the symmetric initial condition.

Figure 5.4b shows the actual particle number at later times, when the kink-antikink have already annihilated. At this moment we do find a temperature around 1, conform the results of Chapter 2 and the effective potential (2.45). As a comparison we also plotted the result obtained in that chapter using a flat ensemble simulation, in the same figure. It clearly shows that the temperatures are equal: T is uniquely determined by the coupling and energy, not by the initial condition. The initial condition is still visible in which modes have thermalized, and we see that starting from an annihilating $K\overline{K}$ allows the system to thermalize faster. The reason for this is of course the fact, that this initial condition has a more favourable energy distribution, cf. Fig 5.4a. However the $K\overline{K}$ initial condition has a delta function initial density matrix, which is not very suitable for our Hartree ensemble approximation: we do not reduce the statistical errors by averaging over multiple initial conditions.

Having showed that also this initial condition leads to a thermal Bose-Einstein distribution in the end, we will now leave the thermalization topic and continue with a discussion of the actual collisions.

5.3.3 NUMERICAL RESULTS: CRITICAL SPEED

We start this section with a study of *classical* kink-antikink collisions. An extensive study of this can be found in Reference [73].

Figure 5.5 shows energy contour plots of Lorentz boosted classical kink-antikink configurations. The results in these plots demonstrate that they just annihilate at very low incident speed, while at a certain range of higher speeds, they bounce a few times and then either annihilate or escape again to infinity, with a slightly lower speed. At high enough speeds, when u is larger than a certain u_c, with a value between 0.25 and 0.30, the pair immediately escapes after the collision, again with a lower speed. Part of the kinetic energy is transferred to an internal vibrational mode of the kink, which can be seen as a wiggling in the contour plots.

These results are consistent with Ref. [73] in which a critical speed $u_c = 0.2598$ is found, above which colliding kinks always bounce back, while below a speed 0.193, they always annihilate immediately. Between these speeds they found reflection and annihilation bands, caused by a resonance between the center of mass motion

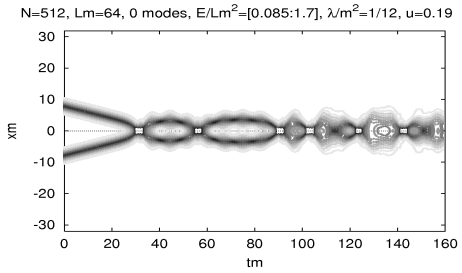

a: $u_i = 0.19$ ($\gamma \approx 1.019$).

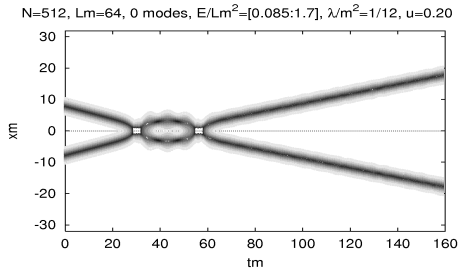

b: $u_i = 0.20$ ($\gamma \approx 1.021$).

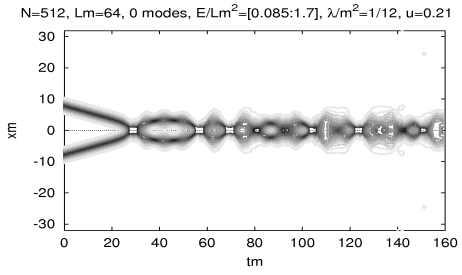

c: $u_i = 0.21$ ($\gamma \approx 1.023$).

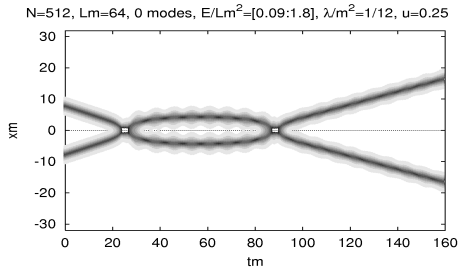

d: $u_i = 0.25$ ($\gamma \approx 1.033$).

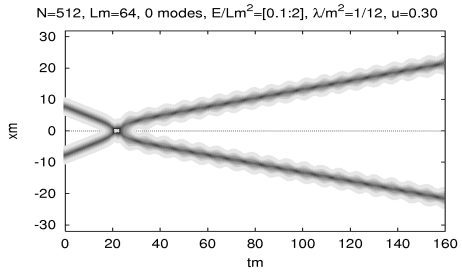

e: $u_i = 0.30$ ($\gamma \approx 1.048$).

Figure 5.5: Colliding classical kink-antikink, $\lambda/m^2 = 1/12$, above and below the critical speed.

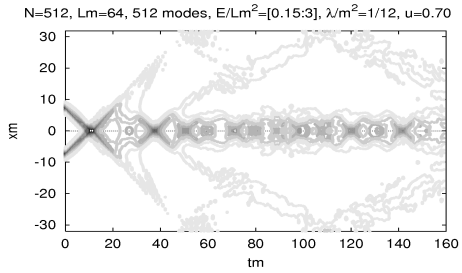

a: $u_i = 0.700$ ($\gamma \approx 1.400$).

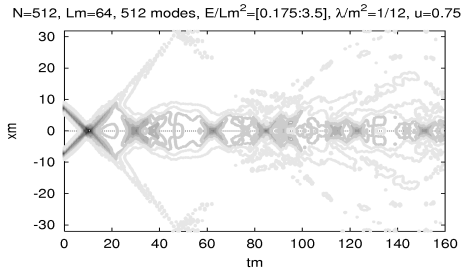

b: $u_i = 0.750$ ($\gamma \approx 1.512$).

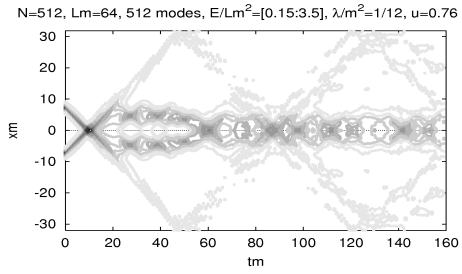

c: $u_i = 0.760$ ($\gamma \approx 1.539$).

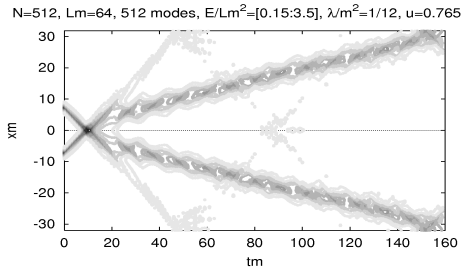

d: $u_i = 0.765$ ($\gamma \approx 1.553$).

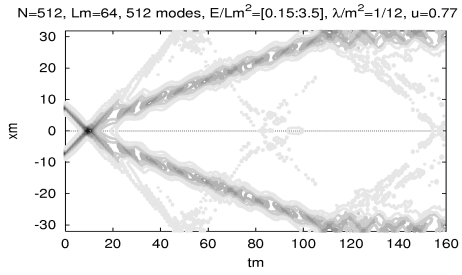

e: $u_i = 0.770$ ($\gamma \approx 1.567$).

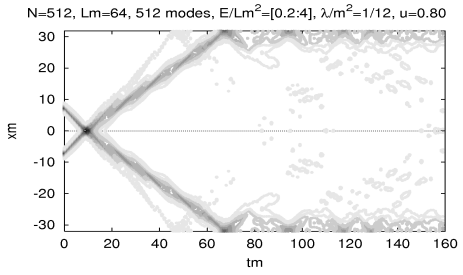

f: $u_i = 0.800$ ($\gamma \approx 1.667$).

Figure 5.6: Colliding Hartree kink-antikink, $\lambda/m^2 = 1/12$, above and below the critical speed.

and the vibrational mode. Except for Fig. 5.5d all shown results are in accordance with Table I in [73]. Since we used different discretizations etc. and given the very narrow width of the stability bands found by [73] we can certainly expect small differences in their precise position, explaining the discrepancy. Finally the authors of [73] found that the final speed, for an initial speed above u_c, satisfies the following relation

$$u_f^2 \propto u_i^2 - u_c^2, \tag{5.13}$$

which is consistent with Fig. 5.5e, from which we derive a final speed $u_f \approx 0.13 - 0.14$.

It is important to note that although breather-like states seem to emerge after a collision, truly stable breathers do not exist in the $\lambda\phi^4$ theory [74]. However, very long-lived and almost stationary configurations do exist [75] as we have shown here again. The radiation causes the energy to decay as $1/\log(t)$, as found analytically by [74] and confirmed numerically by [75].

We would like to compare these classical results with the Hartree approximation and to see if in the quantum theory a critical speed still exists. In the classical theory, one can always use units such that $\mu = \lambda = 1$, and one expects a critical speed to be unique, while in the quantum theory, including the Hartree approximation, this will no longer be possible. However, we will not go further into the question of the coupling dependence of the critical speed.

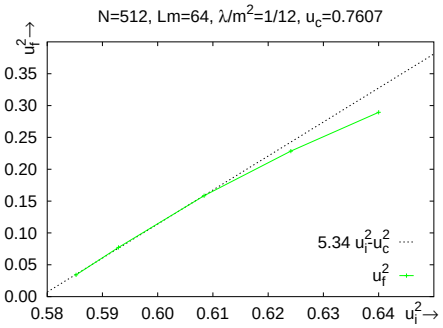

Figure 5.7: u_f^2 as a function of u_i^2 in the Hartree approximation, showing roughly the same behaviour as in classical theory, but with a $u_c = 0.7607$.

In Figure 5.6 the results for six different initial speeds are shown. We see that a critical speed does indeed exist, with a value somewhere between 0.760 and 0.765, indicating that the quantum kink pair is less stable than its classical counterpart, at least at this coupling. One might think that this instability is caused by the fact that we only have an approximate quantum kink-antikink as initial condition, but as can be seen from Fig. 5.6, the pair before the collision looks very stable, there is hardly any wiggling, while after the collision the wave packet is dispersing and oscillating and its speed has decreased considerably. The reason for the higher instability is the radiative channel. This probably also causes the fewer number of breather states found: only at an initial speed $u = 0.760$, very close to the critical speed, can we recognise an approximate

breather state. Bands of stability have not been found and for most simulations in which the pair does not bounce back immediately, the radiation causes them to annihilate.

We also have investigated the functional behaviour of u_f as a function of u_i, to see if it has the same form (5.13), valid in the classical approximation. The result of several runs at different initial speeds is plotted in Figure 5.7. We see that close to the critical speed, u_f indeed behaves in the same way as in the classical theory:

$$u_f^2 = 5.34\left(u_i^2 - u_c^2\right). \tag{5.14}$$

The resulting critical speed u_c can be determined very precisely in this way and we obtain $u_c = 0.760$. Further away from the critical speed the behaviour is not linear in u_i^2, in contrast to the classical result, but the corrections are relatively small.

We have done a few simulations at a stronger coupling $\lambda/m^2 = 1/6$ and they indicate the behaviour is slightly different. For example at a $u_i = 0.80$ we find $u_f = 0.280$, while at $\lambda/m^2 = 1/12$ we found $u_f = 0.538$. The critical speed is not very different. We did not check as fully as for the smaller coupling, but it has a value between 0.790 and 0.795, from a linear fit of u_f^2 versus u_i^2 we obtain $u_c = 0.793$. Since $u_i = 0.80$ is much closer to this value of u_c, the value of u_f at $u_i = 0.80$ is much smaller. The prefactor 5.34 also is higher, around 7 to 7.5, but more data needs to be taken to obtain an accurate answer.

Apart from the factor 3 larger value of the critical speed, their are other important differences between Fig. 5.6 and Fig. 5.5. For example a lot of energy is radiated away after the collision, irrespectively if the pair annihilates or not, in the form of quasi-particles, moving with approximately the speed of light. One might think that the radiation is mainly described by the mode function contribution to the energy density, while the energy density of the surviving kink pair comes from the mean field. However, by checking the different contributions separately we found this is not the case, the kinks are mainly described by the mean field, but also have a contribution from the modes and the radiation is described by both together. Only the total field is a physical quantity describing both the kink-antikink and the radiated particles. Just as only the total two point functions describe the quasi-particles which approximately thermalize.

5.3.4 NUMERICAL RESULTS: SCALING

We are interested in the possibility of using kink-antikink collisions as a description of heavy ion collisions, such as has been conducted at the SPS and are currently being conducted at RHIC and later at LHC. We therefore look closer at the region just after the actual impact, in collisions with high γ. In Figure 5.8 we show the results of four different simulations, at different γ factors and couplings and a comparison with classical dynamics.

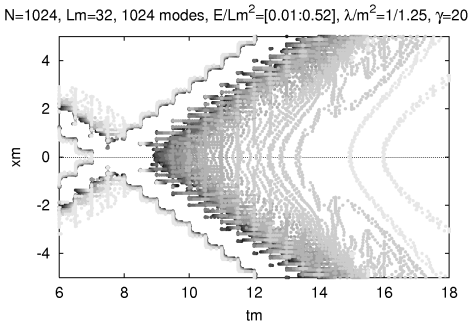

a: Hartree, $\lambda/m^2 = 1/1.25$, $\gamma = 20$ ($u = 0.9987$).

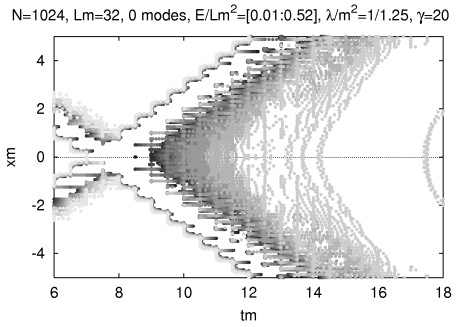

b: Classical, $\lambda/m^2 = 1/1.25$, $\gamma = 20$ ($u = 0.9987$).

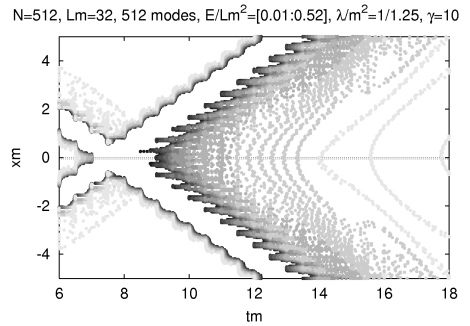

c: Hartree, $\lambda/m^2 = 1/1.25$, $\gamma = 10$ ($u = 0.9950$).

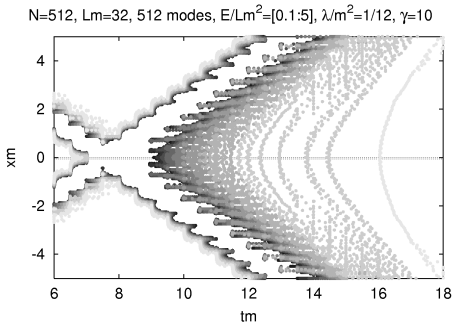

d: Hartree, $\lambda/m^2 = 1/12$, $\gamma = 10$ ($u = 0.9950$).

Figure 5.8: Colliding kink-antikink, period around the collision only.

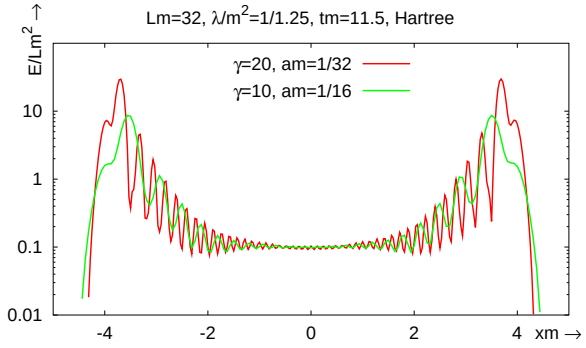

a: $\gamma = 20$ and 10 (Hartree, $\lambda/m^2 = 1/1.25$).

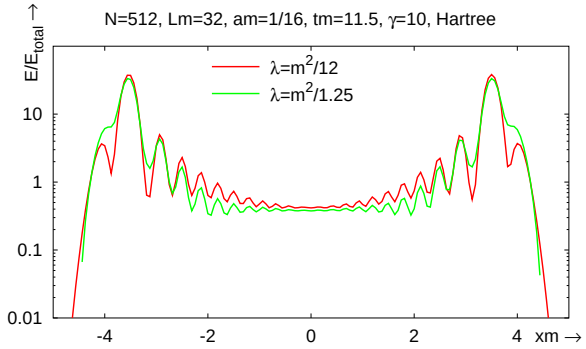

b: $\lambda/m^2 = 1/12$ and $1/1.25$ (Hartree, $\gamma = 10$). The energy density is normalised by the average energy density.

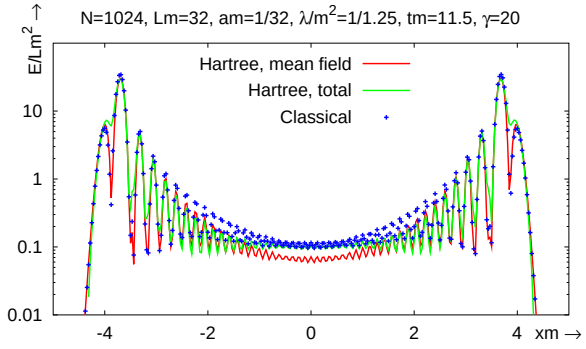

c: Hartree mean field, Hartree total and classical ($\lambda/m^2 = 1/1.25$, $\gamma = 20$).

Figure 5.9: Colliding kink-antikink, time-slice at $tm = 11.5$, after a collision at $tm = 8$.

The plots show a remarkable similarity. In order to investigate this similarity more quantitatively we made a time-slice shortly after the impact, shown in Figure 5.9, at a time 11.5, the impact itself was at time 8. In Figure 5.9a we see that a different impact velocity only influences the resulting energy density in the emerging kink-antikink, the central plateau is the same for both speeds. In Figure 5.9b we see the difference for two couplings. We have re-scaled the energy density with the average density of the whole system in order to compare them. Again, the difference is small. At the stronger coupling the energy is slightly more concentrated in the kink-antikink. Finally in Figure 5.9c we compare the difference between Hartree and classical dynamics. In both simulations the kink-antikink pair region is very similar. The central plateau shows some differences, although the total Hartree energy density in this region is very close to the classical energy density. The modes are essential in this region, the mean field is more concentrated in the kink-antikink. We can conclude from this that there is a scaling behaviour, an extensive range of energies and couplings approximately results in one final plateau. Furthermore at high incident speeds the difference between Hartree and classical is relatively small. Classical dynamics can be used in the study of these collisions, giving further foundation for its use in the study of heavy ion collisions.

It is interesting to compare the results obtained here in kink-antikink collisions with what is known about heavy ion collisions. According to Bjorken [76] the central plateau height is expected to depend only weakly on the incident speed, just as was found here. Furthermore, only a relatively small fraction of the energy should be left in the central region, most of it remains in what is left of the colliding ions, a result which is at least qualitatively consistent with what we find here as well. A first study of hydrodynamic scaling in a ϕ^4 theory can be found in Reference [77]. The authors calculate the energy momentum tensor, which in our metric equals

$$T_{\mu\nu} = \partial_\mu\phi\partial_\nu\phi + \eta_{\mu\nu}\mathcal{L}, \tag{5.15}$$

in two systems, a colliding kink-antikink[5] and a decaying Gaussian wave packet. For a perfect fluid it can be expressed in the energy density and pressure. The assumption of a perfect fluid is valid when collisions can be neglected, as in the (homogeneous) Hartree approximation. For example the trace of $T_{\mu\nu}$ gives (in $1+1$ dimensions)

$$T^\mu_\mu = -e + p = -2V \qquad \begin{cases} e = \frac{1}{2}(\partial_t\phi)^2 + \frac{1}{2}(\partial_x\phi)^2 + V, \\ V = \frac{1}{2}\mu^2\phi^2 + \frac{1}{4}\lambda\phi^4 + \frac{\mu^2}{\lambda}. \end{cases} \tag{5.16}$$

Note that this is a slightly different definition then given by equation (13) in Ref. [77], since we would like both T_{00} and T_{11} to vanish in the vacuum $\phi = v$. From (5.16)

[5]Note that in [77] a product of a kink and antikink is taken, while we use a sum of the two, equation (5.7). Of course both are approximate kink-antikink solutions and the difference should be small.

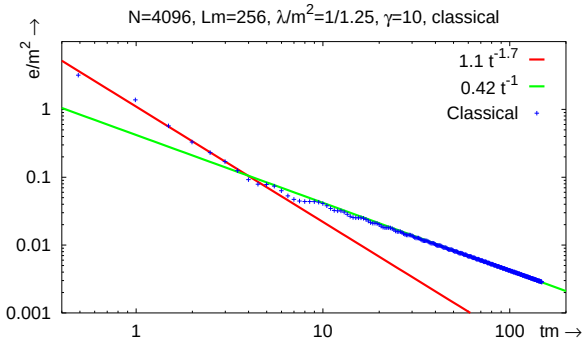

a: Log-log plot of energy density at $x = 0$.

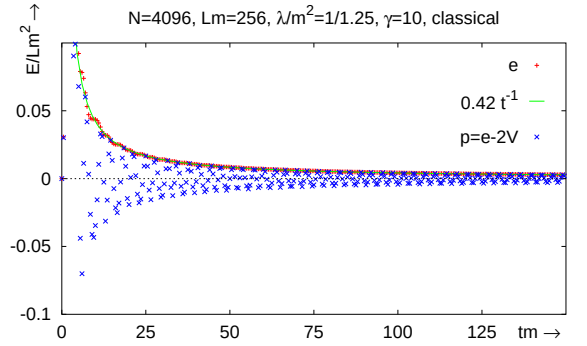

b: Pressure $p = e - 2V$ and energy density. Note that e falls right on top of p.

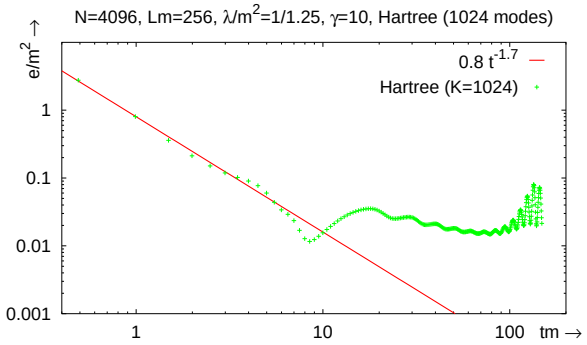

c: Log-log plot of energy density at $x = 0$.

Figure 5.10: Energy density and pressure in the central region, after a classical and a Hartree kink-antikink collision. Both are consistent with $p =$ constant and $c_0 = 0$.

we find the pressure

$$p = \frac{1}{2}(\partial_t \phi)^2 + \frac{1}{2}(\partial_x \phi)^2 - V. \tag{5.17}$$

Using the scaling behaviour one can then for example express the speed of sound in the energy density in the center

$$e \propto \tau^{-(1+c_0^2)} \to t^{-(1+c_0^2)} \qquad \text{at } x = 0, \tag{5.18}$$

where $\tau = \sqrt{t^2 - x^2}$ is the proper time and c_0 is the speed of sound. For a classical kink-antikink collision we plotted the central energy density as a function of time, on a log-log plot in Figure 5.10a and, on a linear scale, together with the corresponding pressure, in Figure 5.10b. Both from equation (5.18) and (5.16) we find that shortly after the collision, the pressure in the central region becomes zero, leading to a vanishing speed of sound, which is quite a remarkable result. Interestingly enough, we see that initially the speed of sound is non-zero, but in the range 0.7 to 0.8. It is not clear to us what causes the change from the relativistic phase, to the pressureless phase.

The result obtained from Hartree dynamics is shown in Figure 5.10c. In this case we can only find a speed of sound in the first stage, the second stage exhibits strange oscillations but no power behaviour. The first stage results in a speed of sound very similar to the classical result.

The result found in the first stage is similar to what was found by Bettencourt et al. but only for times up to $tm \approx 8$. Unlike their study, we are looking for power behaviour in the wake of a kink-antikink collision instead of a disintegrating Gaussian wave packet, since the comparison between a $K\overline{K}$ collision and a heavy ion collision seems more reasonable.

5.4 THERMAL KINK NUCLEATION

In this section we briefly discuss the thermal creation and annihilation properties of the kink-antikink pairs. There is a long history of papers on the subject of thermal nucleation. See for example Reference [78] and reference therein for an analytical study, and for example References [79, 80, 81, 82, 83] for numerical studies.

These numerical studies so far have only considered the classical kink nucleation rate. The Hartree ensemble approximation method allows us to study the creation of kink-antikink pairs starting from a thermal Bose-Einstein distribution and to make a comparison between the classical and Hartree approximation. One of the problems we are thus faced with is a proper definition of kink number. Since only pairs, with no net kink number can be created, we need an effective kink number definition, the winding number will be always 0 or 1 (depending only on the

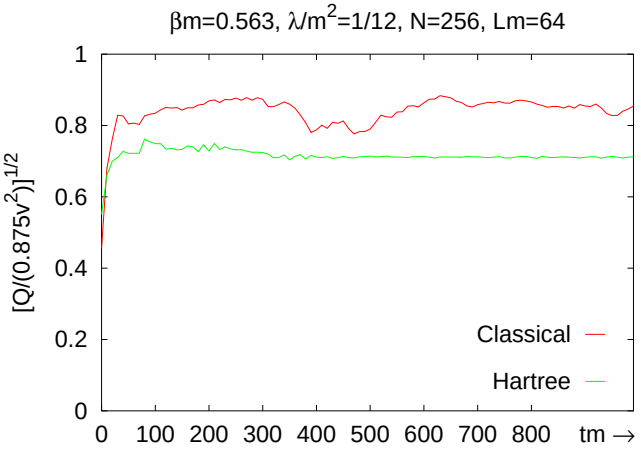

Figure 5.11: Kink indicator parameter Q from equation (5.21) for classical dynamics (upper plot) and Hartree dynamics (lower plot). Both values are normalised with the value 0.875, the value of Q for a symmetrically placed kink-antikink pair in a volume $Lm = 64$. Of course this value heavily depends on the exact position of the kinks.

boundary conditions). Furthermore, in the quantum theory, one might think the kinks will be fully described by the mean field, while the mode functions just describe fluctuations around them. However, as we already noticed before, this split-up cannot be taken so rigorously: the kink number will also be partially described by the modes and we need a definition based on the ensemble description of our system, only ensemble averaged quantities are physical.

In the classical theory, a useful quantity to look at, is the following

$$Q_{\text{class}} = \overline{\phi(x)^2} - \overline{\phi(x)}^2, \tag{5.19}$$

where the overline denotes a spatial average. When a kink-antikink pair is present, this observable will become of the order v^2. If the coupling is not too small, it will therefore give a reasonable indication for their presence. Note that it cannot distinguish between one or multiple pairs. The advantage is that we can easily extend its definition to the quantum theory:

$$Q = \overline{\langle\hat{\phi}(x)\hat{\phi}(x)\rangle} - \overline{\langle\hat{\phi}(x)\rangle}\,\overline{\langle\hat{\phi}(x)\rangle}, \tag{5.20}$$

and that it can be easily found from S_k, eq. (2.52). It is however UV divergent and should be renormalized by subtracting the vacuum contribution:

$$Q_{\text{ren}} = \frac{1}{L}\sum_k \Big(S_k - \frac{1}{2\omega_k^{\text{free}}}\Big). \tag{5.21}$$

We now have a quantum kink indicator, which shows if a pair is present, and that can be compared to the classical theory. We have done so in two simulations at $\lambda/m^2 = 1/12$ in a volume $Lm = 64$, at an inverse temperature $\beta m = 0.563$, just below the thermal phase transition at $\beta m = 0.562$. At such a high temperature we expect the highest creation rate. In a volume $Lm = 64$, it follows from Ref. [81, 82], that we should find about a half to two kinks per total volume, depending on the counting algorithm. The result for Q is shown in Figure 5.11.

We can clearly see it is different from zero, showing the presence of kink-antikink pairs. Furthermore, they emerge through the dynamics, initially the number is lower. Finally, although the quantum number is smaller than the classical, it does *not* go away, while looking at the mean fields in different realisations separately, we find the kink-antikinks do disappear in the Hartree approximation. From Q we see that they first are contained in the mean field, while later they are described by the modes, again showing that only the total two-point functions, from the total field, describe the physical quantum field. As an example of their emergence from the dynamics we plotted in Figure 5.12 the mean field of one of the realisations at 4 different times. Initially the field fluctuates around one of its minima, with a reasonable amount of energy, it then forms a $K\overline{K}$ pair, which subsequently annihilates, while transferring its energy to the quantum modes. The total two point function still describes $K\overline{K}$ pairs, but this cannot be seen from one of the realisations.

5.5 CONCLUSION

In this chapter we looked at the topological defects which can be present in a scalar $\lambda\phi^4$ theory: kinks and antikinks. After a derivation of the classical solutions, we used both classical and Hartree dynamics in studying their annihilation, both when at rest and when boosted. We found that classical kink pairs are much more stable than their Hartree counterparts. Hartree kink pairs at smaller coupling are therefore also more stable than at larger couplings. Although we do not know an exact Hartree solution to the equations of motion, by damping the mean field equation, we can find an approximate solution. This damping can, especially at larger couplings, prolong the survival time enormously, but is still orders of magnitude shorter than for a classical kink-antikink pair, due to radiation in the form of quantum particles, the quasi-particles discussed in Chapters 2 and 3. We suggested a

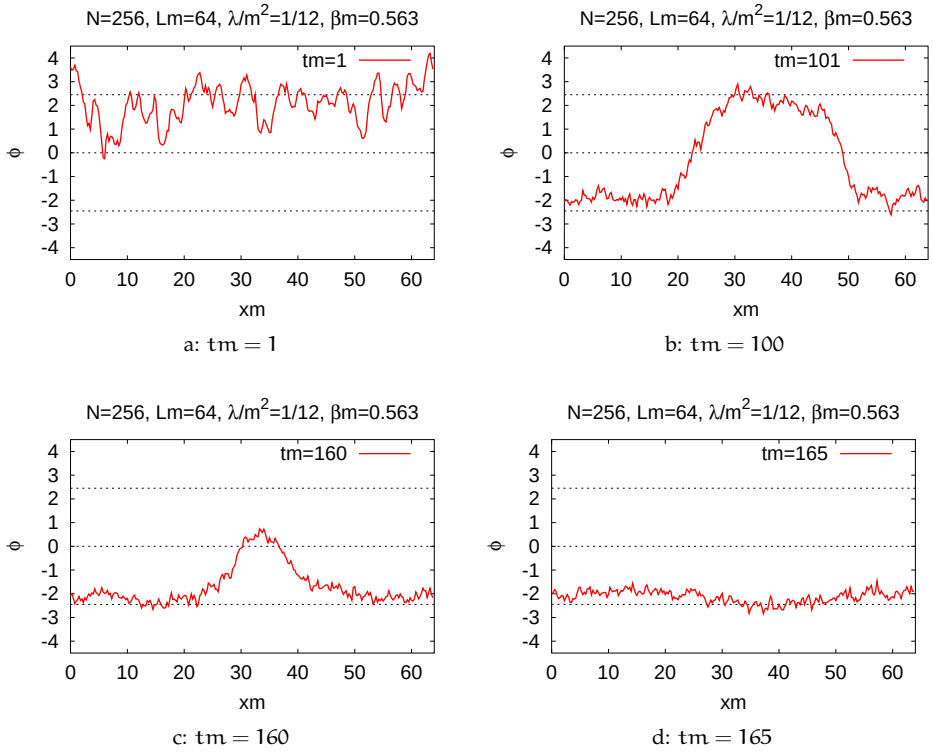

Figure 5.12: Thermal kink nucleation and subsequent annihilation in the Hartree approximation. The dotted lines are at $\pm v(T = 0)$ and 0.

algorithm to find an accurate numerical and more stable solution for the Hartree equations of motion, but we have not yet tested it.

Using a damped mean field equation of motion we were also able to find an approximate quantum kink mass. The Hartree approximation seems to give better results than the one-loop semi-classical approximation, especially at larger couplings, where the semi-classical approximation fails. Damping the equations has some unwanted side-effects, such as the slow damping with a very long time scale, which sets in after a time $tm \approx 10-20$ and which has a strong volume dependence. It would be interesting to investigate this phenomenon further. In order to check the validity of the Hartree approximation in the determination of the soliton mass, it would of course be best to do a lattice Monte Carlo simulation, as in [69, 70], at our parameters. This is also a topic for future research.

The kink-antikink pair, after annihilation, also leads to an approximate thermal Bose-Einstein spectrum, just as a flat initial ensemble. The initial energy distribution has a form which approaches the thermal distribution more easily than the flat ensemble, as used in Chapter 2. This makes it possible to recognise the Bose-Einstein already in an early stage, although the statistical errors are larger, since we cannot average over multiple initial conditions.

In the study of kink collisions, we found once more that the classical kinks are much more stable: for the classical dynamics, we reproduced the results of [73] on the critical speed and the existence of approximate breather modes. In the Hartree approximation the critical speed is considerably higher and we were not able to find stability bands, i.e. approximate breather solutions. In order to make this result rigorous, many more simulations have to be done, at higher precision, since the radiation makes it difficult to see clearly if a short-lived bound state, or breather, has emerged. It is also important to check the dependence on the coupling. In the classical theory the dimensionless critical speed is independent of λ as the action can be rewritten in a way that $\mu = \lambda = 1$, while in the quantum theory, this is not possible.

We compared some of the results from these kink-antikink collisions with the heavy ion collisions such as are carried out at the RHIC in Brookhaven and in the future at the LHC at CERN in Genève. Although the scalar ϕ^4 theory is much to simple to serve even as a toy model for this, it is interesting to see that we can compare some of the ingredients: the kinks describing the colliding hadrons or ions and the quasi-particles describing the "plasma". After the collision, the resulting field showed a central plateau, with scaling behaviour: the plateau height only weakly depends on the initial speed of the kinks, and scales with the coupling in a very straightforward way. Most of the energy remained in the receding kink-antikink. The qualitative difference between the Hartree and classical approximations is small. However, at the quantitative level there are important differences.

For example, shortly after the collision, both the Hartree and classical dynamics resulted in a speed of sound of about 0.7 to 0.8, while after a time $tm \approx 8$, this speed in the classical simulation dropped to zero, i.e. vanishing pressure, while in the Hartree dynamics the energy density became roughly constant, making it impossible to obtain a speed of sound.

In Ref. [77] the Hartree plasma was also found to behave as a relativistic plasma, with speed of sound close to 1, similar to what we found until a time $tm \approx 8$. However the result in [77] was obtained from a disintegrating Gaussian wave packet, instead of a colliding kink-antikink. It would be interesting to find a more accurate result for the speed of sound in the Hartree approximation.

Finally we have briefly looked at the connection between a thermal Bose-Einstein distribution and the creation and annihilation of kinks in the system. We found that we need to consider the complete field in the description of kinks, not only the mean field. This means that we have to look at quantum and ensemble averages only, the separate realisations give some impression of what is happening but do not describe the full theory. It is hopeful to see that although the kinks disappear from the mean field, our rough kink indicator does not go to zero, but becomes constant, i.e. the creation and annihilation rate are equal. However, we do find fewer pairs in the Hartree approximation than in the classical theory, probably related to the higher instability of Hartree kinks. In the Hartree description, more energy is carried by radiation than in the classical theory.

BIBLIOGRAPHY

[1] E. W. Kolb and M. S. Turner, *The Early Universe* (Addison-Wesley Pulishing Company, Reading, USA, 1990).

[2] B. J. W. Tent, Ph.D. thesis, University Utrecht, Utrecht (2002).

[3] K. A. Olive (2002) astro-ph/0202486.

[4] A. D. Dolgov, Nucl. Phys. Proc. Suppl. **110** (2002) 137-143, hep-ph/0201107.

[5] A. D. Sakharov, Pisma Zh. Eksp. Teor. Fiz. **5** (1967) 32-35, [JETP Lett. **5** (1967) 24-27].

[6] J. M. Cline, Pramana **54** (2000) 1-10, hep-ph/0003029.

[7] J. M. Cline (2002) hep-ph/0201286.

[8] U. W. Heinz, AIP Conf. Proc. **602** (2001) 281-292, hep-ph/0109006.

[9] D. Bödeker, G. D. Moore, and K. Rummukainen, Phys. Rev. **D61** (2000) 056003, hep-ph/9907545.

[10] W.-H. Tang and J. Smit, Nucl. Phys. **B540** (1999) 437-456, hep-lat/9805001.

[11] S. Y. Khlebnikov and I. I. Tkachev, Phys. Rev. Lett. **77** (1996) 219-222, hep-ph/9603378.

[12] T. Prokopec and T. G. Roos, Phys. Rev. **D55** (1997) 3768-3775, hep-ph/9610400.

[13] G. N. Felder and L. Kofman, Phys. Rev. **D63** (2001) 103503, hep-ph/0011160.

[14] J. García-Bellido, D. Y. Grigoriev, A. Kusenko, and M. E. Shaposhnikov, Phys. Rev. **D60** (1999) 123504, hep-ph/9902449.

[15] A. Rajantie, P. M. Saffin, and E. J. Copeland, Phys. Rev. **D63** (2001) 123512, hep-ph/0012097.

[16] G. Parisi, Europhys. Lett. **40** (1997) 357-362.

[17] G. Aarts, G. F. Bonini, and C. Wetterich, Nucl. Phys. **B587** (2000) 403-418, hep-ph/0003262.

[18] G. Aarts, G. F. Bonini, and C. Wetterich, Phys. Rev. **D63** (2001) 025012, hep-ph/0007357.

[19] G. Aarts and J. Smit, Phys. Rev. **D61** (2000) 025002, hep-ph/9906538.

[20] G. Aarts and J. Smit, Nucl. Phys. **B555** (1999) 355-394, hep-ph/9812413.

[21] G. Aarts and J. Smit, Nucl. Phys. **B511** (1998) 451-478, hep-ph/9707342.

[22] G. Aarts and J. Smit, Phys. Lett. **B393** (1997) 395-402, hep-ph/9610415.

[23] P. Arnold, Phys. Rev. **D55** (1997) 7781-7796, hep-ph/9701393.

[24] B.-J. Nauta, Nucl. Phys. **B575** (2000) 383-396, hep-ph/9906389.

[25] G. Aarts, B.-J. Nauta, and C. G. van Weert, Phys. Rev. **D61** (2000) 105002, hep-ph/9911463.

[26] D. Boyanovsky and H. J. de Vega, in *Current topics in astrofundamental physics: The cosmic microwave Background*, edited by N. G. Sánchez (Kluwer, 2000), proceedings Erice Chalonge School, astro-ph/0006446.

[27] F. Cooper, Y. Kluger, E. Mottola, and J. P. Paz, Phys. Rev. **D51** (1995) 2377-2397, hep-ph/9404357.

[28] M. A. Lampert, J. F. Dawson, and F. Cooper, Phys. Rev. **D54** (1996) 2213-2221, hep-th/9603068.

[29] B. Mihaila, J. F. Dawson, and F. Cooper, Phys. Rev. **D56** (1997) 5400-5412, hep-ph/9705354.

[30] B. Mihaila, T. Athan, F. Cooper, J. Dawson, and S. Habib, Phys. Rev. **D62** (2000) 125015, hep-ph/0003105.

[31] A. V. Ryzhov and L. G. Yaffe, Phys. Rev. **D62** (2000) 125003, hep-ph/0006333.

[32] B. Mihaila, F. Cooper, and J. F. Dawson, Phys. Rev. **D63** (2001) 096003, hep-ph/0006254.

[33] K. Blagoev, F. Cooper, J. Dawson, and B. Mihaila, Phys. Rev. **D64** (2001) 125003, hep-ph/0106195.

[34] G. Aarts, D. Ahrensmeier, R. Baier, J. Berges, and J. Serreau, Phys. Rev. **D66** (2002) 045008, hep-ph/0201308.

[35] J. Berges and J. Cox, Phys. Lett. **B517** (2001) 369-374, hep-ph/0006160.

[36] F. Cooper, J. F. Dawson, and B. Mihaila (2002) hep-ph/0209051.

[37] J. García-Bellido, M. G. Peréz, and A. González-Arroyo (2002) hep-ph/0208228.

[38] D. Boyanovsky, H. J. de Vega, R. Holman, and J. F. J. Salgado, Phys. Rev. **D54** (1996) 7570-7598, hep-ph/9608205.

[39] L. Mandel and E. Wolf, *Optical coherence and quantum optics* (Cambridge University Press, Cambridge, UK, 1995).

[40] J. R. Klauder and B.-S. Skagerstam, *Coherent States: applications in physics and mathematical physics* (World Scientific, Singapore, 1985).

[41] M. Sallé, J. Smit, and J. C. Vink, Phys. Rev. **D64** (2001) 025016, hep-ph/0012346.

[42] M. Sallé and J. Smit (2002) hep-ph/0208139.

[43] M. Sallé, J. Smit, and J. C. Vink, Nucl. Phys. **B625** (2002) 495-511, hep-ph/0012362.

[44] M. Sallé, J. Smit, and J. C. Vink, in *Strong and electroweak matter 2000 – Proceedings of the SEWM2000 Meeting*, edited by C. P. Korthals Altes (World Scientific, Singapore, 2000), hep-ph/0008122.

[45] M. Sallé, J. Smit, and J. C. Vink, Nucl. Phys. Proc. Suppl. **94** (2001) 427-430, hep-lat/0010054.

[46] B. S. DeWitt, *Dynamical theory of groups and fields* (Gordon and Breach, London, 1965), originally published in: Relativity, groups and topology, proceedings of the Les Houches Summer School of Theoretical Physics 1963, (Blackie, London, 1964).

[47] H.-S. Roh and T. Matsui, Eur. Phys. J. **A1** (1998) 205-220, nucl-th/9611050.

[48] F. Cooper, S. Habib, Y. Kluger, and E. Mottola, Phys. Rev. **D55** (1997) 6471-6503, hep-ph/9610345.

[49] J. Smit, *Introduction to Quantum Fields on a Lattice* (Cambridge University Press, UK, 2002).

[50] H. A. Weldon, Phys. Rev. **D28** (1983) 2007.

[51] E. Wang and U. W. Heinz, Phys. Rev. **D53** (1996) 899-910, hep-ph/9509333.

[52] L. M. A. Bettencourt, K. Pao, and J. G. Sanderson, Phys. Rev. **D65** (2002) 025015, hep-ph/0104210.

[53] R. G. Miller, Biometrika **61** (1974) 1-15.

[54] G. Aarts and J. Berges, Phys. Rev. **D64** (2001) 105010, hep-ph/0103049.

[55] D. Boyanovsky, C. Destri, H. J. de Vega, R. Holman, and J. F. J. Salgado, Phys. Rev. **D57** (1998) 7388-7415, hep-ph/9711384.

[56] R. Micha and I. I. Tkachev (2002) hep-ph/0210202.

[57] J. C. Vink, private communication.

[58] R. Rajaraman, *Solitons and Instantons* (North-Holland Publishing Company, Amsterdam, 1982).

[59] E. B. Bogomol'nyi, Sov. J. Nucl. Phys. **24** (1976) 449.

[60] M. Gleiser and A. Sornborger, Phys. Rev. **E62** (2000) 1368-1374, patt-sol/9909002.

[61] J. M. Speight and R. Ward, Nonlinearity **7** (1994) 475.

[62] J. M. Speight, Nonlinearity **10** (1997) 1615, patt-sol/9703005.

[63] J. M. Speight, Nonlinearity **12** (1999) 1373-1387, hep-th/9812064.

[64] A. B. Adib and C. A. S. Almeida, Phys. Rev. **E64** (2001) 37701-37704, hep-th/0104225.

[65] R. F. Dashen, B. Hasslacher, and A. Neveu, Phys. Rev. **D10** (1974) 4130-4138.

[66] A. Alonso Izquierdo, W. García Fuertes, M. A. González León, and J. Mateos Guilarte, Nucl. Phys. **B635** (2002) 525-557, hep-th/0201084.

[67] H. J. de Vega, Nucl. Phys. **B115** (1976) 411-428.

[68] J. Verwaest, Nucl. Phys. **B123** (1977) 100-108.

[69] J. C. Ciria and A. Tarancón, Phys. Rev. **D49** (1994) 1020-1028, hep-lat/9309019.

[70] A. Ardekani and A. G. Williams, Austral. J. Phys. **52** (1999) 929-937, hep-lat/9811002.

[71] L. P. Kadanoff, Phys. Rev. Lett. **23** (1969) 1430-1433.

[72] L. P. Kadanoff and H. Ceva, Phys. Rev. **B3** (1971) 3918-3939.

[73] D. K. Campbell, J. F. Schonfeld, and C. A. Wingate, Physica **9D** (1983) 1.

[74] H. Segur and M. D. Kruskal, Phys. Rev. Lett. **58** (1987) 747-750.

[75] J. Geicke, Phys. Rev. **E49** (1994) 3539-3542, brief Reports.

[76] J. Bjorken, Phys. Rev. **D27** (1983) 140-151.

[77] L. M. A. Bettencourt, F. Cooper, and K. Pao (2001) hep-ph/0109108.

[78] J. F. Currie, J. A. Krumhansl, A. R. Bishop, and S. E. Trullinger, Phys. Rev. **B22** (1980) 477-496.

[79] D. Y. Grigoriev and V. A. Rubakov, Nucl. Phys. **B299** (1988) 67-78.

[80] M. G. Alford, H. Feldman, and M. Gleiser, Phys. Rev. Lett. **68** (1992) 1645-1648.

[81] F. J. Alexander and S. Habib, Phys. Rev. Lett. **71** (1993) 955-958, hep-th/9212059.

[82] F. J. Alexander, S. Habib, and A. Kovner, Phys. Rev. **E48** (1993) 4284-4296, hep-th/9308103.

[83] S. Habib and G. Lythe, Phys. Rev. Lett. **84** (2000) 1070-1073, cond-mat/9911228.

SAMENVATTING

In deze samenvatting zal ik proberen, op een voor een algemeen publiek leesbare wijze, uit te leggen waar dit proefschrift over gaat. Het is hiervoor verhelderend om eerst op de context in te gaan.

Een interessante ontwikkeling in de hedendaagse fundamentele natuurkunde is het samenkomen van de fysica van de hele grote afstanden, de kosmologie en de hele kleine afstanden, de subatomaire fysica. Deze gebieden lijken op het eerste gezicht weinig met elkaar te maken te hebben, maar zoals zal blijken is voor het begrijpen van de één de ander nodig. Het onderzoek beschreven in dit proefschrift heeft zodoende ook toepassingen in beide velden.

Een zeer belangrijke ontdekking, die aan de basis staat van de moderne kosmologie is de observatie door Edwin Hubble in 1929 dat, naarmate sterrenstelsels verder van ons weg staan, ze steeds harder van ons af bewegen. Deze observatie heeft uiteindelijk geleid tot het "hete oerknal model". Dit beschrijft, simpel gezegd, het vroege heelal als een reusachtige explosie, die in feite nu, circa 15 miljard jaar later, nog steeds doorgaat. Uitdijende gaswolken koelen af, en vergelijkbaar koelt ook het uitdijende het heelal af. Als we dus teruggaan in de tijd wordt het steeds heter en neemt de dichtheid steeds verder toe. In deze richting gaande worden ook de typische deeltjes steeds kleiner: vaste stoffen vallen uit elkaar in losse moleculen en atomen in de vorm van gassen, bij nog hogere temperaturen vallen de atomen uit elkaar en vormen een plasma van losse kernen en elektronen. Bij nog weer hogere temperaturen vallen ook de kernen uit elkaar in losse protonen en neutronen. Ook deze protonen en neutronen vallen uiteindelijk uit elkaar en vormen dan een plasma van quarks en gluonen (gluonen zijn de dragers van de sterke kernkracht, zoals fotonen, oftewel licht, de dragers zijn van de elektromagnetische kracht). Naar dit quark gluon plasma wordt op dit moment hard gezocht, o.a. bij de RHIC in Brookhaven en straks bij de LHC van het CERN bij Genève. Er zijn inmiddels al aanwijzingen voor het bestaan gevonden op grond van eerdere experimenten met de SPS eveneens van het CERN. Later in deze samenvatting zal ik nog kort terug komen op het quark gluon plasma.

De hierboven genoemde overgangen worden faseovergangen genoemd en deze gebeurtenissen zijn belangrijk omdat ze vaak leiden tot waarneembare signalen. Zo dateert bijvoorbeeld de Kosmische Microgolf Achtergrondstraling van de overgang van een plasma van kernen en elektronen naar neutrale atomen, circa 300 000 jaar na de oerknal, en is het hete oerknal model in staat de relatieve dichtheden

van de lichte elementen zoals waterstof en helium, gevormd circa 3 minuten na de oerknal, correct te voorspellen met als enige vrije parameter de netto hoeveelheid baryonen (protonen plus neutronen). Met netto wordt hier bedoeld baryonen minus antibaryonen: van alle (elementaire) deeltjes bestaat ook een antiversie, met exact dezelfde massa, maar o.a. tegengestelde lading.

Dit netto aantal baryonen blijkt zeer klein te zijn. Een belangrijk onderzoeksgebied is het voorspellen en begrijpen van dit kleine maar belangrijke getal, dat wederom met een faseovergang te maken moet hebben: bij lage temperaturen is de levensduur van het proton vele malen de leeftijd van het heelal, maar bij hoge temperaturen wordt het instabiel. Dit gebeurd rond de "elektrozwakke faseovergang", die plaats vond toen de temperatuur van het heelal circa 10^{15} Kelvin was. Bij die overgang kregen alle deeltjes hun massa, via het zogeheten Higgs mechanisme en moet ook het netto baryongetal zijn ontstaan, baryogenese: boven de overgang wordt het netto baryongetal nul door interacties, hier onder kan het niet veranderen.

De fysica die belangrijk is in het vroege heelal is dus die van elementaire deeltjes en fundamentele krachten bij zeer hoge temperaturen en rond faseovergangen. De deeltjes en krachten (behalve de zwaartekracht) worden beschreven met het zogeheten Standaard Model, dat in staat is gebleken tot zeer grote precisie de experimenten in de deeltjesversnellers, zoals bij het CERN, te beschrijven. Faseovergangen goed beschrijven is echter een lastig probleem. Het Standaard Model is beschreven met behulp van quantum veldentheorie. Een veel gebruikte techniek bij berekeningen hierin is storingsrekening. Deze werkt echter niet goed voor het beschrijven van faseovergangen, zoals ik hieronder zal uitleggen. Verder is het voor bijvoorbeeld het beschrijven van baryogenese, maar ook de vorming van het quark gluon plasma, nodig om het systeem te volgen in de tijd, het is niet in evenwicht, wat een verdere reductie van het aantal beschikbare technieken betekent.

Voor het beschrijven van een klassiek mechanisch systeem is het in principe voldoende om de potentiaal en de begintoestand te specificeren (klassiek geeft de potentiaal de hoeveelheid potentiele energie die het deeltje heeft en maakt het mogelijk op een zeer elegantie manier de bewegingsvergelijkingen af te leiden). Klassiek, dat wil zeggen niet quantummechanisch, zal een niet bewegend deeltje zich in een minimum van de potentiaal bevinden. Quantummechanisch kan echter een deeltje niet stilstaan op een precieze plaats, men kan niet plaats en snelheid onbeperkt nauwkeurig bepalen en de deeltjes zullen fluctueren om een minimum van de potentiaal. Het is daarom een stuk lastiger om toch verwachtingswaardes van fysische grootheden uit te rekenen. Men maakt hierbij vaak gebruik van storingsrekening: voor een beperkt aantal potentialen kan ook in de quantummechanica exact worden uitgerekend hoe de verwachtingswaarde van grootheden afhangt van de potentiaal. Door de fysische potentiaal te schrijven als zo'n exact oplosbare poten-

tiaal plus een verschil- of storingsterm kan een benadering worden gemaakt van de verwachtingswaarde in de fysische potentiaal.

In veldentheorie is de zaak wat ingewikkelder, ook daar wordt het systeem gespecificeerd door potentiaal en beginvoorwaarden, maar een veld heeft op iedere plaats in de ruimte een waarde. Dit leidt er toe dat in quantum velden theorie eigenlijk alleen de meest simpele situatie nog oplosbaar is, die van een vrije theorie, beschreven door een harmonische potentiaal (het veldentheoretische analogon van een deeltje aan een veer). Het verschil tussen de exacte potentiaal en de harmonische potentiaal is in het algemeen niet geschikt voor storingsrekening. Door alleen in de buurt van een minimum van de potentiaal te kijken kan dit probleem verholpen worden. Hiervoor is het dus wel nodig dat de fluctuaties rond dat minimum niet te groot zijn en is het essentieel dat de configuraties rond één minimum fluctueren. Dit is in het algemeen niet het geval bij faseovergangen, wat het gebruik van storingsrekening drastisch beperkt.

In klassieke veldentheorie is het stukken eenvoudiger om de evolutie van systemen te berekenen. Heel simpel gezegd is het effect van quantum mechanica op klassieke mechanica het toevoegen van quantum fluctuaties rond de klassieke oplossing. Zodoende kunnen we in quantum veldentheorie ook een expansie rond de klassieke oplossing maken. De niet in storingsrekening te vangen effecten worden beschreven door de klassieke oplossing, terwijl de kleine quantum fluctuaties eromheen beschreven worden in storingsrekening. De in dit proefschrift gebruikte Hartree benadering is ook zo'n soort benadering, en is daarmee beter in staat om processen te beschrijven die niet noodzakelijkerwijs in de buurt van een minimum van de potentiaal plaats vinden. Een andere benadering is het geheel negeren van de quantum fluctuaties. Vooral bij hoge temperaturen, zoals in het vroege heelal, is dit een verdedigbare benadering. Hoewel het op het eerste gezicht slechter lijkt dan de Hartree benadering, is dat niet per se het geval.

Het andere probleem van het beschrijven van faseovergangen is hun niet-evenwichts karakter. Als een systeem in evenwicht is, en in het bijzonder bij hoge temperatuur, kunnen allerlei extra benaderingsmethodes gebruikt worden, zoals bijvoorbeeld Monte Carlo simulaties. Als echter ook de dynamica beschreven moet kunnen worden, is dit niet langer mogelijk. De klassieke en de Hartree benadering zijn dan enkele van de weinige resterende mogelijkheden.

Zoals alle benaderingen heeft ook de Hartree benadering zijn beperkingen. Eén van deze beperkingen is het beschrijven van de gang naar evenwicht. De benadering is goed voor een kort tijdje, maar daarna niet meer. Eén van de oorzaken hiervoor is dat het te veel van de interacties weggooit. In dit opzicht is de klassieke benadering beter dan de Hartree benadering, en is daarom op haar beurt wel in staat om de gang naar evenwicht te beschrijven, zij het dan klassiek evenwicht. Men kan nu hopen dat een geschikte "combinatie benadering" in staat zou zijn om

de gang naar een quantum evenwicht te beschrijven.

In Hoofdstuk 1 wordt zo'n combinatie benadering geïntroduceerd, de Hartree ensemble benadering. We bestuderen deze benadering in een eenvoudig model, waarbij de ruimte beperkt is tot een lijn. In Hoofdstuk 2 wordt vervolgens gekeken of en hoe deze benadering de gang naar evenwicht kan beschrijven. In Hoofdstuk 3 wordt gekeken of dit evenwicht ook vastgehouden kan worden als het eenmaal bereikt is, en wordt een vergelijking gemaakt met de puur klassieke benadering.

In deze eerste paar hoofdstukken blijkt dat het beschrijven van equilibratie veel beter gaat in de zogeheten gebroken fase, dan in de symmetrische fase. Dit begrip heeft te maken met de vorm van de potentiaal. De potentiaal die we beschouwen is een zeer veel gebruikte en wordt, naar zijn wiskundige vorm, de ϕ^4 potentiaal genoemd. Deze potentiaal kan één of twee minima hebben, afhankelijk van een parameter en de temperatuur. Bij hoge temperaturen, boven een zekere faseovergang, is er altijd slechts één minimum. In Hoofdstuk 4 kijken we naar de potentiaal die voor alle temperaturen slechts één minimum heeft, de symmetrische situatie. Voor equilibratie is het nodig dat er genoeg interactie is, maar het blijkt dat er in de symmetrische situatie te weinig zijn om de gang naar evenwicht goed te kunnen beschrijven in de Hartree benadering.

In Hoofdstuk 5 wordt tenslotte gekeken naar een toepassing van de benaderingsmethode in de andere fase van het systeem, die met twee minima. Zoals hierboven zeer kort uitgelegd, wordt in storingsrekening gekeken naar de fluctuaties rond een van de minima. In het geval er twee minima zijn, zal er eentje gekozen worden. De aanvankelijke symmetrie tussen beide breekt spontaan. Dit kan gezien worden als het plaatsen van een bal precies op de top van een berg, met aan twee kanten een dal. De meest minimale verstoring zal het in een van beide laten terechtkomen, maar welke is niet bij voorbaat vast te stellen, de symmetrie zal spontaan breken. In veldentheorie is er niet sprake van één deeltje dat op één plaats is, maar sprake van een veld dat op alle plaatsen een bepaalde waarde heeft (zoals de temperatuur in een kamer). In veldentheorie is spontane symmetriebreking daarmee ingewikkelder, het veld hoeft niet overal in de ruimte in het zelfde minimum van de potentiaal terecht te komen. Zo'n veldconfiguratie, waarin het veld op één plaats in het ene minimum zit en verderop in het andere, wordt een kink genoemd.

In een zeker opzicht kunnen deze kinks gezien worden als de deeltjes die in deeltjesversnellers op elkaar worden geschoten. Net als die deeltjes hebben ook kinks hun antiversie en kunnen ze annihileren. In het laatste hoofdstuk wordt gekeken naar dit soort botsingsprocessen en wordt gekeken in hoeverre de Hartree ensemble benadering toegepast op de ϕ^4 theorie kan fungeren als een zeer versimpeld model voor de zware-ion botsingen bij RHIC en LHC.

DANKWOORD

Deze laatste bedrukte pagina wil ik graag gebruiken voor het bedanken van een slechts een klein deel van de mensen die mij de afgelopen jaren hebben geholpen.

Allereerst natuurlijk mijn promotor, Jan Smit, die altijd een open deur had en altijd bereid was vragen te beantwoorden. Het is soms moeilijk om heel direct als promovendus met je promotor samen te werken, maar ik geloof dat je er uiteindelijk veel meer van leert.

Ook Jeroen Vink, helaas slechts gedurende kort tijd aan ons Instituut verbonden, wilde ik bedanken voor zijn grondigheid en vaak kritische opstelling. De discussies die we met z'n drieën hadden waren daardoor vaak lang en schijnbaar zonder voortgang, maar leidden uiteindelijk tot veel beter onderbouwde resultaten.

Bert-Jan wilde ik bedanken voor zijn altijd gewillige oor en geduld in de eerste helft van mijn promotie. Ik ben benieuwd of je terug naar de natuurkunde gaat.

Mijn eerste kamergenoot, na twee jaar, werd Ad Maas. Niet alleen kamergenoot maar ook goede vriend. We woonden allebei in de Rivierenbuurt, trouwden een week na elkaar, werden allebei vader en zijn nu allebei postdoc, een paar maanden na elkaar. Ik hoop dat we onze discussies per e-mail zullen voortzetten.

Mark wilde ik graag bedanken voor de gezelligheid op en buiten het Instituut. Eerst hadden we het alleen maar over de computer, later gelukkig minder. Mijn eerst zo trouwe bezoeken aan je concerten werden helaas ook minder en zullen nu wel helemaal niet meer lukken. Je hulp tijdens onze verhuizing naar Helsinki was reusachtig en onmisbaar!

Om alle andere collegae, die het Instituut tot een tweede huis maakten, persoonlijk te noemen gaat te ver, bij deze een gezamenlijk dank je wel.

Buiten het Instituut om waren er soms weinig, maar wel heel belangrijke mensen. Allemaal zagen ze mij vaak veel te weinig. Ik hoop dat ik in dit opzicht mijn leven kan beteren. Een paar wil ik hier expliciet noemen.

Anna: we lijken soms uit elkaar te groeien, maar ik geloof niet dat dat zo is. Tien jaar is een lange tijd, en ik hoop dat het er veel meer worden.

Ook mijn ouders en zus hebben mij veel te weinig gezien. Dat zal moeilijk beter worden nu wij in Helsinki wonen. Dank jullie wel voor de hulp bij de afronding van dit proefschrift en in het bijzonder Marijke: dank je wel voor de mooie kaft!

De laatste regels van dit proefschrift zijn al heel lang gereserveerd voor degene die er het meest onder te lijden heeft gehad, maar er misschien wel het belangrijkste voor was. Dank je wel Naomi, voor in mij te geloven, zelfs als ik dat niet deed.